

**Coupled transport and population growth of
Pseudomonas putida cells
in the vicinity of a toluene source plume
in a saturated sand-packed 2-D microcosm**

A Dissertation

Presented to

The Faculty of the School of Engineering and Applied Science

University of Virginia

Dr. Roseanne Ford, Advisor

Dr. Giorgio Carta

Dr. Lisa Colosi Peterson

Dr. Geoffrey Geise

Dr. Kyle Lampe

In Partial Fulfillment

Of the Requirements for the Degree

Doctor of Philosophy (Chemical Engineering)

By

Shun Zheng

August 2017

Abstract

Nearly half of all Americans drinking water comes from groundwater, while it suffers a great potential threat from the leakage of hazardous substances from underground storage tanks. According to US EPA, there are more than 400,000 confirmed underground storage tank leaks nationwide. Bioremediation is the treatment that uses naturally occurring microorganisms to break down these hazardous substances into less toxic or nontoxic substances. In the past years, increasing amount of data have been reported regarding the enhancement of the contaminant biodegradation rate by the chemotaxis of the microorganisms to these pollutants due to their increased delivery to the contaminated site, the process of which is often hindered by the non-uniform distributions of subterranean hydraulic conductivity. Although mixing transverse to the flow path is suggested to be a primary limiting factor for biodegradation efficiency, other steps can also contribute to the hindrance of the bioremediation process, for instance, the first step for the bacteria to degrade the contaminants is their uptake into the cell body. In this study, we investigated the impact of the toluene uptake step on the bioremediation efficiency using *Pseudomonas putida* F1 wild type and knockout mutant strains (PpF1 wild type, PpF1 (Δ todX), and PpF1 (Δ todX Δ cymD Δ F1fadL)) whose toluene transmembrane transport channel(s) were removed, yet their chemotaxis to toluene was preserved. To this end, a bench-scale 2-D microcosm system was used as the study platform mimicking features of the naturally occurring groundwater system to study bioremediation efficiency limiting factors under conditions closer to those in natural aquifers. The application of mathematical models that incorporate the cell growth rate during this process - which is dependent on the toluene uptake that provides the cells with the carbon and energy source for survival and proliferation – will further elucidate to what extent the uptake step contributes to the bioremediation process in comparison with other steps such as dispersion and chemotaxis. The results revealed that PpF1 (Δ todX)

that has reduced toluene transport capability, exhibited a lower percent recovery as compared with the wild type, implying less toluene consumption, and furthermore, exposure of the bacterial population to an increased toluene concentration (up to a certain level) increased the cell percent recovery. Furthermore, PpF1 (*ΔtodXΔcymDΔF1fadL*) that had even lower toluene uptake capability due to additional removal of toluene transport related channels, showed even lower recovery from the 2-D microcosm under the same experimental conditions. A mathematical model was then set up to study in detail the transport processes of the species during the microcosm experiments, and it was confirmed the sensitiveness of the toluene degradation efficiency to bacterial growth-related parameters which was directly correlated with toluene uptake capability, regardless of the presence of mass transfer barrier. And this sensitiveness was reserved under different conditions, for example, in a region more distant to toluene source and at an increased flow rate which can occur at different geographic locations. This suggests that, in addition to mechanisms that enhance the delivery of the degrading agents to the contaminated site, transport membrane proteins of bacteria can also play a key role in bioremediation enhancement. Moreover, it suggests the potential of engineering bacteria toward higher contaminant permeability for enhanced bioremediation efficiencies.

Acknowledgement

To my advisor Dr. Roseanne Ford: for your guidance, patience, encouragement, support, and care throughout my PhD study. I can't express more than enough of how much I feel fortunate and grateful of having this experience to study under your supervision. Your mentorship goes beyond the academic training and extends to how to lead a life and become a better person. Your wisdom will keep inspiring me for the rest of my life.

To my Dad Zhongyang Zheng: this dissertation is fully dedicated to you, the enlightener of my curiosity as well as interest in truth, and the pursuit thereafter. You've been accompanying me all the way here, and I know you will always be there with me along the way ahead. To my family: my Mom Zhengyu Piao, brother Yongwen Zheng, sister-in-law Yuedan An, and nephew Haoyan Zheng: your endless love and support brought me here. This accomplishment can never be achieved without you. We did this together, and I love you.

To my dissertation committee Dr. Giorgio Carta, Dr. Lisa Colosi Peterson, Dr. Geoffrey Geise, Dr. Kyle Lampe: thank you very much for serving as my committee, and for your insightful input and thoughtful discussions about this work.

To our collaborators Dr. Bert van den Bert and Dr. Anne Doble from the Newcastle University: for the provision of the cell strains and the share of your pearls of wisdom during the course of this research.

To research groups at UVA: thank Dr. Robert G. Kelly for the access to COMSOL, Dr. James N. Demas for the access to the fluorimeter, and Dr. Lisa Peterson for the access to GC/MS.

To current and past Ford group members Joanna Adadevoh, Xueying Zhao, Gabrielle Chen, Justin Peruzzi, Julia Sheehan, and Mathew Smith: it was fun studying and brainstorming together with you, and thank you for putting me up when things were not going quite smoothly.

To all my dear friends at UVA: for sharing everything, which can either be joys, challenges or even sorrow, for so many unforgettable memories that we created together, and for growing up together with me.

To the funding sources: my gratitude also goes to the financial support by National Institutes of Health under the award number “1R01GM104495-01” for the experimental part of this study, and National Science Foundation under the award number “NSF1141400” for the support of the simulation part.

Table of contents

List of Figures	vii
List of Tables	xii
List of Symbols	xiv
Chapter 1. Introduction	1
Chapter 2. 2-D Microcosm Experiments	7
2.1. Introduction	7
2.2. Materials and methods	9
2.3. Comparison of cell growth	13
2.3.1. Comparison of cell growth on agar plate	13
2.3.2. Comparison of cell growth in liquid media	14
2.4. 2-D Microcosm experiments: without toluene	16
2.5. 2-D Microcosm experiments: low & high concentration of toluene	20
2.6. 2-D Microcosm experiments: three PpF1 strains	24
2.7. 2-D Microcosm experiments: toluene analysis	26
2.8. Reproducibility	28
Chapter 3. Computational Simulation	30
3.1. Introduction	30
3.2. Mathematical model	32
3.3. COMSOL simulation: A representative result	38
3.4. Comparison: cell growth/death vs. chemotaxis	44
3.5. Parametric study	49
3.5.1. Sensitivity analysis of simulation results with current experimental setup	50
3.5.2. Moment analysis of simulation results with current experimental setup	56

3.6.	Effect of oxygen	60
3.7.	Effect of spacing between bacterial cell and toluene	64
3.8.	Effect of flow rate	68
	Chapter 4. Conclusions and Recommendations.....	72
	References	74
	Appendices	81
A1.	Uranine quantification.....	81
A2.	Cell enumeration.....	83
A2.1.	Cell staining	83
A2.2.	Fluorimeter analysis.....	84
A2.3.	Flow cytometer analysis	85
A3.	Toluene quantification by GC-MS	93
A4.	Moment analysis	95
A5.	Gaussian fitting	96
A6.	Medium and buffer recipes	97
A7.	2-D microcosm experiments: scheme, image, analyte concentration profile	98
A8.	COMSOL parameter calculations	102
A9.	COMSOL setting window capture.....	107
A10.	Calculation of sensitivity of bacterial cell recovery to bacterial cell growth and chemotaxis parameters.....	111

List of Figures

Figure 1.1	The <i>tod</i> operon controls toluene degradation in <i>Pseudomonas putida</i> F1. Toluene (A) is catalyzed by a series of enzymes in the <i>tod</i> operon to 2-hydroxy-6-oxo-2, 4-heptadienoate (B) and then 2-hydroxypenta-2, 4-dienoate (C) before entering the TCA cycle to produce CO ₂ and H ₂ O. <i>todX</i> is believed to be the gene for the transport channel on the bacteria membrane to uptake toluene. Operon <i>cymD</i> is also confirmed to support the growth of <i>Pseudomonas putida</i> F1 on toluene by van den Berg lab although the exact metabolic pathway has not been fully elucidated yet.	4
Figure 2.2.1	A 2-D microcosm was used in this study to mimic the natural groundwater system.	10
Figure 2.3.1	Comparison of growth of three PpF1 strains on LR agar plate where toluene was supplied in the gas phase. 1: PpF1 wild type; 2: PpF1 single knockout strain; 3: PpF1 triple knockout strain. The growth rate is in the order: PpF1 wild type > PpF1 single knockout strain > PpF1 triple knockout strain.	15
Figure 2.3.2.1	Comparison of growth of three PpF1 strains in liquid media. The growth rate is in the orde: PpF1 wild type > PpF1 single knockout strain > PpF1 triple knockout strain. The growth rates of three PpF1 strains are statistically significant (<i>p</i> -value <0.05).	2
Figure 2.4.1	Schemes and pictures of 2-D microcosm runs without toluene.	17
Figure 2.4.2	Concentration profiles of two bacterial strains, PpF1 wild type (PpF1 f0) and PpF1 single knockout strain (PpF1 f1) at the 2-D microcosm outlet. Uranine served as a tracer and internal control.	17
Figure 2.5.1	Configurations for four different microcosm runs with PpF1 wild type (PpF1 f0) and PpF1 single knockout strain (PpF1 f1).	21
Figure 2.5.2	Concentration profiles of bacterial cells and uranine for microcosm Run #3. PpF1 wild type (PpF1 f0) was injected above the toluene plume and PpF1 single knockout strain (PpF1 f1) below the toluene plume.	21
Figure 2.5.3	Plot of cell recovery for PpF1 wild type and PpF1 single knockout strain (PpF1 f1) when injected above and below the toluene plume, both at low and high concentration of toluene.	22
Figure 2.6.1	Configurations for two different microcosm runs with PpF1 wild type (PpF1 f0) and PpF1 triple knockout strain (PpF1 f3).	25

Figure 2.6.2	Plot of cell recovery for three PpF1 strains: PpF1 wild type (PpF1 f0), PpF1 single knockout strain (PpF1 f1) and PpF1 triple knockout strain (PpF1 f3), when 1e-4 v/v of toluene was fed. Recovery was plotted both when PpF1 strains were injected above and below the toluene plume. ... 25
Figure 2.7.1	Toluene profiles at the microcosm outlet from an abiotic experiment and Run #6. 27
Figure 2.8.1	Averaged uranine recovery. 29
Figure 2.8.2	Averaged PpF1 cell recovery over 2 runs. PpF1 f0 was injected 1e-4 v/v toluene plume and PpF1 f3 below toluene plume. 29
Figure 3.3.1	COMSOL simulation results with bacterial cell growth/death and chemotaxis terms applied: distribution of toluene within the microcosm as a function of time. (A) 0 h; (B) 5 h; (C) 10 h; (D) 15 h; (E) 18 h; (F) 19 h; (G) 20 h after injection; (H) steady state; (I) scale bar for (A)-(H); (J) toluene concentration profile at inlet; (K) toluene concentration profile at outlet of the microcosm as a function of time. 41
Figure 3.3.2	COMSOL simulation results with bacterial cell growth/death and chemotaxis terms applied: distribution of bacterial cells within the microcosm as a function of time. (A) 0 h; (B) 5 h; (C) 10 h; (D) 15 h; (E) 18 h; (F) 19 h; (G) 20 h after injection; (H) steady state; (I) scale bar for (A)-(H); (J) bacterial cell concentration profile at inlet; (K) bacterial cell concentration profile at outlet of the microcosm as a function of time. . 42
Figure 3.3.3	COMSOL simulation results with bacterial cell growth/death and chemotaxis terms applied: distribution of oxygen within the microcosm as a function of time. (A) 0 h; (B) 5 h; (C) 10 h; (D) 15 h; (E) 18 h; (F) 19 h; (G) 20 h after injection; (H) steady state; (I) scale bar for (A)-(H); (J) oxygen concentration profile at inlet. (K) oxygen concentration profile at outlet of the microcosm as a function of time. 43
Figure 3.4.1	Simulation results: effect of bacterial cell growth/death and chemotaxis on the distribution of toluene, bacterial cells, and oxygen distribution. Images were captured 19 h after injection. (A) Toluene distribution within 2-D microcosm: (A1) with growth/death and chemotaxis, (A2) with chemotaxis only, (A3) with growth/death only, (A4) without growth/death and chemotaxis; (B) Bacterial cell distribution within 2-D microcosm: (B1) with growth/death and chemotaxis, (B2) with chemotaxis only, (B3) with growth/death only, (B4) without growth/death and chemotaxis; (C) Oxygen distribution within 2-D microcosm: (C1) with growth/death and chemotaxis, (C2) with chemotaxis only, (C3) with growth/death only,

	(C4) without growth/death and chemotaxis.	47
Figure 3.4.2	Simulation results: effect of bacterial cell growth/death and chemotaxis on the distribution of toluene, bacterial cells, and oxygen distribution at the outlet of 2-D microcosm. Each concentration profile was captured at 19 h after injection. (A) Toluene; (B) Bacterial cell; (C) Oxygen. (thick grey line: with growth/death and chemotaxis; black dash line: with chemotaxis only; black dot line: with cell growth only; think grey line: without growth/death and chemotaxis).	48
Figure 3.5.1.1	Tornado chart for sensitivity analysis of bacterial cell recovery and toluene recovery to growth and chemotaxis parameters, with 19-h sample.	51
Figure 3.5.1.2	Tornado chart for sensitivity analysis of bacterial cell recovery and toluene recovery to growth and chemotaxis parameters at steady state. (note: recovery values at 120% of μ_{max} instead of those at 200% were plotted)	53
Figure 3.5.1.3	Fitted curves for sensitivity calculation (reference point: $x=1$). The table below listed the calculated sensitivity for growth and chemotaxis parameters.	55
Figure 3.5.2.1	Concentration profiles of bacterial cells at the outlet at various parameter values.	59
Figure 3.6.1	With O ₂ incorporated in the model. Distribution of toluene (A), bacterial cell (B), and oxygen (C) within the 2-D microcosm at steady state. (D) is the scale bar for (A) and (C), and (E) is the scale bar for (B). Concentration profile of toluene, bacterial cell, and oxygen at the outlet were plotted over y-axis in (F).	61
Figure 3.6.2	Without O ₂ incorporated in the model. Distribution of toluene (A), bacterial cell (B), and oxygen (C) within the 2-D microcosm at steady state. (D) is the scale bar for (A) and (C), and (E) is the scale bar for (B). Concentration profile of toluene, bacterial cell, and oxygen at the outlet were plotted over y-axis in (F).	61
Figure 3.6.3	Comparison of toluene and bacterial cell recovery when oxygen was and wasn't incorporated in the mathematical model.	62
Figure 3.6.4	Effect of oxygen concentration on toluene and bacterial cell recovery... ..	63
Figure 3.7.1	With 3 cm spacing between bacterial cell and toluene (experimental setup). Distribution of toluene (A), bacterial cell (B), and oxygen (C) within the 2-D microcosm at steady state. (D) is the scale bar for (A) and (C), and (E) is the scale bar for (B). Concentration profile of toluene,	

	bacterial cell, and oxygen at the outlet were plotted over y-axis in (F). .	65
Figure 3.7.2	With 4 cm spacing between bacterial cell and toluene. Distribution of toluene (A), bacterial cell (B), and oxygen (C) within the 2-D microcosm at steady state. (D) is the scale bar for (A) and (C), and (E) is the scale bar for (B). Concentration profile of toluene, bacterial cell, and oxygen at the outlet were plotted over y-axis in (F).	65
Figure 3.7.3	Tornado chart for sensitivity analysis of bacterial cell recovery (A) and toluene recovery (B) to growth and chemotaxis parameters at steady state, with increased spacing between bacterial cells and toluene.	66
Figure 3.7.4	Fitted curves for sensitivity calculation at the reference point ($x=1$) with simulation with increased spacing between bacterial cells and toluene. The table below listed the calculated sensitivity for growth and chemotaxis parameters with increased spacing between bacterial cells and toluene, as well as those from current experimental setup for comparison.	67
Figure 3.8.1	Simulation result at $V_f = 1.55 \text{ e-}5 \text{ m/s}$ (experimental setup). Distribution of toluene (A), bacterial cell (B), and oxygen (C) within the 2-D microcosm at steady state. (D) is the scale bar for (A) and (C), and (E) is the scale bar for (B). Concentration profile of toluene, bacterial cell, and oxygen at the outlet were plotted over y-axis in (F).	69
Figure 3.8.2	Simulation result at $V_f = 1.76 \text{ e-}4 \text{ m/s}$. Distribution of toluene (A), bacterial cell (B), and oxygen (C) within the 2-D microcosm at steady state. (D) is the scale bar for (A) and (C), and (E) is the scale bar for (B). Concentration profile of toluene, bacterial cell, and oxygen at the outlet were plotted over y-axis in (F).	69
Figure 3.8.3	Tornado chart for sensitivity analysis of bacterial cell recovery and toluene to growth and chemotaxis parameters at steady state, with higher flow rate.	70
Figure 3.8.4	Fitted curves for sensitivity calculation at the reference point ($x=1$) with simulation with higher flow rate. The table below listed the calculated sensitivity for growth and chemotaxis parameters with higher flow rate, as well as those from current experimental setup for comparison.....	71
Figure A1.1	Adsorption spectrum of uranine. Uranine has an absorption peak at $\sim 490 \text{ nm}$	81
Figure A1.2	Calibration curve of uranine, measured with absorption at 490 nm	82
Figure A2.2.1	Excitation and emission spectrum of cells stained with FM4-64. Ex/Em	

	for stained cells is ~ 500 nm/650 nm.	84
Figure A2.3.1	Optimization of FSC-H threshold for cell counting. M9, unstained cells and stained cells were counted with various FSC-H thresholds. In the vertical direction from top to bottom, FSC-H thresholds are 10 k, 20 k and 30 k in turn.	89
Figure A2.3.2	Optimization of FL3-H threshold. Stained cells, unstained cells and M9 samples were counted with FSC-H threshold of 10k, and cell counts were plotted over FL3-H value.	89
Figure A2.3.3	Cell counting of serially diluted stained cell samples. Cell counts of 1x, 0.1x and 0.01x stained cell samples were plotted over FL3-H value.	90
Figure A2.3.4	Calibration curve of cell counting with flow cytometer. Double thresholds - FSC-H of 10 k and FL3-H of 1 k - were used.	92
Figure A3.1	Toluene calibration curve by GC-MS analysis.	94
Figure A7.1	2-D Microcosm experiments with PpF1 f0, PpF1 f1 and PpF1 f3: scheme, images and concentration profiles of uranine and PpF1 cells at the outlet (continued on next page).	99
Figure A7.2	2-D Microcosm experiments with PpF1 f0, PpF1 f1 and PpF1 f3: scheme, images and concentration profiles of uranine and PpF1 cells at the outlet (continued from last page).	100
Figure A.9.1	COMSOL parameter setting.	107
Figure A9.2	COMSOL Mesh setting.	107
Figure A9.3	COMSOL setting for toluene (1).	108
Figure A9.4	COMSOL setting for toluene (2).	108
Figure A9.5	COMSOL setting for bacterial cell (1).	109
Figure A9.6	COMSOL setting for bacterial cell (2).	109
Figure A9.7	COMSOL setting for oxygen (1).	110
Figure A9.8	COMSOL setting for oxygen (2).	110

List of Tables

Table 2.1.1	Three types of PpF1 strains and genotype.	8
Table 2.3.2.1	Cell density of three PpF1 strains measured after 16-hour culture in LR media with toluene supplied at gas phase.	15
Table 2.3.2.2	Statistical analysis of growth rates of three PpF1 strains.	15
Table 2.4.1	Comparison of parameter values (mean μ and variance σ^2) from Gaussian fitting of uranine tracer concentration and bacterial cell counts in 2-D microcosm effluent samples for PpF1 wild type and PpF1 single knockout strain.	18
Table 2.5.1	List of cell recovery data in four microcosm runs. The same shading/patterning represents the same microcosm run, respectively. At the outlet of each microcosm run, cells were collected, counted, and calibrated to uranine recovery, then compared with the inlet concentration for the percent recovery calculation.	22
Table 2.6.1	List of cell recovery data for three PpF1 strains during 2-D microcosm experiments with 1e-4 v/v toluene fed: PpF1 wild type (PpF1 f0), PpF1 single knockout strain (PpF1 f1) and PpF1 triple knockout strain (PpF1 f3). At the outlet of each microcosm run, cells were collected, counted, and calibrated to uranine recovery, then compared with the inlet concentration for the percent recovery calculation.	25
Table 2.8.1	Averaged uranine recovery data.	29
Table 2.8.2	Averaged PpF1 cell recovery data.	29
Table 3.2.1	Parameter values used in COMSOL simulation.	37
Table 3.5.1.1	Parametric study with bacterial cell recovery and toluene recovery, with 19-h sample.	51
Table 3.5.1.2	Parametric study with bacterial cell recovery and toluene recovery, at steady state.	53
Table 3.5.2.1	Moment analysis. \bar{y} was listed in reference to the injection position.	59
Table 3.7.1	Parametric study with bacterial cell recovery and toluene recovery, with increased spacing between bacterial cells and toluene.	66
Table 3.8.1	Dispersion coefficient of toluene, bacterial cell, and oxygen at low and high flow rate.	70
Table 3.8.2	Parametric study with bacterial cell recovery and toluene recovery, with	

	higher flow rate.	70
Table A1.1	Calibration curve of uranine measured with adsorption at 490 nm.	82
Table A2.3.1	Optimization of FSC-H threshold for cell counting. No cells (M9 media only), unstained cells and stained cells were counted with various FSC-H thresholds.	87
Table A2.3.2	Event counting of M9 with various parameters. Double thresholds - FSC-H of 10 k and FL3-H of 1 k - gave negligible recordings.	90
Table A3.1	GC-MS noise peak information. (n=3).	94
Table A3.2	Toluene calibration curve from GC-MS (n=3), noise peak area has been deducted from original value.	94
Table A7.2	List of peak parameters from Gaussian fitting and moment analysis for uranine and PpF1 strains in 2-D microcosm run #1 ~ #5 (#5' is repeat run of #5). <i>Italic numbers</i> are from Gaussian fitting and others from moment analysis.	101

List of Symbols

Symbols

a	toluene concentration (chemoattractant)
b	bacterial cell concentration
o	oxygen concentration (electron acceptor)
t	time
x	the distance longitudinally in the flow direction
y	the transverse distance to the x axis
a_0	injected toluene concentration
b_0	injected bacterial concentration
o_0	injected oxygen concentration
$D_{a,bulk}$	bulk diffusion coefficient for toluene
$D_{a,eff}$	effective diffusion coefficient for toluene in porous media
$D_{a,eff,ref}$	effective diffusion coefficient for toluene from reference
D_{ax}	longitudinal dispersion coefficient for toluene
$D_{ax,ref}$	longitudinal dispersion coefficient for toluene from reference
D_{ay}	transverse dispersion coefficient for toluene
$D_{ay,ref}$	transverse dispersion coefficient for toluene from reference
$D_{b,bulk}$	bulk diffusion coefficient for bacterial cell
$D_{b,eff}$	effective diffusion coefficient for bacterial cell in porous media
D_{bx}	longitudinal dispersion coefficient for bacterial cell
D_{by}	transverse dispersion coefficient for bacterial cell
$D_{o,bulk}$	bulk diffusion coefficient for oxygen
$D_{o,eff}$	effective diffusion coefficient for oxygen in porous media
D_{ox}	longitudinal dispersion coefficient for oxygen
D_{oy}	transverse dispersion coefficient for oxygen
K_a	half saturation constant, growth on toluene
K_c	chemotaxis receptor binding constant
K_o	half saturation constant, growth on oxygen
k_{decay}	bacterial cell decay rate
MW_b	molecular weight of bacterial cell

MW_o	molecular weight of oxygen
MW_t	molecular weight of toluene
q_a	maximum reaction rate of toluene
q_o	maximum reaction rate of oxygen
R	retardation factor
v_b	bacterial cell swimming speed
U_{avg}	apparent flow rate
V_b	single bacterial volume
V_f	average interstitial velocity
$V_{f,hi}$	average interstitial velocity, high flow rate
$V_{f,ref}$	average interstitial velocity from reference
v_{set}	bacterial cell settling velocity due to gravity
$Y_{b/a}$	yield coefficient of the bacterial cell on toluene
$Y_{b/o}$	yield coefficient of the bacterial cell on oxygen

Greek letters

α_{ax}	longitudinal dispersivity for toluene
α_{ay}	transverse dispersivity for toluene
α_{bx}	longitudinal dispersivity for bacterial cell
α_{by}	transverse dispersivity for bacterial cell
α_{ox}	longitudinal dispersivity for oxygen
α_{oy}	transverse dispersivity for oxygen
ξ	porosity
ε_{ref}	Porosity from reference
σ_b^2	variance of bacterial concentration peak at microcosm outlet
τ	tortuosity
μ_{max}	maximum specific growth rate of cell on toluene
$\mu_{max,o}$	maximum specific growth rate of cell on oxygen
$\chi_{0,eff}$	chemotactic sensitivity coefficient

Chapter 1. Introduction

With the rapid development of new technologies and industrialization of modern society, the production of pollutant substances places a large burden on the environment and is posing substantial risks for groundwater quality, due to the fact that many of these compounds are toxic, carcinogenic and teratogenic. When released as non-aqueous phase liquids (NAPL), large amounts of contaminants can be trapped in soils and remain there until they slowly dissolve into groundwater, a process that can continue for decades or even centuries (1-8). According to a study by European Soil Data Centre of the European Commission, the number of estimated potential contaminated sites is more than 2.5 million and the identified contaminated sites around 342 thousand, with mineral oil and heavy metals being the main contaminants contributing around 60% to soil contamination (2). In the US, approximately 558,000 underground storage tanks nationwide store petroleum or hazardous substances, and there are more than 400,000 confirmed underground storage tank leaks nationwide (3-4).

Aromatic hydrocarbons are widespread pollutants within the environment owing to natural releases, improper industrial and social activities, such as the widespread occurrences of leakage from underground petroleum storage tanks and spills at petroleum production wells and refineries, and their removal has proven to be very challenging. As a result, aromatic hydrocarbons are listed as priority pollutants by the US Environmental Protection Agency (9). In addition, due to the limited chemical reactivity and hydrophobic character, aromatic hydrocarbons and many other xenobiotics are highly persistent within the environment. Besides the obvious health-related factors, there is also a considerable economic burden resulting from the presence of pollutants within the environment due to the high costs of the treatment and cleanup of contaminated sites by

various abiotic methods, such as incineration of soils, soil washing, pump and treat, *etc.* (10-18).

Moving together with the groundwater flow, the dissolution of aromatic hydrocarbon contaminants into the groundwater forms a contaminant plume. The lengths of contaminant plumes vary between several to a few hundred meters and the total expanse is specifically governed by natural attenuation. Most abiotic attenuation process, for example, dilution, sorption, ion exchange, volatilization, precipitation, chemical transformation and dispersion (19-22), only play a role during the early stages of contamination until microbial degradation becomes established. Subsequently, microbial activity is the only process that effectively leads to a net loss of pollutants in plumes contaminated with petroleum hydrocarbons (23-32). Thus, there has been a great amount of interest concerning metabolism of pollutants by bacteria as well as the application of those bacteria for the removal of xenobiotics from the environment (23-34). *In situ* bioremediation has been demonstrated to be an efficient and cost-effective method to reduce organic contamination under certain conditions (14, 33-37). Compared with the traditional pump-and-treat approach, it mainly utilizes bacteria, by either stimulating indigenous species (biostimulation) or introducing exogenous species (bioaugmentation), to metabolically degrade the contaminants without disturbing the natural environment or requiring large space for equipment.

Bioremediation is a complex process involving a series of steps including the delivery of the biodegraders to the contaminants, the contaminant uptake and the metabolism of the contaminants by the biodegraders. Experimental studies by Griebl and coworkers (38-40) showed that biodegradation occurred at the edges of contaminant plumes and was mixing-controlled; however, under different conditions other steps may be the limiting

factors, for example, the passage of hydrophobic substrates into the cell body, in regard to the effective barrier of the cells against alien molecules. In this study, we propose to investigate the impact of this uptake step on bioremediation, comparing strains that differ in their permeability to the contaminants under conditions that are relevant for the natural environment. The application of a mathematical model that accounts for transport, proliferation and degradation will quantify the extent to which the bioremediation is dependent on the uptake step as compared with the delivery of cells to the contaminated site. To this end, a model system comprising of the degraders *Pseudomonas putida F1* strains and the contaminant toluene was used where a saturated sand packed 2-D microcosm served as the study platform.

Pseudomonas putida F1 (PpF1) has a number of advantages, which make it an ideal model microorganism for this study. PpF1 is known to be chemotactic to a number of aromatic hydrocarbons and chlorinated aliphatic compounds, a property that is likely to aid its efficiency as a biodegrader (41). While many bacterial isolates have been identified with aromatic hydrocarbon-degrading capabilities, only few of them have been characterized in detail. PpF1 was isolated from a polluted creek in Urbana (IL), and was the first biodegrader whose genome was sequenced (42). It has a large genome of 6.0 Mb and is a versatile organism found in soil and water that is capable of growth on the mono-aromatic hydrocarbons (MAH) benzene, toluene, ethylbenzene and p-cymene (43).

To test the toluene uptake step on bioremediation efficiency, PpF1 mutant strains were generated by knocking out the uptake channels, which led to impaired uptake capability comparing with the wild type. PpF1 is a gram-negative bacterium where the thin peptidoglycan layer of their cell wall is sandwiched between an inner cytoplasmic cell membrane and a bacterial outer membrane. The outer membrane of PpF1 is a very

effective barrier against the permeation of hydrophobics such as toluene, due to the lipopolysaccharide in the outer leaflet of the outer membrane. Thus, the outer membrane is a unique lipid bilayer that requires specific channels for the uptake of hydrophobics such as aromatic hydrocarbons destined for biodegradation and these specific channels are usually trans-membrane proteins encoded by the bacterial genome. Besides the availability of the genomic sequence, another advantage of PpF1 is that all its biodegradative capabilities are encoded on the chromosome and not on a large catabolic plasmid, as is the case for many biodegrader strains. This removes the need to ensure that the plasmid is maintained and avoids potential incompatibilities with expression plasmids used for gene complementation.

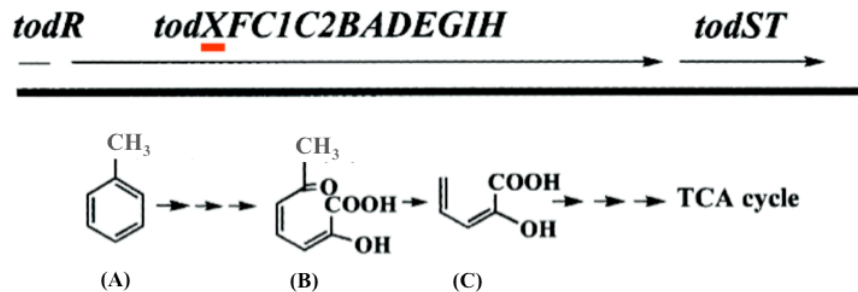


Figure 1.1 The *tod* operon controls toluene degradation in *Pseudomonas putida* F1. Toluene (A) is catalyzed by a series of enzymes in the *tod* operon to 2-hydroxy-6-oxo-2, 4-heptadienoate (B) and then 2-hydroxypenta-2, 4-dienoate (C) before entering the TCA cycle to produce CO₂ and H₂O. *todX* is believed to be the gene for the transport channel on the bacteria membrane to uptake toluene. Operon *cymD* is also confirmed to support the growth of *Pseudomonas putida* F1 on toluene by van den Berg lab although the exact metabolic pathway has not been fully elucidated yet.

PpF1 has two operons responsible for the degradation of MAH, located adjacent to each other. These operons are designated *tod* (toluene degradation) and *cym/cmt* (p-cymene/p-cumate). The *tod* operon (**Figure 2.1**) consists of the genes *todXFC1C2BADEGIH*, which together encode for seven enzymatic reactions. All enzymes within the *tod* operons are soluble and located within the cytoplasmic space. The operon contains one member of the

FadL family of outer membrane channels, TodX. While the involvement of TodX in substrate uptake in PpF1 has not been demonstrated, there is inconclusive experimental evidence linking the FadL orthologs TbuX to toluene uptake in *Ralstonia pickettii* and XylN to toluene uptake in *Pseudomonas putida* F1 (44). A *tod* knockout strain and a *tod/cymD/FadL* triple knockout strain were generated by the van den Berg lab (Newcastle University, UK), which demonstrated decreased toluene permeability as compared with wild type. Furthermore, TodX is known to not affect the PpF1 chemotactic pathway (39).

The objective of this study is to investigate the impact of contaminant uptake by microorganisms on bioremediation with a bench-scale 2-D microcosm under conditions that are relevant for the natural environment, where mass transfer limitations have posed a significant barrier for bioremediation efficiency. Bioremediation being a complex process comprises a series of steps, i.e., the delivery of the biodegraders to the contaminants, the uptake of the contaminant, and the chemical transformation of the contaminants by the biodegraders. While previous studies emphasized mass transfer as the limiting factor for the overall rate of contaminant removal, the subsequent uptake step can also contribute to the remediation efficiency. This study will not only be of fundamental importance in clarifying the mechanisms underlying the bioremediation processes, but also in providing insights that lead to the design of bacterial strains with altered and/or enhanced biodegradation properties.

In this study, it is hypothesized that in a 2-D microcosm mimicking features of the natural groundwater system, the toluene uptake can serve as the “remediation-rate-limiting” step. Thus, it is expected that the PpF1 cell strain with the greater toluene uptake rate proliferates faster upon the consumption of toluene as sole carbon source inside the microcosm in comparison to the strain with the lower toluene uptake rate. To test this

hypothesis, a 2-D microcosm mimicking the natural groundwater system will be used as the study platform wherein both mass transfer and toluene uptake can play a role in the proliferation rate. First, PpF1 wild type and PpF1 (*ΔtodX*) strains will be respectively introduced above and below the toluene plume during the same microcosm run. As they travel through the microcosm from one end to the other, transverse dispersion as well as chemotaxis serve as transport mechanisms that bring them closer to the toluene plume upon which they survive and proliferate. PpF1 (*ΔtodX*) strain whose toluene uptake channel has been knocked out are expected to proliferate to a lesser extent than the wild type. Next, a triple knockout mutant strain PpF1 (*ΔtodX, ΔcymD, ΔFadL*) with even lower toluene uptake capability, whose proliferation rate is expected to be even slower, will be tested in the same way. Furthermore, a mathematical model quantifying transport, uptake and degradation will be set up and matched to the experimental system to evaluate in detail how and how much the chemotactic and cell growth/death parameters affect the overall bioremediation process. Under natural environment, typical groundwater flow rate in a sandy or gravelly aquifer may range from 0.5 to 50 feet per day (45, 46), and the location where the biodegraders are delivered to in regard to the contaminant source also varies case by case. These are factors that can affect the portion of the contributions of different steps during the remediation process. Thus, the mathematical model was also tested at a higher flow rate as well as a longer spacing distance between the toluene and the biodegrader injection ports, and the effect of chemotaxis and contaminant uptake rate on bioremediation process were compared under such conditions.

Chapter 2. 2-D Microcosm Experiments

2.1. Introduction

An overview of this chapter is presented below. Three PpF1 strains are used in this study: *Pseudomonas putida* F1 wild type (PpF1 wild type) which has full capability of toluene uptake, *Pseudomonas putida* F1 single knockout strain (PpF1 (Δ to*dX*)) which has impaired toluene uptake capability, and *Pseudomonas putida* F1 triple knockout strain (PpF1 (Δ to*dX* Δ cym*D* Δ F*I*f*a*d*L*)), which has even higher degree of impaired toluene uptake capability. The wild type strain and two mutant strains were obtained from Bert van den Berg lab (Newcastle University, UK).

Before 2-D microcosm experiments were performed, growth of three types of PpF1 strains were compared both by culture on LR agar plate and by culture in LR liquid media where the toluene as the sole carbon source was supplied in the gas phase. Details were presented in Chapter 2.2.

In Chapter 2.4, 2-D microcosm experiments were first conducted in the absence of a toluene plume to establish the baseline migration behavior for the PpF1 wild type and PpF1 single knockout strains. In Chapter 2.5, subsequent 2-D microcosm experiments in the presence of toluene were designed for PpF1 wild type and PpF1 single knockout strains to test their response to low and high concentration of toluene. Lastly in Chapter 2.6, a new set of 2-D microcosm experiments were carried out for PpF1 triple knockout strain, following the same experimental design for PpF1 single knockout strain, to assess how different toluene uptake capability affect the PpF1 population growth and migration.

Table 2.1.1 Three types of PpF1 strains and genotype.

Strain genotype	Strain characteristic	Strain label
PpF1 wild type	PpF1 wild type	PpF1 f0
PpF1 ($\Delta todX$)	PpF1 single knockout strain	PpF1 f1
PpF1 ($\Delta todX\Delta cymD\Delta F1fadL$)	PpF1 triple knockout strain	PpF1 f3

2.2. Materials and methods

Growth of three types of PpF1 strains were compared both by culture on LR agar plate and by culture in LR liquid media where the toluene as the sole carbon source was supplied in the gas phase.

Growth rates of three PpF1 strains were compared by culture on an LR agar plate (prepared as described in **Appendix A6**) where toluene as the sole carbon source was supplied in the gas phase. A single colony of PpF1 wild type, PpF1 single knockout strain or PpF1 triple knockout strain was picked from an LB plate that had been stored in 4 °C then inoculated to 3 mL LB media in a tube. PpF1 cells were cultured in a shaking incubator overnight with a rotation rate of 150 rpm at 28 °C. The cells were harvested by centrifugation at 4,000 xg for 10 min and washed with autoclaved H₂O then harvested again. This washing step was repeated one more time. Then PpF1 cell concentration was adjusted to OD₅₉₀=1 with autoclaved H₂O. 5 uL of this cell suspension was dropped on an LR agar plate and streaked with an autoclaved inoculating loop. The inoculated LR plate was put in a sealed container wherein 50 uL of toluene was supplied in a 1.5 mL closed-cap microcentrifuge tube and incubated at 30 °C for 2 days before photos were taken. The microcentrifuge containing toluene was replaced every day.

Growth rates of three PpF1 strains were also tested by culture in liquid media for a more quantitative comparison than the visual observation on agar plate. PpF1 cells were first activated in LB media through tube culture then washed as mentioned above. Equal amounts of three types of PpF1 cells were inoculated separately to each autoclaved 100 mL duran bottle containing 25 mL LR liquid medium and 1 uL or 2 uL of toluene supplemented in an open-cap microcentrifuge tube, and cultured at a rotation rate of 180 rpm at 23-25 °C. Cell concentration was measured at wavelength of 590 nm after 16 h of

culture.

To prepare cells for 2-D microcosm experiments, a single colony of each PpF1 strain was picked from an LB agar plate that had been stored in 4 °C and inoculated into 3 mL LB liquid media in a tube. PpF1 cells were cultured in a shaking incubator overnight at a rotation rate of 150 rpm at 28 °C. Equal portions of each strain were then inoculated separately into 250 mL flasks containing 50 mL of growth media supplemented with toluene and cultured for 9 h under at a rotation rate of 150 rpm at room temperature. Then, cells were harvested by centrifugation at 4,000 xg for 10 min and washed with autoclaved deionized H₂O. This washing step was repeated one more time. Cell concentration was adjusted to OD₅₉₀= 0.5-1 with autoclaved running buffer that was used within the 2-D microcosm.

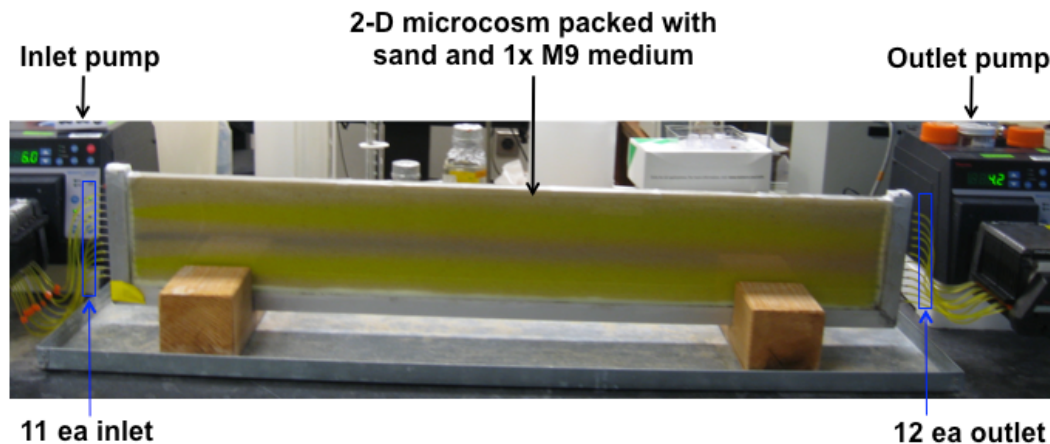


Figure 2.2.1 A 2-D microcosm was used in this study to mimic the natural groundwater system.

The 2-D microcosm experimental setup is shown in **Figure 2.2.1** (5). The 2-D microcosm mimics the contaminated groundwater system with water flowing steadily through the saturated sand-filled tank from one end to the other. The toluene plume is marked by co-

injection of a color indicator resazurin that appears purple and the PpF1 cell plumes are visible by co-injection with uranine, which appears yellow.

The 2-d microcosm had a Teflon base, Teflon end pieces, an aluminum frame, and two sheets of glass all sealed watertight with silicone glue wherein Ottawa sand was packed. The inner dimensions measured 95 cm x 14 cm x 1 cm and the apparatus sat on two wooden supports with a spill tray underneath. The inlet and outlet ends of the 2-D microcosm were equipped with twelve ports with a vertical spacing of 1 cm numbered 1 through 12 from top to bottom. Two-inch long stainless steel capillaries were fitted through the ports. The inflow and outflow capillaries extended 0.5 cm into the microcosm. The outflow capillaries were wrapped with 1 cm x 1 cm piece of steel woven wire fine mesh to prevent sediment from clogging the capillaries. The outer capillary tips were connected to PVC pump tubing links (PVC solvent/hydrocarbon tubing, two-stop, 0.89 mm ID), which ran through two twelve-channel Carter peristaltic precision pumps (Manostat Carter, Thermo Scientific), one for the inflow and another for the outflow. The pump was calibrated prior to each run so that the flow rate variance from each channel was less than 5%. The inlet ports were used to transfer the running buffer M9 media (47) from a 1L storage bottle into the microcosm. The effluent media pumped from the outlet ports was directed into the sample collection containers during sample collection period and otherwise to a hazardous waste collection container. The flow rate is controlled by both inflow and outflow pumps.

Prior to each experiment, the microcosm tank was rinsed with 0.3 M NaOH solution followed by autoclaved H₂O three times and then a last washing step with autoclaved M9 media. Before injection of any solution into the sand-packed microcosm, M9 medium was pumped through for at least 12 h to reach a steady flow, during which a stable water table was established below

a thin unsaturated layer on top of the microcosm. The flow rate was about 1.1 ~ 1.3 m/d, which is similar to the natural groundwater velocities (33).

In general, the PpF1 cell suspension and attractant solution will be continuously fed at different vertical locations. In this experiment, when two PpF1 cells were injected into the microcosm, port 7 was dedicated for M9 containing toluene and uranine, and port 4 and port 10 for different PpF1 strains. After traveling through the microcosm, various samples containing uranine, resazurin, resorufin, toluene, and PpF1 cells at the outlet were collected over a range of vertical positions for 2 h and their concentration distribution was analyzed by various analytical methods, which are detailed in the Appendices.

2.3. Comparison of cell growth

2.3.1. Comparison of cell growth on agar plate

As **Figure 2.3.1** shows, under the same culture condition, the PpF1 wild type exhibited greater growth rate than two PpF1 knockout strains, and PpF1 single knockout strain grew slightly faster than PpF1 triple knockout strain. Notice that both of the two knockout strains also had a slight growth in spite of the absence of the toluene-specific transport channels. According to van den Berg lab (Newcastle University, UK), this is due to leakage of toluene transport across the membrane via other pathways.

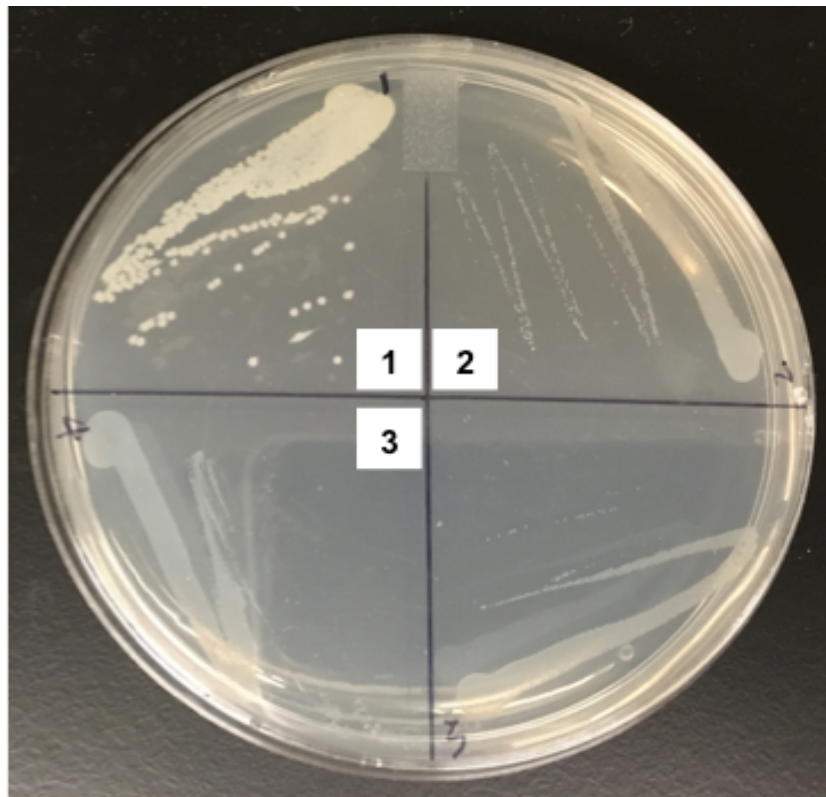


Figure 2.3.1 Comparison of growth of three PpF1 strains on LR agar plate where toluene was supplied in the gas phase. 1: PpF1 wild type; 2: PpF1 single knockout strain; 3: PpF1 triple knockout strain. The growth rate is in the order: PpF1 wild type > PpF1 single knockout strain > PpF1 triple knockout strain.

2.3.2. Comparison of cell growth in liquid media

For a more quantitative growth comparison than the visual observation on agar plate, growth rates of three PpF1 strains were also tested by culture in liquid media. Similar to the result from growth comparison on agar plate, in liquid media as well, the PpF1 wild type proliferated fastest, PpF1 triple knockout strain slowest, and PpF1 single knockout strain in between (**Table 2.3.1** and **Table 2.3.2**, **Figure 2.3.2**). Regardless of the lack of a certain trans-membrane toluene transport proteins, PpF1 knockout strains still showed a certain level of growth, implying that there are other pathways for toluene to be uptake by PpF1 cells.

Table 2.3.2.1 Cell density of three PpF1 strains measured after 16-hour culture in LR media with toluene supplied at gas phase

Strain	#	Toluene	OD ₅₉₀	Avr.	SD	CV
PpF1 wild type	f0-1	1 uL	0.113	0.097	0.011	12%
	f0-2	1 uL	0.091			
	f0-3	1 uL	0.097			
	f0-4	1 uL	0.087			
PpF1 single knockout	f1-1	1 uL	0.055	0.070	0.017	24%
	f1-2	1 uL	0.056			
	f1-3	1 uL	0.087			
	f1-4	1 uL	0.081			
PpF1 triple knockout	f3-1	1 uL	0.025	0.029	0.007	25%
	f3-2	1 uL	0.021			
	f3-3	1 uL	0.036			
	f3-4	1 uL	0.035			

Strain	#	Toluene	OD ₅₉₀	Avr.	SD	CV
PpF1 wild type	f0-1	2 uL	0.159	0.179	0.020	11%
	f0-2	2 uL	0.164			
	f0-3	2 uL	0.192			
	f0-4	2 uL	0.2			
PpF1 single knockout	f1-1	2 uL	0.076	0.090	0.015	16%
	f1-2	2 uL	0.079			
	f1-3	2 uL	0.101			
	f1-4	2 uL	0.105			
PpF1 triple knockout	f3-1	2 uL	0.047	0.045	0.024	53%
	f3-2	2 uL	0.02			
	f3-3	2 uL	0.068			

Table 2.3.2.2 Statistical analysis of growth rates of three PpF1 strains

	<i>p</i> -value	
	Toluene 1 uL	Toluene 2 uL
PpF1 wild type vs PpF1 single knockout	0.03560	0.000411
PpF1 wild type vs PpF1 triple knockout	0.00006	0.000491
PpF1 single knockout vs PpF1 triple knockout	0.00435	0.026710

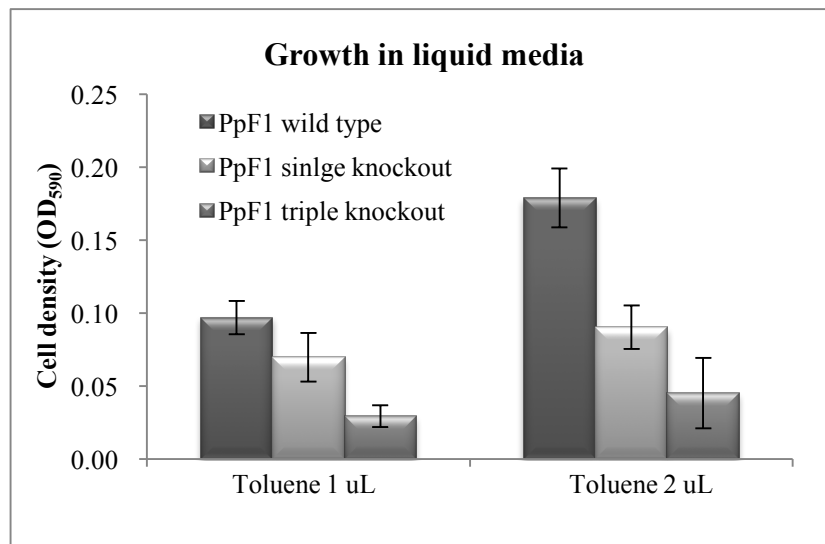


Figure 2.3.2.1 Comparison of growth of three PpF1 strains in liquid media. The growth rate is in the order: PpF1 wild type > PpF1 single knockout strain > PpF1 triple knockout strain. The growth rates of three PpF1 strains are statistically significant (*p*-value <0.05).

2.4. 2-D microcosm experiments: without toluene

2-D Microcosm experiments were first conducted in the absence of a toluene plume to establish the baseline migration behavior for the wild type and PpF1 single knockout strains. Each PpF1 cell suspension was fed continuously from an inlet port, and it was transported along with the continuous convective flow toward the outlet. Dispersion contributed to the spread of the plume vertical to the flow direction, such that the concentration yielded a Gaussian-shaped distribution at the outlet. Characterization of PpF1 cell distributions in the effluent was done with Gaussian fitting (details in the **Appendix A5**). The schemes and pictures of actual 2-D microcosm runs with PpF1 wild type and PpF1 single knockout strains are shown below.

In **Figure 2.4.2**, the distributions of PpF1 wild type and PpF1 single knockout strains are plotted side-by side for comparison. Uranine was co-injected with the bacteria as an internal control for the fluid flow behavior in the microcosm. The vertical position of the bacterial profiles was thus plotted relative to the uranine position for that particular experimental run to compensate for small variations in the fluid velocity between different microcosm trials. The uranine and PpF1 cell distribution profiles were subjected to Gaussian fitting (**Appendix A5**) to determine the peak center as well as the breadth of each peak. The peak center is indicated by the mean and the peak breadth by variance σ^2 . Fitting result is shown in **Table 2.4.1**. Comparing the center of mass relative to the uranine tracer, both PpF1 strains settled downward from the injection altitude, as their specific gravity was greater than unity. The settling velocity of both PpF1 strains appeared to be comparable as the center of mass shifted downward by about 1 cm for each strain.

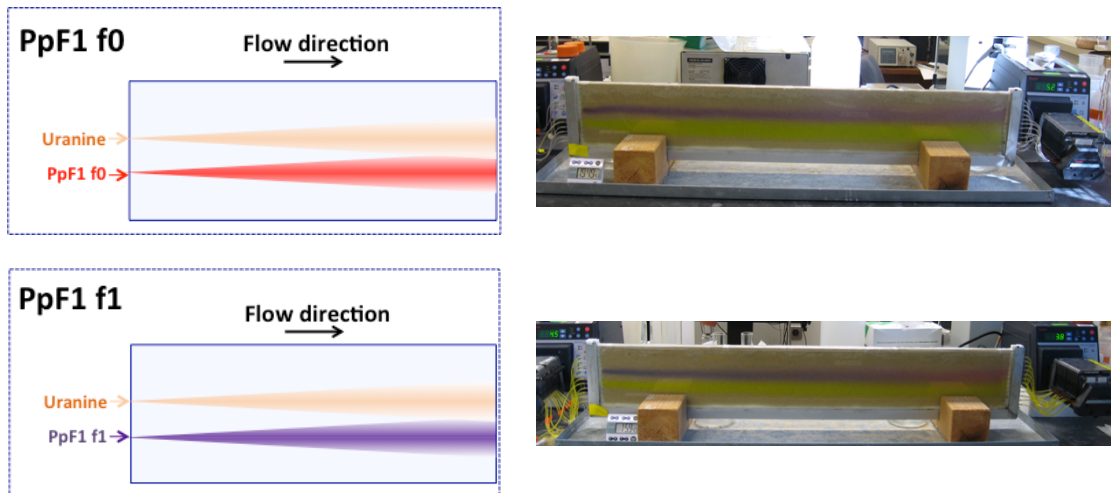


Figure 2.4.1 Schemes and pictures of 2-D microcosm runs without toluene.

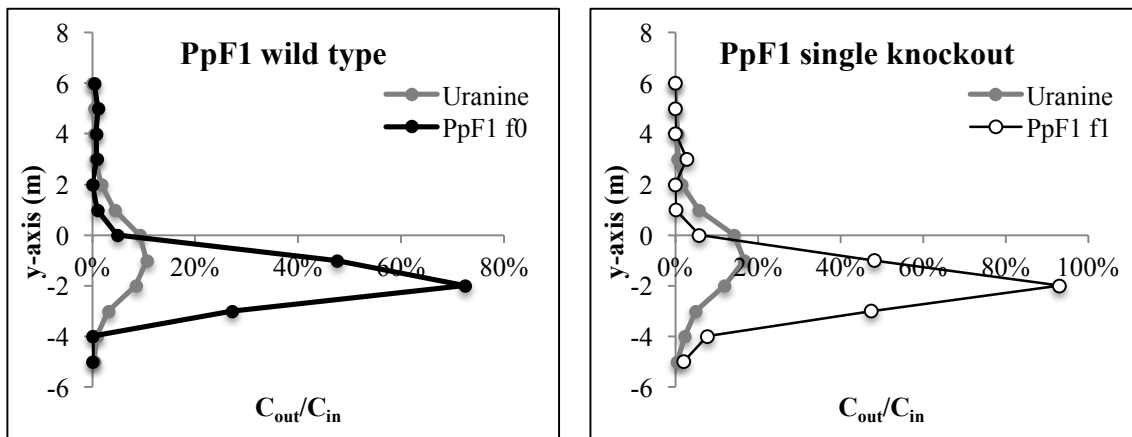


Figure 2.4.2 Concentration profiles of two bacterial strains, PpF1 wild type (PpF1 f0) and PpF1 single knockout strain (PpF1 f1) at the 2-D microcosm outlet. Uranine served as a tracer and internal control.

Table 2.4.1 Comparison of parameter values (mean μ and variance σ^2) from Gaussian fitting of uranine tracer concentration and bacterial cell counts in 2-D microcosm effluent samples for PpF1 wild type and PpF1 single knockout strain.

	PpF1 wild type		PpF1 single knockout	
	Uranine	Cell	Uranine	Cell
μ (cm)	0	-0.9	0	-1.1
σ^2 (cm ²)	2.0	0.7	1.8	0.8
Transverse dispersivity (cm)	0.0053	0.0018	0.0043	0.0022

A force balance on the cell accounting for Stokes drag yields $v_{settlement} = \frac{(\rho_P - \rho)gd_P^2}{18\mu}$, where $v_{settlement}$ is the theoretical settling velocity for a perfect sphere, ρ_P and d_P are the respective buoyant density and diameter of the particle, ρ is the fluid density, and μ is the dynamic fluid viscosity, and g is the acceleration due to gravity (48). Estimating $\rho_P = 1.11 \times 10^3 \text{ kg/m}^3$, $\rho = 1 \times 10^3 \text{ kg/m}^3$, $g = 9.8 \text{ m/s}^2$, $d_P = 1 \times 10^{-6} \text{ m}$, and $\mu = 1 \times 10^{-3} \text{ kg}\cdot\text{m}^{-1}\cdot\text{s}^{-1}$ (49), the calculated settling velocity is $v_{settlement} = 6.0 \times 10^{-8} \text{ m/s}$. Thus, over the averaged traveling time of 20 h, the settling distance is 0.39 cm, which is the same order of magnitude as the observed value 1 cm. The difference between the estimated and observed settling distances may be attributed to the idealized spherical shape as well as an underestimate of the cell diameter and the cell density that were used in the calculation.

Uranine recovery in the runs for PpF1 wild type and PpF1 single knockout strain were 39.8% and 58.3%, respectively, and the cell recovery after calibration by uranine yielded 391% and 355% for each of them.

Dispersivity was calculated as follows:

From the Einstein relationship, $D_T = \frac{\sigma^2}{2t}$, where D_T is the transverse diffusion coefficient, σ^2 is the second moment and t is the traveling time.

$D_T = \frac{D_{eff}}{\varepsilon} + \alpha_T v$, where D_{eff} is the effective diffusion coefficient, α_T is the dispersivity and v is the swimming speed. So, $\alpha_T = \frac{(\frac{\sigma^2}{2t} \frac{D_{eff}}{\varepsilon})}{v}$, where $t = 19$ h, $v = 1.55 \times 10^{-5}$ m/s, $\varepsilon = 0.37$, D_{eff} for uranine is 9.0×10^{-6} cm²/s and D_{eff} for a cell is 3.2×10^{-6} cm²/s. The transverse dispersivity for each analyte in each run is listed in **Table 6.1.1**.

These values are similar in magnitude to previously reported values of 0.0005-0.0012 cm for *E. coli* bacteria (31) and 0.004-0.010 for small molecules (38, 31, 32) from other microcosm set-ups and a smaller-scale microfluidics device. The vertical spread of both cell types as measured by the second moment was comparable to each other, and less than that of uranine. This is likely due to the larger size of cells than uranine molecules where the larger particles make less detours in transverse direction as they flow along with the streamlines (31, 50). The results from the moment analysis show the knockout of TodX from PpF1 doesn't have a significant effect on the cell transport during the microcosm run.

2.5. 2-D Microcosm experiments: low & high concentration of toluene

With toluene fed into the 2-D microcosm, two experimental configurations with two different toluene concentrations were studied as shown in **Figure 2.5.1** (Actual images in **Appendix A7.1** and **A7.2**). The lower concentration of toluene ($1\text{e-}5$ v/v) was fed for Run 1 and Run 2, and the higher concentration of toluene ($1\text{e-}4$ v/v) was fed for Run 3 and Run 4. For the same feed concentration of toluene, two different PpF1 strains - PpF1 wild type and PpF1 single knockout strain - were injected, with one above and the other below the toluene plume during the same run. Also a run where the positions were switched was also tested.

PpF1 strains were injected in a suspension without a carbon source. As cells moved horizontally together with the convective flow of buffer, dispersion as well as chemotaxis and settling due to gravity drove the vertical movement of cells toward or away from the toluene plume. Upon exposure to toluene, which serves as the sole carbon source for PpF1 cell survival and proliferation, the population growth of PpF1 single knockout strain was observed to be less than PpF1 wild type, due to the impaired toluene uptake capability.

To compare the difference of PpF1 wild type and PpF1 single knockout strain in growth rate, the percent recovery of cells at the effluent was analyzed and the results are listed in **Table 2.5.1**. Cell recovery was calibrated relative to the uranine recovery that was co-injected together with the cells. **Figure 2.5.2** shows a representative concentration profile of cell and uranine concentrations at the outlet using Run 3 as an example (others are in **Appendix A7.1** and **A7.2**). The area under each peak represents the quantity recovered of the corresponding analyte.

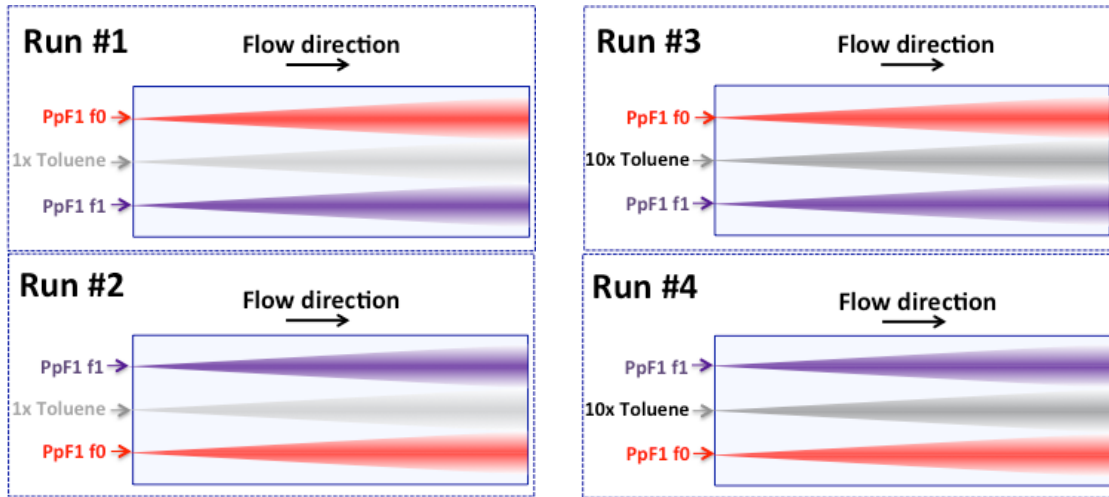


Figure 2.5.1 Configurations for four different microcosm runs with PpF1 wild type (PpF1 f0) and PpF1 single knockout strain (PpF1 f1).

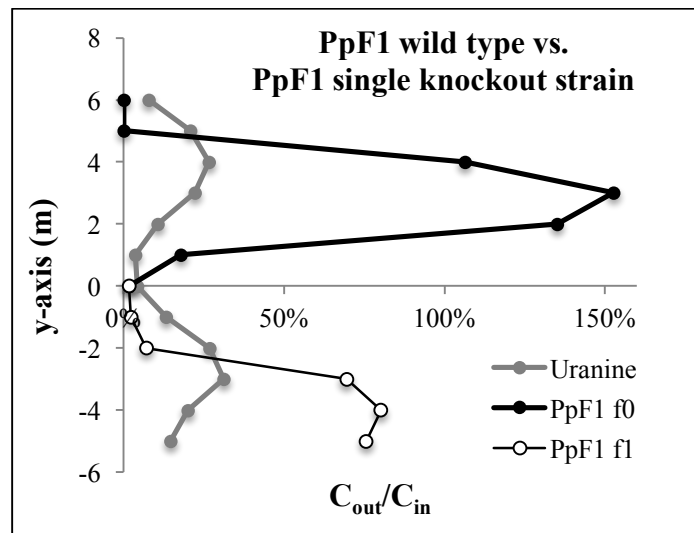


Figure 2.5.2 Concentration profiles of cells and uranine for microcosm Run 3. PpF1 wild type (PpF1 f0) was injected above the toluene plume and PpF1 single knockout strain (PpF1 f1) below the toluene plume.

Table 2.5.1 List of cell recovery data in four microcosm runs. The same shading/patterning represents the the same microcosm run, respectively. At the outlet of each microcosm run, cells were collected, counted, and calibrated to uranine recovery, then compared with the inlet concentration for the percent recovery calculation.

PpF1 strain	Injection location Above/Below toluene plume	% Recovery	
		1e-5 v/v	1e-4 v/v
PpF1 wild type	Above (top)	170%	431%
	Below (bottom)	232%	219%
PpF1 single knockout strain	Above (top)	86%	124%
	Below (bottom)	127%	213%

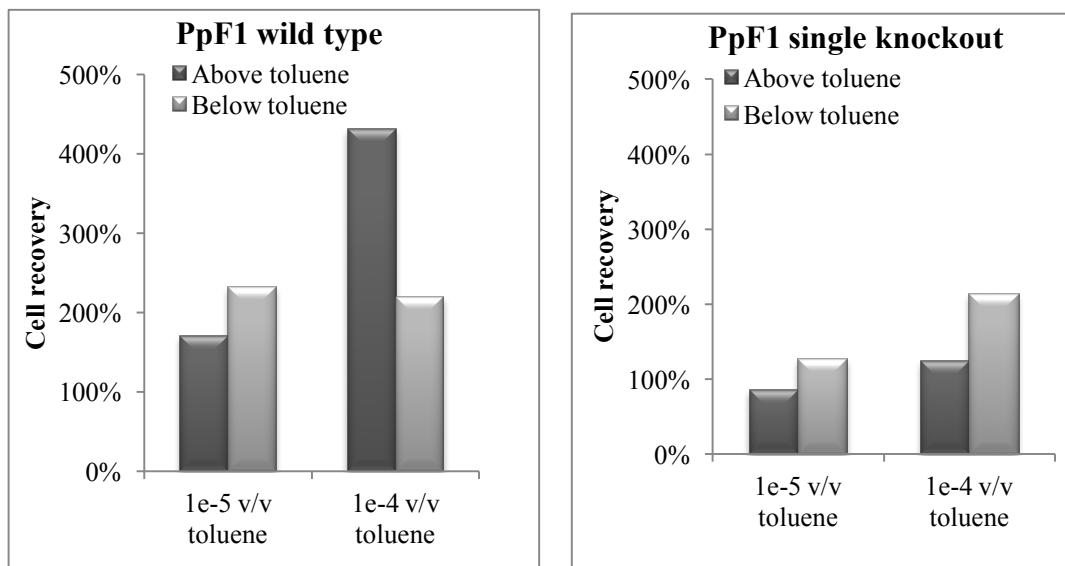


Figure 2.5.3 Plot of cell recovery for PpF1 wild type and PpF1 single knockout strain when injected above and below the toluene plume, both at low and high concentration of toluene.

In each microcosm run, PpF1 wild type recovery was greater than PpF1 single knockout strain: 170% vs. 127%, 232% vs. 86%, 431% vs. 213%, and 219% vs. 124% (**Table 2.5.1**). These results were as expected: the lack of TodX led to less uptake of toluene by the PpF1 single knockout strain (PpF1 (*ΔtodX*)) and consequently reduced population growth.

In comparing microcosm runs with low and high toluene concentration feed it was noted that: PpF1 wild type had higher recovery at higher toluene concentration, 431% vs. 170% when injected above the toluene plume; and a comparable percent recovery at high and low toluene concentration, 219% vs. 232% when injected below the toluene plume.

PpF1 single knockout strain had higher recovery at high toluene concentration 124% vs. 86% when injected above the toluene plume; and higher recovery at low toluene concentration 219% vs. 127% when injected below the toluene plume.

Overall, it was revealed that under the current experimental conditions mimicking the natural groundwater environment, PpF1 single knockout strain achieved lower population growth as compared with the wild type, and exposure of the PpF1 cells to a certain level of increased toluene concentration accelerated the cell population growth. It implies that the toluene uptake step can play an important role in bioremediation enhancement and also suggested the potential of engineering bacteria toward higher contaminant permeability for enhanced bioremediation efficiencies.

2.6. 2-D Microcosm experiments: three PpF1 strains

With PpF1 single knockout strain grew slower than PpF1 wild type in the microcosm when toluene served as the only carbon source over the run, the same set of experiments were conducted for another strain PpF1 triple knockout mutant, with exactly the same setting as 2-D microcosm runs with PpF1 single knockout strain which had more toluene uptake related transport proteins knocked out thus showed even lower growth rate on agar plate as well as in liquid media. The scheme was drawn in **Figure 2.6.1** and cell recovery at the 2-D microcosm outlets was measured and adjusted over the uranine recovery at the end of the experiments (concentration profiles in **Appendix A7**). The corresponding graph comparing cell recovery of three PpF1 strains was shown in **Figure 2.6.2**.

With $1e-4$ v/v toluene supply, when PpF1 strains were injected above the toluene plume, the cell recovery was in order of PpF1 wild type > PpF1 single knockout strain > PpF1 triple knockout strain. With $1e-4$ v/v toluene supply, when PpF1 strains were injected below the toluene plume, the cell recovery was in order of PpF1 wild type \approx PpF1 single knockout strain > PpF1 triple knockout strain. This is the same order as toluene uptake capability of three PpF1 strains, indicating that with the mass transfer barrier existing inside the microcosm, toluene uptake capability of PpF1 strains still played a dominant role in degrading toluene.



Figure 2.6.1 Configurations for two different microcosm runs with PpF1 wild type (PpF1 f0) and PpF1 triple knockout strain (PpF1 f3).

Table 2.6.1 List of cell recovery data for three PpF1 strains during 2-D microcosm experiments with $1e-4$ v/v toluene fed: PpF1 wild type (PpF1 f0), PpF1 single knockout strain (PpF1 f1) and PpF1 triple knockout strain (PpF1 f3). At the outlet of each microcosm run, cells were collected, counted, and calibrated to uranine recovery, then compared with the inlet concentration for the percent recovery calculation.

% Cell recovery			% Cell recovery		
Above $1e-4$ v/v toluene plume			Below $1e-4$ v/v toluene plume		
PpF1 f0	PpF1 f1	PpF1 f3	PpF1 f0	PpF1 f1	PpF1 f3
435%	124%	96%	209%	213%	58%

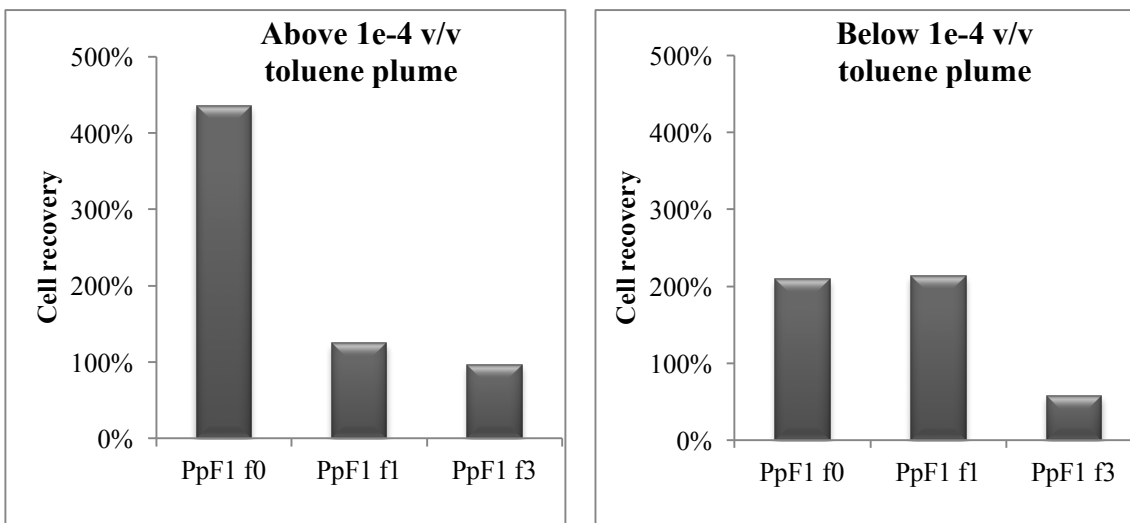


Figure 2.6.2 Plot of cell recovery for three PpF1 strains: PpF1 wild type (PpF1 f0), PpF1 single knockout strain (PpF1 f1) and PpF1 triple knockout strain (PpF1 f3), when $1e-4$ v/v of toluene was fed. Recovery was plotted both when PpF1 strains were injected above and below the toluene plume.

2.7. 2-D Microcosm experiments: toluene analysis

Toluene quantity was measured from two 2-D microcosm experiments: one from abiotic run where no bacterial cells were introduced into the 2-D microcosm and the other from the biotic run #6 from chapter 2.6. Toluene concentration profiles from two microcosm runs were shown below in **Figure 2.7.1**. The toluene recovery from abiotic run summed up to 8.9% whereas toluene recovery from run #6 summed up to 1.1%, the difference being 7.8%. A great loss of toluene from abiotic experiments was observed, indicating that either that toluene was trapped within the microcosm or that the loss occurred during quantification process, or both.

To calculate the conversion factor of those produced daughter bacterial cells from toluene consumption over the inlet bacterial cells:

$$\begin{aligned} \# &= \frac{Area_{inlet, toluene} \times V_f \times \varepsilon \times C_{toluene} \times Y_b \times 7.8\%}{Area_{inlet, bacteria} \times V_f \times \varepsilon \times b_0} = \frac{C_{toluene} \times Y_b \times 7.8\%}{b_0} \\ &= \frac{0.944 \times 9.98e-9 \times 0.078 \frac{mol}{s}}{5.8e-10 \frac{mol}{s}} = 1.27 \end{aligned}$$

This is number less than the maximum recovery of bacterial cells from 2-D microcosm outlet (433%). One reason could be that toluene experienced reversible absorption with the sands inside the 2-D microcosm thus provided more carbon-energy source when bacterial cells were injected into the system than 7.8% as calculated above.

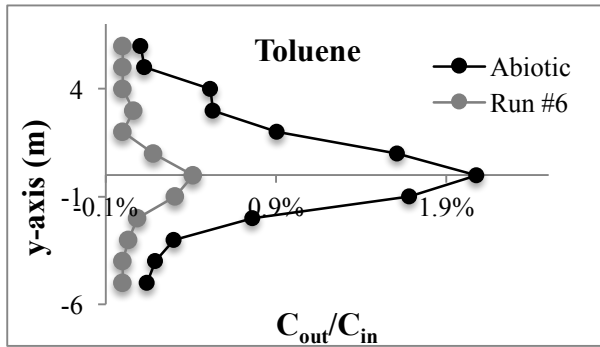


Figure 2.7.1 Toluene profiles at the microcosm outlet from an abiotic experiment and Run #6.

2.8. Reproducibility

Reproducibility was tested with uranine recovery from Run #1 – Run #6. In regard to the asymmetric flow pattern between the top and bottom part of the microcosm, uranine recovery was averaged for each part separately. The averaged data and corresponding graph was shown below (**Table 2.8.1** and **Figure 2.8.1**), which confirmed an acceptable fluctuation.

Furthermore, Run #5 was repeated and the reproducibility of cell recovery was tested in addition to uranine recovery. (**Table 2.8.2** and **Figure 2.8.2**) The fluctuation range was about 8% of averaged cell recovery value for PpF1 wild type, and 24% for PpF1 triple knockout strain. The higher number is primarily due to low recovery of PpF1 triple knockout strain at the outlet.

Table 2.8.1 Averaged uranine recovery data.

Uranine (n=5)			
	Mean	SD	CV
Top	83.1%	0.1412	17%
Bottom	94.8%	0.1682	18%

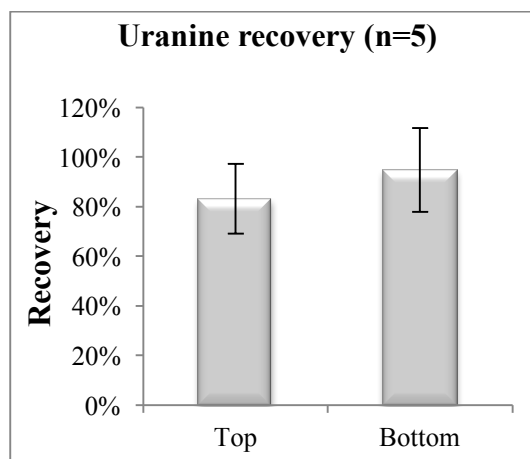


Figure 2.8.1 Averaged uranine recovery.

Table 2.8.2 Averaged PpF1 cell recovery data.

Cell recovery (n=2)			
	Mean	SD	CV
PpF1 f0 (top)	437%	35%	8%
PpF1 f3 (bottom)	96%	24%	24%

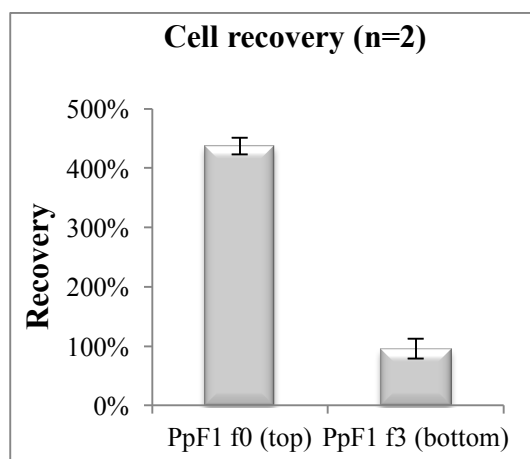


Figure 2.8.2 Averaged PpF1 cell recovery over 2 runs. PpF1 f0 was injected 1e-4 v/v toluene plume and PpF1 f3 below.

Chapter 3. Computational Simulation

3.1. Introduction

To evaluate how the cell growth/death and mass transfer (chemotaxis) parameters separately affect the overall toluene consumption rate, a mathematical model was set up to quantitatively describe the transport phenomena occurring inside the 2-D microcosm. Comparison of the numerical solutions of these mathematical equations to the experimental observations will facilitate the evaluation of the impact of various parameters on bioremediation efficiency under this natural-groundwater-mimicking condition and thus the sensitivity of bioremediation efficiency to each of these parameters. Therefore, it allows us to compare the extent to which the bioremediation is dependent on the contaminant uptake step, which is related with bacterial cell growth rate, with the delivery of bacterial cells to the contaminated site. The established model could further be utilized to predict the behavior of bacterial cells and toluene with various parameter settings under non-tested conditions, and ultimately provide assistance in practical *in situ* bioremediation.

To this end, the governing equations explaining all processes including advection, dispersion, chemotaxis, bacterial cell growth/death, bacterial settling, and toluene/oxygen consumption terms were established in preparation for analysis with finite element analysis software COMSOL Multiphysics®. “Time dependent” mode was used and the computation was stopped at 19 h after initiation which was the median time point of sample collection period in experiments (18 h – 20 h). “Steady state” mode was used later to represent the condition that are closer to the real world scenario.

In this chapter, a representative simulation results were first shown matching the experimental results where the highest bacterial cell recovery were observed in experiments, and these parameters were used as a basis for subsequent simulations. To qualitatively compare the effect of chemotaxis and bacterial cell growth/death on the fate of bacterial cells as well as toluene during experiments, four combinatorial sets of simulation runs were performed where chemotaxis and bacterial cell growth/death terms were or were not incorporated in the model. Next, for a quantitative comparison, parametric analysis was done to figure out how much sensitively the bacterial cell recovery and toluene recovery responded to each of the parameters involved in chemotaxis (chemotaxis sensitivity coefficient $\chi_{0,eff}$ and chemotactic receptor binding constant K_c) and bacterial growth/death (maximum specific growth rate μ_{max} and half saturation constant K_a). With these results, moment analysis was done with bacterial cell recovery to further study how these parameters influenced the transfer and consumption of toluene by bacteria. In regard to the previous studies that insufficient oxygen supply has well known to impede the bioremediation process by aerobic remediating bacteria, simulations were performed with incorporating or not incorporating oxygen consumption terms in the model, followed by simulations at various oxygen concentrations to study its effect. Finally, simulations were done with increased spacing between bacterial cells and toluene source, and also with increased flow rate, in which the effect of chemotaxis and bacterial growth/death under these conditions were evaluated and compared with current experimental setting.

3.2. Mathematical model

A mathematical model (**Equation 3.2.1 – 3.2.3**) was set up to represent the transport phenomena inside the microcosm. In addition to bacterial cells (b) and toluene (a), oxygen (o) was also taken into consideration because insufficient oxygen availability has been observed to significantly limit the bioremediation efficiency by previous studies (54). The governing equations are listed below. These partial differential equations were solved by finite element analysis software COMSOL Multiphysics[®], with the microcosm simulation configured to match the experimental setup. Parameter values were either referenced from other studies or measured and calculated in this study (**Table 3.2.1**).

$$R \frac{\partial b}{\partial t} = D_{bx} \frac{\partial^2 b}{\partial x^2} + D_{by} \frac{\partial^2 b}{\partial y^2} - V_f \frac{\partial b}{\partial x} + \left(\frac{o}{o + K_o} \frac{\mu_{max} a}{K_a + a} \right) b - k_{decay} b - \frac{\partial(V_{chx} b)}{\partial x} - \frac{\partial(V_{chy} b)}{\partial y} - v_{set} \frac{\partial b}{\partial y} \quad (3.2.1)$$

$$\frac{\partial a}{\partial t} = D_{ax} \frac{\partial^2 a}{\partial x^2} + D_{ay} \frac{\partial^2 a}{\partial y^2} - V_f \frac{\partial a}{\partial x} - \frac{o}{o + K_o} \frac{q_a a}{(K_a + a)} b \quad (3.2.2)$$

$$\frac{\partial o}{\partial t} = D_{ox} \frac{\partial^2 o}{\partial x^2} + D_{oy} \frac{\partial^2 o}{\partial y^2} - V_f \frac{\partial o}{\partial x} - \frac{q_o o}{(o + K_o)} \frac{a}{(K_a + a)} b \quad (3.2.3)$$

where b is bacterial cell concentration, a is the toluene concentration (attractant/carbon and energy source), o is the electron acceptor oxygen concentration, t is time, x is the distance longitudinally in the direction of buffer flow along the microcosm, y is the transverse distance to the x axis with $x = 0$ located at the center of the toluene injection zone, R is retardation factor which accounts for sorption, V_f is average interstitial velocity, D_{bx} is longitudinal dispersion coefficient for bacterial cell, D_{by} is transverse dispersion coefficient for bacterial cell, D_{ax} is longitudinal dispersion coefficient for toluene, D_{ay} is transverse dispersion coefficient for toluene, D_{ox} is longitudinal dispersion coefficient for oxygen, D_{oy} is transverse dispersion coefficient for oxygen, μ_{max} is maximum specific growth rate of the bacterial cell on toluene, $\mu_{max,o}$ is maximum specific growth rate of the bacterial cell on oxygen, K_a is half saturation constant for bacterial cell growth on toluene, K_o is half saturation constant for bacterial

cell growth on oxygen, k_{decay} is bacterial cell decay rate, V_{Chx} is longitudinal chemotactic velocity, V_{Chy} is transverse chemotactic velocity, v_{set} is bacterial cell settling velocity due to higher gravity than buffer, $Y_{b/a}$ is yield coefficient of the bacterial cell on toluene, the maximum toluene consumption rate $q_a = \mu_{max}/Y_{b/a}$, $Y_{b/o}$ is yield coefficient of the bacterial cell on oxygen, and the maximum oxygen consumption rate $q_o = \mu_{max,o}/Y_{b/o}$. (51)

The dispersion coefficients are defined by:

$$D_{ix} = \frac{D_{diff,i}}{\varepsilon} + \alpha_{ix}V_f, (i = a, b, o) \quad (3.2.4)$$

$$D_{iy} = \frac{D_{diff,i}}{\varepsilon} + \alpha_{iy}V_f, (i = a, b, o) \quad (3.2.5)$$

where i represents each species, D_{ix} is longitudinal dispersion coefficient of i , D_{iy} is transverse dispersion coefficient of i , $D_{diff,i}$ is diffusion coefficient of i , α_{ix} is longitudinal dispersivity of i , and α_{iy} is transverse dispersivity of i .

The chemotactic velocity terms V_{Chx} and V_{Chy} are defined by (48):

$$V_{Chx} = \frac{2}{3}v_b \tanh\left(\frac{\chi_{0,eff}}{2v_b} \frac{K_c}{(K_c + a)^2} \frac{\partial a}{\partial x}\right) \quad (3.2.6)$$

$$V_{Chy} = \frac{2}{3}v_b \tanh\left(\frac{\chi_{0,eff}}{2v_b} \frac{K_c}{(K_c + a)^2} \frac{\partial a}{\partial y}\right) \quad (3.2.7)$$

where v_b is bacterial cell swimming speed, $\chi_{0,eff}$ is chemotaxis sensitivity coefficient and K_c is chemotactic receptor binding constant.

The 2-D microcosm was configured such that a tank with the dimensions 95 cm (x - axis) \times 13 cm (y - axis) was represented as a homogeneous porous medium with a void fraction of 0.37 (52). Flow direction was from left to right, so all inlets were located on the left side of the microcosm and outlets on the right.

Boundary conditions:

No-flux boundary conditions were used for the upper and lower boundaries of the model. The outlet boundary condition was set as $-\mathbf{n} \cdot D_i \cdot \nabla c_i = 0$, which means the species passing this boundary was pulled out via convective flux. Toluene with concentration of a_0 and bacterial cell with concentration of b_0 were injected continuously from the designated inlets of 2-D microcosm with a width of 1 cm, the width which was experimentally indicated by the color tracer uranine at the inlet once it entered the 2-D microcosm from inlet tubings.

Initial conditions (@ t=0):

Toluene concentration: $a = 0$ ($0 \leq x \leq 95 \text{ cm}, -6.5 \text{ cm} \leq y \leq 6.5 \text{ cm}$)

Bacterial cell concentration: $b = 0$ ($0 \leq x \leq 95 \text{ cm}, -6.5 \text{ cm} \leq y \leq 6.5 \text{ cm}$)

Oxygen concentration: $o = o_0$ ($0 \leq x \leq 95 \text{ cm}, -6.5 \text{ cm} \leq y \leq 6.5 \text{ cm}$)

Toluene concentration, the sole carbon and energy source, was initially set as 0 throughout the 2-D microcosm system, and it started to enter the system from designated inlet at a concentration of a_0 when the computation was initiated. Similarly, bacterial cell concentration was initially set as 0 throughout the 2-D microcosm system, and they started to enter the system from designated inlet(s) at a concentration of b_0 when the computation was initiated. Oxygen concentration, the electron acceptor, was initially set as its saturated concentration o_0 throughout the 2-D microcosm system, and it started to enter the system from all inlets at its saturated concentration when the computation was initiated.

To compare the effect of chemotaxis and bacterial cell growth/death, the governing equations were modified and were listed below. Boundary conditions and initial conditions remain the same.

The governing equations when chemotaxis was not applied:

$$\begin{array}{c}
 \text{Growth /} \\
 \text{Accum.} \quad \text{Dispersion} \quad \text{Advection} \quad \text{Consumption} \quad \text{Decay} \quad \text{Settling} \\
 R \frac{\partial b}{\partial t} = D_{bx} \frac{\partial^2 b}{\partial x^2} + D_{by} \frac{\partial^2 b}{\partial y^2} - V_f \frac{\partial b}{\partial x} + \left(\frac{o}{o + K_o} \frac{\mu_{max} a}{K_a + a} \right) b - k_{decay} b - v_{set} \frac{\partial b}{\partial y}
 \end{array} \quad (3.2.8)$$

$$\frac{\partial a}{\partial t} = D_{ax} \frac{\partial^2 a}{\partial x^2} + D_{ay} \frac{\partial^2 a}{\partial y^2} - V_f \frac{\partial a}{\partial x} - \frac{o}{o + K_o} \frac{q_a a}{(K_a + a)} b \quad (3.2.9)$$

$$\frac{\partial o}{\partial t} = D_{ox} \frac{\partial^2 o}{\partial x^2} + D_{oy} \frac{\partial^2 o}{\partial y^2} - V_f \frac{\partial o}{\partial x} - \frac{q_o o}{(o + K_o)} \frac{a}{(K_a + a)} b \quad (3.2.10)$$

The governing equations when bacterial cell growth/death was not applied:

$$\begin{array}{c}
 \text{Accum.} \quad \text{Dispersion} \quad \text{Advection} \quad \text{Chemotaxis} \quad \text{Settling} \\
 R \frac{\partial b}{\partial t} = D_{bx} \frac{\partial^2 b}{\partial x^2} + D_{by} \frac{\partial^2 b}{\partial y^2} - V_f \frac{\partial b}{\partial x} - \frac{\partial(V_{chx} b)}{\partial x} - \frac{\partial(V_{chy} b)}{\partial y} - v_{set} \frac{\partial b}{\partial y}
 \end{array} \quad (3.2.11)$$

$$\frac{\partial a}{\partial t} = D_{ax} \frac{\partial^2 a}{\partial x^2} + D_{ay} \frac{\partial^2 a}{\partial y^2} - V_f \frac{\partial a}{\partial x} \quad (3.2.12)$$

$$\frac{\partial o}{\partial t} = D_{ox} \frac{\partial^2 o}{\partial x^2} + D_{oy} \frac{\partial^2 o}{\partial y^2} - V_f \frac{\partial o}{\partial x} \quad (3.2.13)$$

The governing equations when bacterial cell growth/death and chemotaxis were not applied:

$$\begin{array}{c}
 \text{Accum.} \quad \text{Dispersion} \quad \text{Advection} \quad \text{Settling} \\
 R \frac{\partial b}{\partial t} = D_{bx} \frac{\partial^2 b}{\partial x^2} + D_{by} \frac{\partial^2 b}{\partial y^2} - V_f \frac{\partial b}{\partial x} - v_{set} \frac{\partial b}{\partial y}
 \end{array} \quad (3.2.14)$$

$$\frac{\partial a}{\partial t} = D_{ax} \frac{\partial^2 a}{\partial x^2} + D_{ay} \frac{\partial^2 a}{\partial y^2} - V_f \frac{\partial a}{\partial x} \quad (3.2.15)$$

$$\frac{\partial o}{\partial t} = D_{ox} \frac{\partial^2 o}{\partial x^2} + D_{oy} \frac{\partial^2 o}{\partial y^2} - V_f \frac{\partial o}{\partial x} \quad (3.2.16)$$

To evaluate the effect of oxygen during the 2-D microcosm runs, a mathematical model without incorporating oxygen into the process was also established, wherein it was assumed that oxygen was supplied with sufficient amount and replenished immediately where it was consumed. The governing equations were listed below:

$$\begin{array}{cccccc}
 & & \text{Growth /} & & & \\
 \text{Accum.} & \text{Dispersion} & \text{Advection} & \text{Consumption} & \text{Decay} & \text{Chemotaxis} & \text{Settling} \\
 R \frac{\partial b}{\partial t} = & D_{bx} \frac{\partial^2 b}{\partial x^2} + D_{by} \frac{\partial^2 b}{\partial y^2} - V_f \frac{\partial b}{\partial x} + \left(\frac{\mu_{max} a}{K_a + a} \right) b - k_{decay} b - \frac{\partial(V_{Chx} b)}{\partial x} - \frac{\partial(V_{Chy} b)}{\partial y} - v_{set} \frac{\partial b}{\partial y} & & & & &
 \end{array} \quad (3.2.17)$$

$$\frac{\partial a}{\partial t} = D_{ax} \frac{\partial^2 a}{\partial x^2} + D_{ay} \frac{\partial^2 a}{\partial y^2} - V_f \frac{\partial a}{\partial x} - \frac{q_a a}{K_a + a} b \quad (3.2.18)$$

Boundary conditions and initial conditions remained the same, except that oxygen part was excluded from the model.

The parameters used in this simulation were listed in **Table 3.2.1**. The calculations of several parameter values in this study were attached in **Appendix A8**.

Table 3.2.1 Parameter values used in COMSOL simulation

Symbol	Physical meaning	Value
a_0	injected toluene concentration	0.94 [mol/m ³]
b_0	injected bacterial concentration	5.80 e-10 [mol/m ³]
o_0	injected oxygen concentration	1.25 e-3 [mol/m ³]
$D_{a,bulk}$	bulk diffusion coefficient for toluene	9.00 e-10 [m ² /s]
$D_{b,bulk}$	bulk diffusion coefficient for bacterial cell	3.20 e-10 [m ² /s]
$D_{o,bulk}$	bulk diffusion coefficient for oxygen	1.97 e-9 [m ² /s]
D_{ax}	longitudinal dispersion coefficient for toluene	1.53 e-8 [m ² /s]
D_{ay}	transverse dispersion coefficient for toluene	1.58 e-9 [m ² /s]
D_{bx}	longitudinal dispersion coefficient for bacterial cell	4.66 e-9 [m ² /s]
D_{by}	transverse dispersion coefficient for bacterial cell	5.12 e-10 [m ² /s]
D_{ox}	longitudinal dispersion coefficient for oxygen	1.60 e-8 [m ² /s]
D_{oy}	transverse dispersion coefficient for oxygen	2.35 e-9 [m ² /s]
K_a	half saturation constant, growth on toluene	1.50 e-1 [mol/m ³]
K_c	chemotaxis receptor binding constant	1 [mol/m ³]
k_{decay}	bacterial cell decay rate	1.27 e-5 [1/s]
K_o	half saturation constant, growth on oxygen	1.25 e-2 [mol/m ³]
q_a	maximum reaction rate of toluene	1.05 e4 [mol /mol cell s]
q_o	maximum reaction rate of oxygen	9.60 e4 [mol /mol cell s]
R	retardation factor	1
U_{avg}	apparent flow rate	5.74 e-6 [m/s]
v_b	bacterial cell swimming speed	4.4 e-5 [m/s]
V_f	average interstitial velocity	1.55 e-5 [m/s]
v_{set}	bacterial cell settling velocity due to gravity	6.04 e-8 [m/s]
$Y_{b/a}$	yield coefficient of the bacterial cell on toluene	9.98e-9 [mol/mol]
α_{ax}	longitudinal dispersivity for toluene	9.41 e-4 [m]
α_{ay}	transverse dispersivity for toluene	6.00 e-5 [m]
α_{bx}	longitudinal dispersivity for bacterial cell	2.85 e-4 [m]
α_{by}	transverse dispersivity for bacterial cell	1.82 e-5 [m]
α_{ox}	longitudinal dispersivity for oxygen	9.41 e-4 [m]
α_{oy}	transverse dispersivity for oxygen	6.00 e-5 [m]
ξ	porosity	0.37
μ_{max}	maximum specific growth rate of cell on toluene	1.05 e-4 [1/s]
$\chi_{0,eff}$	chemotactic sensitivity coefficient	5 e-10 [m ² /s]

3.3. COMSOL simulation: A representative result

In this chapter, a representative simulation result was presented, which was matched to the experimental result where highest bacterial cell recovery was observed. For this purpose, three parameters q_a , q_o , and k_{decay} that were related with bacterial cell growth were scaled down to 0.22x of their reference values. These values were subsequently used as a basis for future simulations in this study.

Simulation was done in “time dependent” mode and was stopped at 19 h after the computation was initiated. For a comparison, “steady state” mode was also conducted and presented in parallel. Buffers carrying toluene, bacterial cells and oxygen were injected from the inlet located on the left side of the 2-D microcosm. Toluene was injected from the center inlet ($y = 0$ m), and bacterial cells were from the inlet located 3 cm above the toluene ($y = 0.03$ m). Oxygen was injected from all inlets.

A representative simulation result was shown in **Figure 3.3.1 – 3.3.3**, where the distribution of toluene, bacterial cells, and oxygen within the 2-D microcosm were shown as a function of time (0 h, 5 h, 10 h, 15 h, 18 h, 19 h, 20 h, and at steady state). Note that the sampling time during experiments were 18 h – 20 h. The concentration profiles of these species at inlet as well as at outlet were plotted as a function of time (**Figure 3.3.1** (J) and (K), **Figure 3.3.2** (J) and (K), **Figure 3.3.3** (J) and (K)).

For all species (toluene, bacterial cells, and oxygen), the convective flow carried them from left to right along x direction. At the same time, dispersion caused the transport of these species in the transverse y direction. Eventually, both toluene and bacterial cells form a fan-like plume with the highest concentration along y-axis located at the center of injection inlet (assuming only advection and dispersion were involved). Initially, though

the bacterial cells and toluene were distant to each other close to the inlet, they eventually would meet within the 2-D microcosm after a certain amount of time of travelling. Once the bacterial cells got exposure to toluene, two processes proceeded simultaneously: the bacterial cells sensed the gradient of toluene and the chemotaxis drove them to swim toward the center of the toluene plume where more toluene was present; at the same time, the bacterial cells started to uptake toluene which they used for survival and growth.

Figure 3.1.1 (D) and (K) shows that toluene started to come out of the 2-D microcosm from approximately 15 h after the computation was initiated. As time went, more and more toluene came out which was shown as increased C_{out}/C_{in} value. Additionally, as toluene was consumed by more and more bacterial cells as a function of time, an increased asymmetry of toluene peaks were observed in **Figure 3.1.1** (K): plots for 15 h, 18 h, 19 h, 20 h and steady state. Less toluene were recovered from top half-section ($y > 0$) of the 2-D microcosm than the bottom half-section ($y < 0$), and this is clearly shown in the region close to the outlet.

For bacterial cells, increased concentration started to appear from approximately 15 h after the computation was initiated, as shown by combined colors of green, yellow, and red in **Figure 3.1.2** (D) - (H). Before 15 h, the color of the bacterial cell plume got slightly dimmed due to the death in the absence of carbon/energy source (toluene in this case). As bacterial cells got exposed to more and more toluene as they traveled toward the outlet, a significantly increased bacterial cell concentration was observed close to the outlets. Similar to toluene, skewed bacterial cell peaks were observed in the region close to the outlet, due to the chemotaxis as well as increased bacterial cell growth where they got exposure to higher concentration of toluene (close to $y = 0$ m).

For oxygen, initially oxygen were homogeneously present at its saturation concentration throughout the 2-D microcosm (**Figure 3.1.3 (A) and (J)**). The bacterial cells started to grow after they got exposure to toluene, wherein the oxygen also started to be consumed. So, a region with decreased oxygen concentration started to appear from approximately 15 h after injection (**Figure 3.1.3 (D) - (H)**). In **Figure 3.1.3 (K)**, oxygen peak started to occur approximately after 15 h, and the concentration decreased further as a function of time, due to consumption by more and more bacterial cells. The peak position located approximately at the same position as the peak for bacterial cells, indicating oxygen was consumed most quickly where most bacterial cells were present.

As shown in **Figure 3.3.1 (K)**, **Figure 3.3.2 (K)**, and **Figure 3.3.3 (K)**, a slight difference in the distributions of toluene, bacterial cells and oxygen at the outlet between 19 h and steady state indicated that at 19 h after the initiation of the computation, the system hasn't reached steady state yet, yet the differences were not very significant.

Toluene

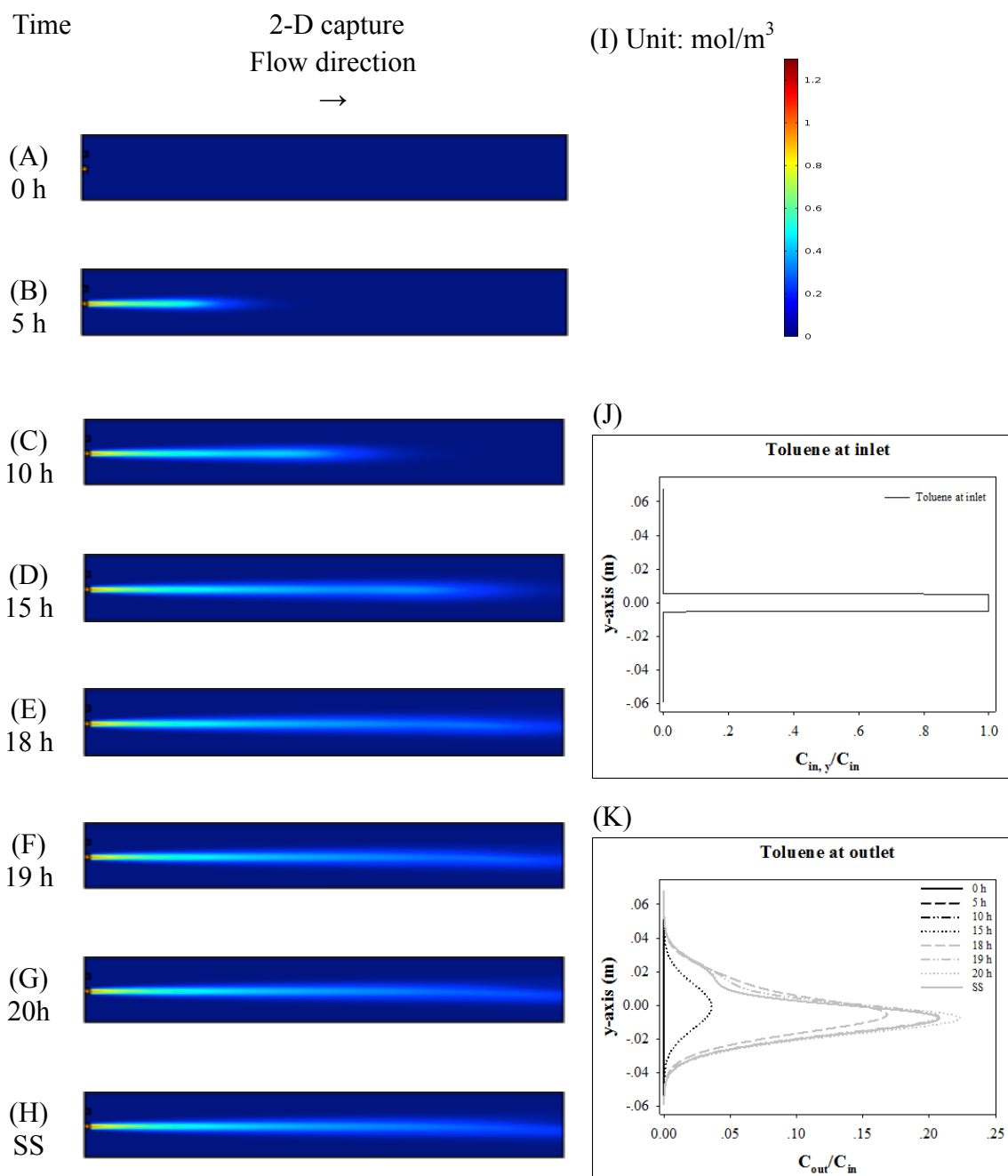


Figure 3.3.1 COMSOL simulation results with bacterial cell growth/death and chemotaxis terms applied: distribution of toluene within the microcosm as a function of time. (A) 0 h; (B) 5 h; (C) 10 h; (D) 15 h; (E) 18 h; (F) 19 h; (G) 20 h after injection; (H) steady state; (I) scale bar for (A)-(H); (J) toluene concentration profile at inlet; (K) toluene concentration profile at outlet of the microcosm as a function of time.

Bacterial cell

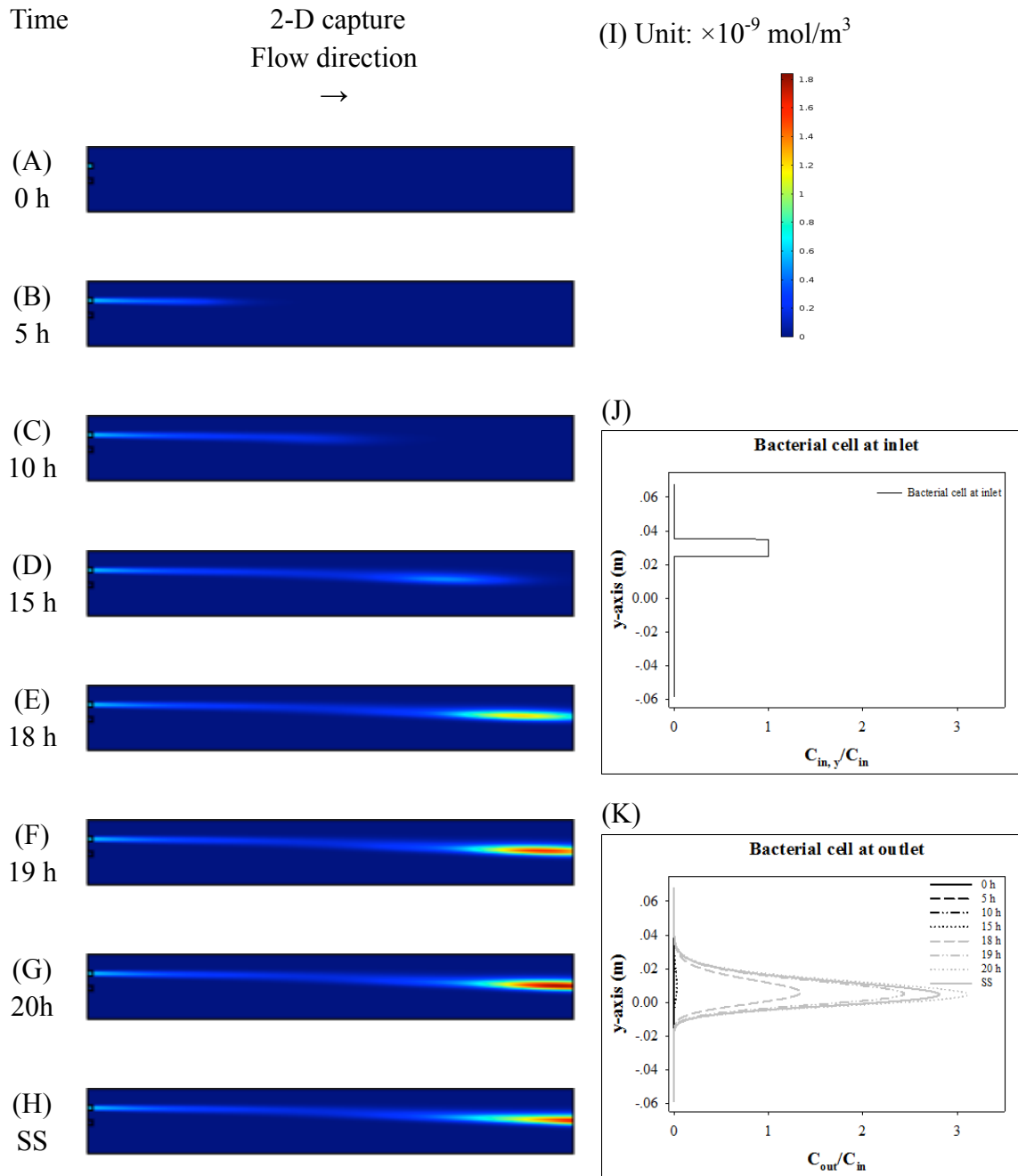


Figure 3.3.2 COMSOL simulation results with bacterial cell growth/death and chemotaxis terms applied: distribution of bacterial cells within the microcosm as a function of time. (A) 0 h; (B) 5 h; (C) 10 h; (D) 15 h; (E) 18 h; (F) 19 h; (G) 20 h after injection; (H) steady state; (I) scale bar for (A)-(H); (J) bacterial cell concentration profile at inlet; (K) bacterial cell concentration profile at outlet of the microcosm as a function of time.

Oxygen (O_2)

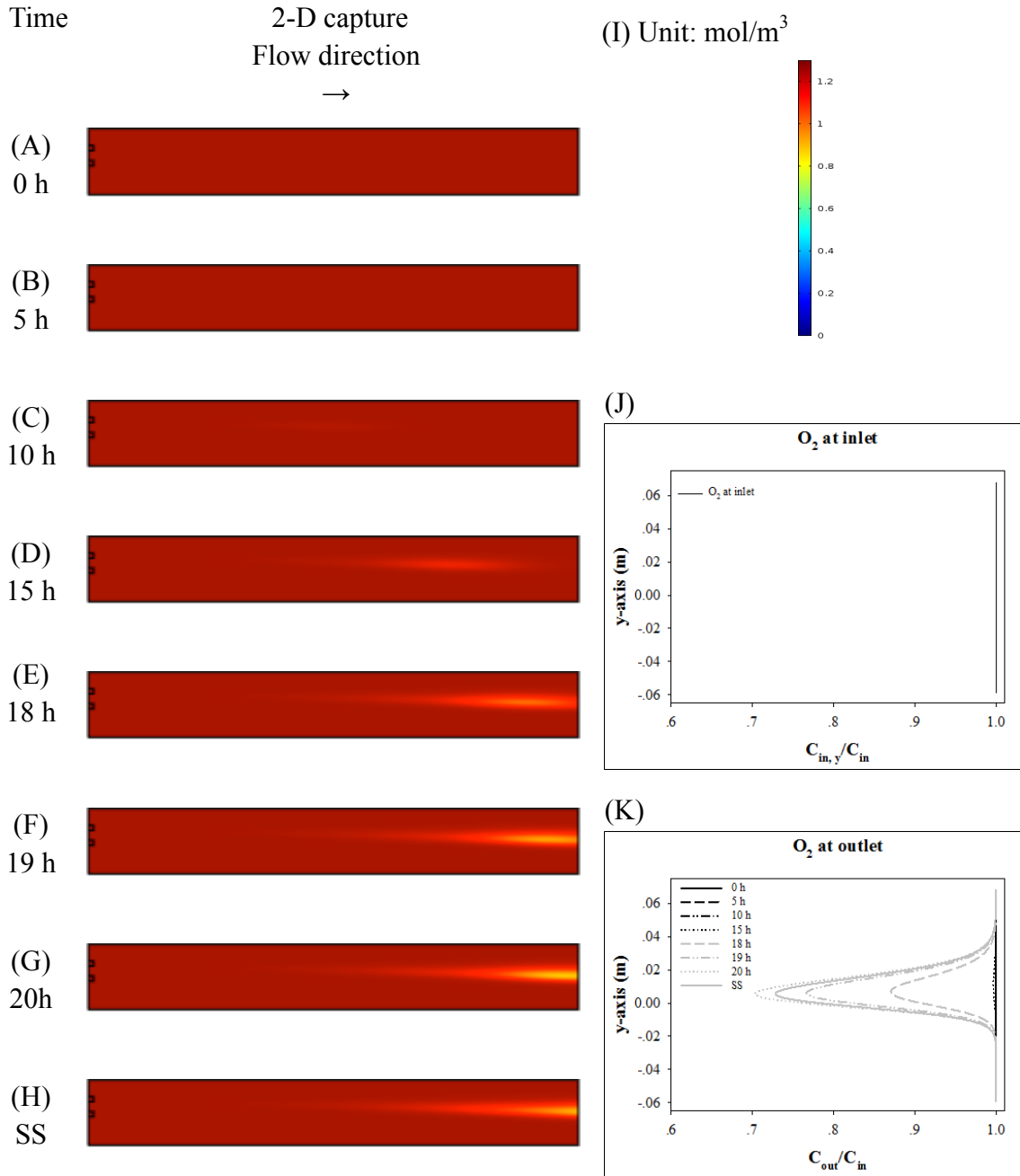


Figure 3.3.3 COMSOL simulation results with bacterial cell growth/death and chemotaxis terms applied: distribution of **oxygen** within the microcosm as a function of time. (A) 0 h; (B) 5 h; (C) 10 h; (D) 15 h; (E) 18 h; (F) 19 h; (G) 20 h after injection; (H) steady state; (I) scale bar for (A)-(H); (J) oxygen concentration profile at inlet. (K) oxygen concentration profile at outlet of the microcosm as a function of time.

3.4. Comparison: cell growth/death vs. chemotaxis

During the 2-D microcosm runs, after bacterial cells and toluene met each other, both bacterial growth process and chemotaxis would lead to increased toluene consumption thus improved bioremediation efficiency. To respectively investigate the effect of each of these processes, simulation was done in four combinatorial sets: both growth/death incorporated in the mathematical model (Equation 3.2.1 – 3.2.3); chemotaxis was not incorporated (Equation 3.2.8 – 3.2.10); growth/death was not incorporated (Equation 3.2.11-13); none of growth/death or chemotaxis was incorporated (Equation 3.2.14 – 3.2.16). The visual results of distribution of toluene, bacterial cells, and oxygen within the 2-D microcosm at 19 h were shown in **Figure 3.4.1**, and the concentration profiles of each species at the outlet for each of four sets were plotted in **Figure 3.4.2**.

In **Figure 3.4.1** (A1), the same as presented in chapter 3.3, decreased amount of toluene distribution in the region close to the 2-D microcosm outlet (top half-section) was observed where both chemotaxis and bacterial cell growth/death were applied. When chemotaxis was not applied (**Figure 3.4.1** (A3)), toluene distribution didn't show much difference from **Figure 3.4.1** (A1), indication insignificance of chemotaxis process. However, when bacterial cell growth/death was not applied (**Figure 3.4.1** (A2) and (A4)), higher concentration of toluene was observed in the region close to the outlet. This indicated that the low concentration of the toluene in the region close to the 2-D microcosm outlet was primarily due to cell growth/death terms that were incorporated in the mathematical model rather than the chemotaxis terms.

Similarly, the analysis of bacterial cell distribution in four sets of experiments (**Figure 3.4.1** (B1) - (B4)) confirmed the same results from the analysis of toluene above. The significantly increased bacterial cell concentration in the region close to the 2-D

microcosm outlet were mainly due to the bacterial cell growth/death terms in the mathematical model, and the chemotaxis term barely generated observable difference.

During 2-D microcosm runs, oxygen was solely consumed by bacterial cells, so the distribution of oxygen was similar to that of bacterial cell, however, in inverse fashion (**Figure 3.4.1** (C1) – (C4)). Again, the decreased oxygen distribution in the region close to the 2-D microcosm outlet aroused primarily from the bacterial growth/death terms.

The concentration profile of each species at the 2-D microcosm outlet for the four combinatorial sets of simulations confirmed the conclusion from above visual observation. In **Figure 3.4.2** (A), the higher two toluene peaks were for the computation where bacterial growth/death was not applied whereas the lower two peaks were for that where bacterial growth/death was applied. However, the peaks basically overlapped to each other when chemotaxis was applied and was not applied (**Figure 3.4.2** (A) thick grey line vs. black dash line, black dot line vs. thin grey line). Lower toluene peaks were due to the consumption by more bacterial cells in that region (**Figure 3.4.2** (B)). When bacterial cell growth/death was not applied, oxygen concentration remained at the same concentration value because it was not consumed by bacterial cells (**Figure 3.4.2** (C)), and when bacterial cell growth/death was applied, a decrease in oxygen concentration was observed where bacterial cell peaks were present. Moreover, whether the chemotaxis was applied or not did not lead to observable difference in the oxygen concentration profile at the 2-D microcosm outlet.

In summary, the simulation with four combinatorial sets where chemotaxis and bacterial growth/death terms were or were not applied suggest that, the latter played a greater role in the fate of toluene, bacterial cell and oxygen, and the incorporation of bacterial

growth/death terms significantly increase the number of bacterial cells within the microcosm leading to the significant decrease in toluene recovery from the 2-D microcosm outlet.

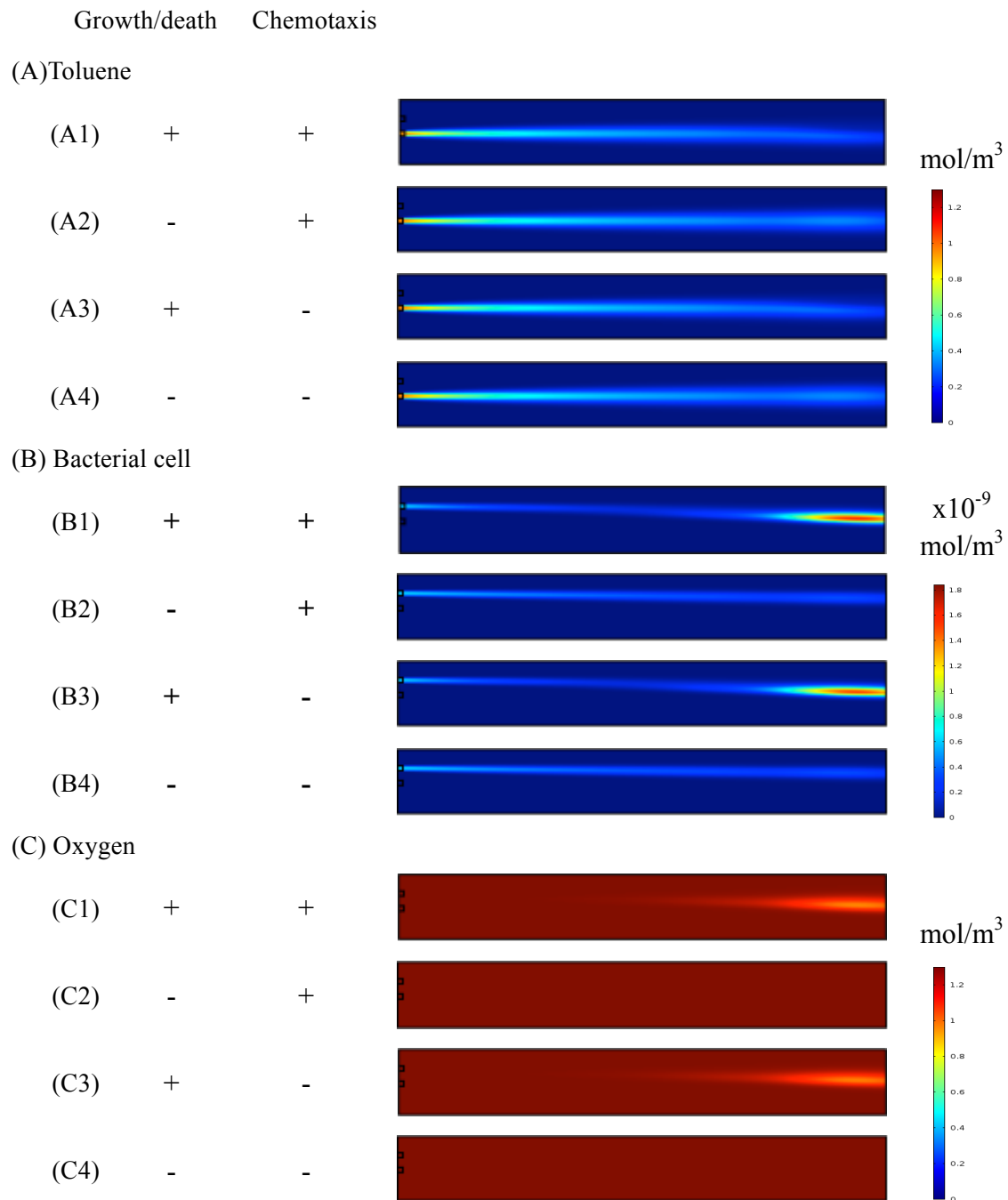
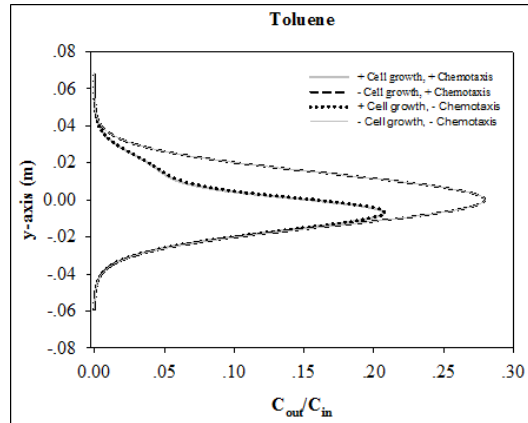
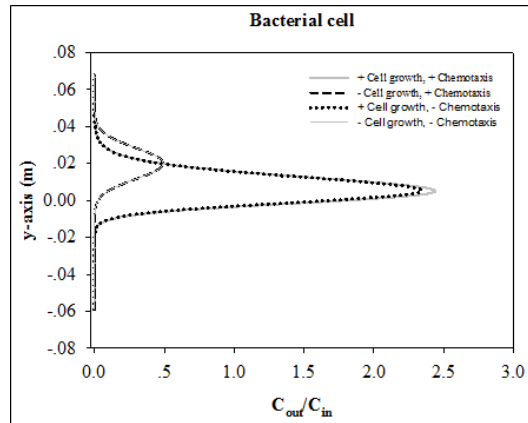


Figure 3.4.1 Simulation results: effect of bacterial cell growth/death and chemotaxis on the distribution of toluene, bacterial cells, and oxygen distribution. Images were captured 19 h after injection. (A) Toluene distribution within 2-D microcosm: (A1) with growth/death and chemotaxis, (A2) with chemotaxis only, (A3) with growth/death only, (A4) without growth/death and chemotaxis; (B) Bacterial cell distribution within 2-D microcosm: (B1) with growth/death and chemotaxis, (B2) with chemotaxis only, (B3) with growth/death only, (B4) without growth/death and chemotaxis; (C) Oxygen distribution within 2-D microcosm: (C1) with growth/death and chemotaxis, (C2) with chemotaxis only, (C3) with growth/death only, (C4) without growth/death and chemotaxis.

(A) Toluene



(B) Bacterial cell



(C) Oxygen (O₂)

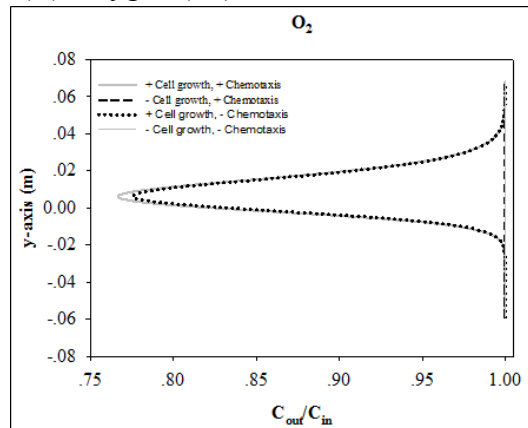


Figure 3.4.2 Simulation results: effect of bacterial cell growth/death and chemotaxis on the distribution of toluene, bacterial cells, and oxygen distribution at the outlet of 2-D microcosm. Each concentration profile was captured at 19 h after injection. (A) Toluene; (B) Bacterial cell; (C) Oxygen. (thick grey line: with growth/death and chemotaxis; black dash line: with chemotaxis only; black dot line: with cell growth only; thin grey line: without growth/death and chemotaxis)

3.5. Parametric study

Chapter 3.4 closed with the conclusion that bacterial growth/death had greater effect on toluene consumption during microcosm runs than chemotaxis, by comparing the conditions where each of the above two terms was entirely taken out from the mathematical model. In this chapter, in order to quantitatively test how the parameters concerning these two processes affect the overall remediation efficiency, simulation work by varying these parameter values over a range were conducted, and how the fate of each species got affected was studied. The parameters to vary during the simulations were: chemotaxis sensitivity coefficient $\chi_{0,eff}$ and chemotactic receptor binding constant K_c for chemotaxis process; maximum growth rate μ_{max} and half saturation constant K_a for cell growth/death process. Each of the abovementioned parameters were varied over its reference values that were set in chapter 3.3 by a factor ranging from 0.1x to 10x. First, COMSOL computations were done in “time dependent” mode to represent current experimental setup. The concentration of bacterial cells and toluene at the 2-D microcosm outlet were plotted, and the area under the peaks was summed up to quantify them. Bacterial cell and toluene recovery were calculated by dividing the overall bacterial cell or toluene harvested at the outlet by the amount injected at the inlet ($\frac{\sum C_{out}}{C_{in}}$). The same sets of computations were also performed with “stationary mode” which was a closer mimic of natural groundwater system where the steady state would probably have evolved over the long course of time after the release of the contaminant to the site. Moment analysis was then performed for the bacterial cell distribution at the 2-D microcosm outlet to further investigate how each parameter influenced the fate of bacterial cells and ultimately the toluene cleanup and bioremediation efficiency.

3.5.1 Sensitivity analysis of simulation results with current experimental setup

Figure 3.5.1.1 shows a tornado chart where the sensitivity of bacterial cell recovery (A) and toluene recovery (B) to each of bacterial cell growth/death related parameters and chemotaxis related parameters was respectively drawn. Each parameter value was varied over the range from -50% to 200% of its reference value (which matched to current experimental setup in chapter 3.3). It was apparently shown that the both bacterial cell recovery and toluene recovery showed greater sensitivity to bacterial growth related parameters μ_{max} and K_a than chemotaxis related parameters $\chi_{0,eff}$ and K_c . μ_{max} and $\chi_{0,eff}$ were positively correlated with bacterial cell recovery while K_a and K_c were negatively correlated. Since higher bacterial recovery indicates more consumption of toluene, μ_{max} and $\chi_{0,eff}$ were negatively correlated with toluene recovery while K_a and K_c were positively correlated. This justified the use of bacterial cell recovery as the indicator of bioremediation efficiency during 2-D microcosm experiments in chapter 2.

The four parameters were further varied over a larger range from 0.1x to 10x (except for μ_{max}), and the corresponding bacterial cell recovery and toluene recovery were calculated and listed in **Table 3.5.1.1**. Recovery data for 5x and 10x of reference value of μ_{max} were not available because COMSOL failed to converge using these parameter values, probably because the rapid increase in bacterial cell numbers or decrease in toluene/oxygen concentration ran out of the tolerable range of COMSOL. μ_{max} represents the growth rate of bacterial cells, so with 0.1x of reference value of μ_{max} , bacterial cell recovery decreased to 14.9%, and with 2x of reference value of μ_{max} , it increased up to 803%. K_a represents the affinity between toluene and bacterial cells in Monod equation characterizing bacterial cell growth upon the substrate (toluene in this case), and bacterial growth rate is inversely proportional to K_a (Equation 3.2.1). 0.1x reference value of K_a led to 791% of bacterial cell recovery and 10 x of reference value

of K_a led to 19.5% of bacterial cell recovery. These were in consistent with the fact that, regardless of the mass transfer barrier, increasing μ_{max} and decreasing K_a led to faster cell growth cultured as in homogeneous liquid media while decreasing μ_{max} and increasing K_a led to slower growth.

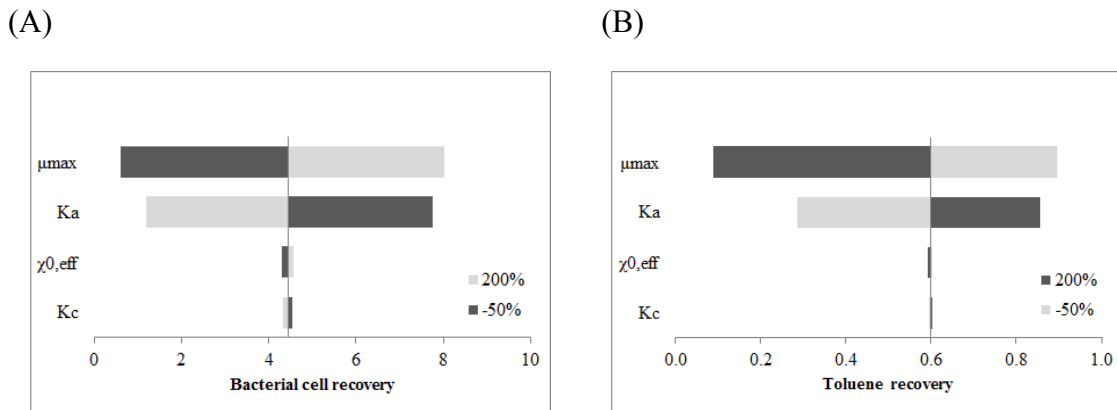


Figure 3.5.1.1 Tornado chart for sensitivity analysis of bacterial cell recovery and toluene recovery to growth and chemotaxis parameters, with 19-h sample.

Table 3.5.1.1 Parametric study with bacterial cell recovery and toluene recovery, with 19-h sample.

Bacterial cell recovery (x100%), 19-h sample					Toluene recovery (x100%), 19-h sample				
Fold #	μ_{max}	K_a	$\chi_{0,eff}$	K_c	Fold #	μ_{max}	K_a	$\chi_{0,eff}$	K_c
0.1x	0.149	7.91	4.28	4.74	0.1x	0.885	0.108	0.606	0.586
0.5x	0.608	7.76	4.31	4.53	0.5x	0.895	0.287	0.603	0.595
1x	4.45	4.45	4.45	4.45	1x	0.600	0.600	0.600	0.600
2x	8.03*	1.20	4.57	4.32	2x	0.088*	0.857	0.592	0.602
5x	N/A	0.318	4.57	4.30	5x	N/A	0.932	0.569	0.605
10x	N/A	0.195	5.47	4.29	10x	N/A	0.944	0.532	0.606

*recovery for 1.2x of reference value of μ_{max}

In natural groundwater system, once the contaminant was released, the plume develops over time and the steady state would have reached over a long time. To mimic this condition, the mathematical models were solved additionally in “steady state” mode and sensitivity analysis was performed in the same way as done in “time-dependent” mode above. **Figure 3.5.1.2** showed the Tornado chart where parameters were varied over the range from -50% to 200%, and **Table 3.5.1.2** showed the sensitivity of bacterial cell recovery and toluene recovery over a larger range from 0.1x to 10x of reference value of each parameter. Similar to what was observed in “time-dependent” mode, they showed greater sensitivity to growth related parameters μ_{max} and K_a , and the correlation trend with four parameters were the same as well.

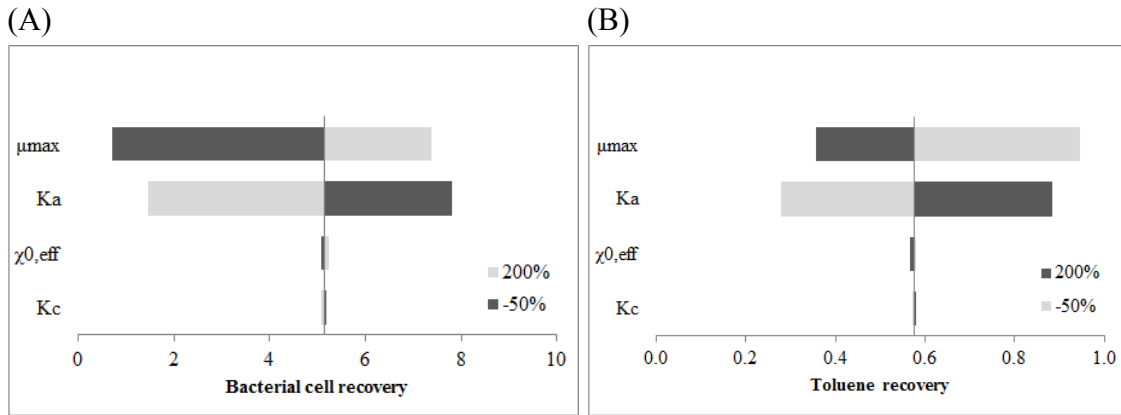


Figure 3.5.1.2 Tornado chart for sensitivity analysis of bacterial cell recovery and toluene recovery to growth and chemotaxis parameters at steady state. (note: recovery values at 120% of μ_{max} instead of those at 200% were plotted)

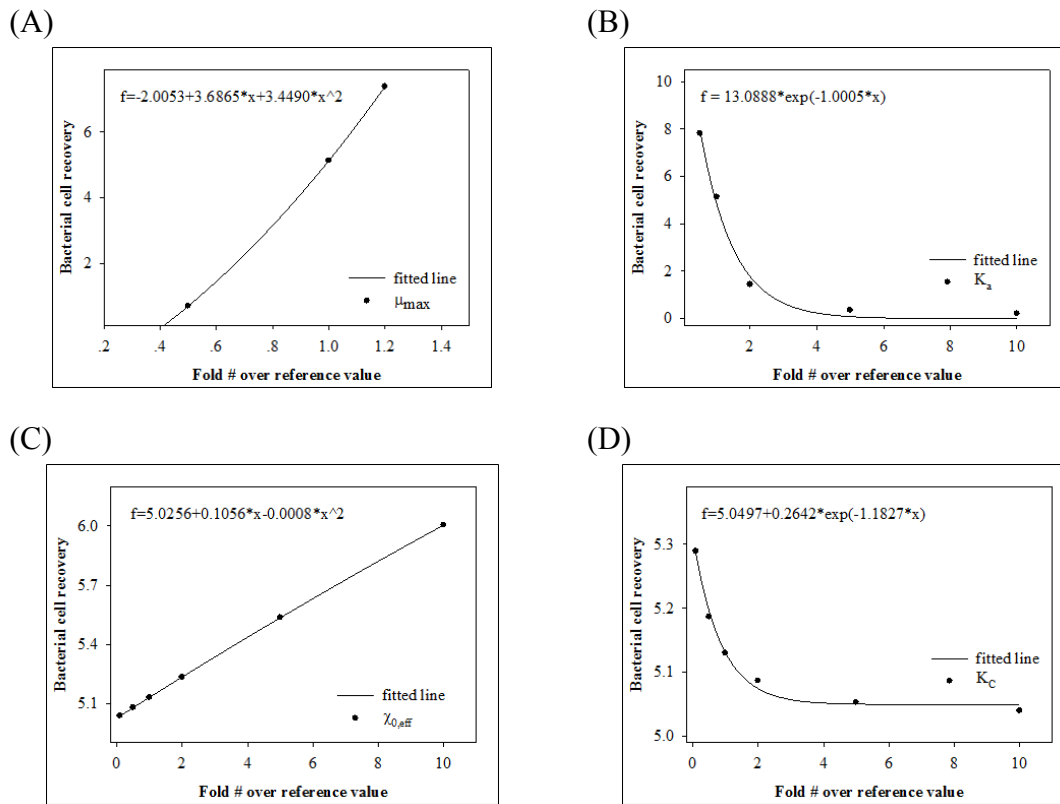
Table 3.5.1.2 Parametric study with bacterial cell recovery and toluene recovery, at steady state.

Bacterial cell recovery (x100%), steady state					Toluene recovery (x100%), steady state				
Fold #	μ_{max}	K_a	$\chi_{0,eff}$	K_c	Fold #	μ_{max}	K_a	$\chi_{0,eff}$	K_c
0.1x	0.169	N/A	5.04	5.29	0.1x	0.995	N/A	0.584	0.560
0.5x	0.700	7.81	5.08	5.19	0.5x	0.945	0.278	0.580	0.571
1x	5.13	5.13	5.13	5.13	1x	5.13	5.13	5.13	5.13
2x	7.38*	1.44	5.23	5.09	2x	0.358*	0.884	0.567	0.580
5x	N/A	0.354	5.54	5.05	5x	N/A	0.978	0.541	0.583
10x	N/A	0.209	6.01	5.04	10x	N/A	0.991	0.499	0.583

*recovery for 1.2x of reference value of μ_{max}

To calculate the sensitivity, bacterial cell recovery were plotted over each of the varied parameters, and the curves were fitted with equations of either polynomial or exponential decay functions whichever gave the least sum of squares (**Figure 3.5.1.3, Appendix A10**). The sensitivity was defined by the slope of the tangential line of the fitted curve (the reference point “Fold # = 1” indicates the parameter values used in current experimental setup), which were listed in **Figure 3.5.1.3 (E)**. The bacterial cell recovery was more sensitive to bacterial cell growth (10.6 for μ_{max} and -4.82 for K_a) and less to chemotaxis (0.104 for $\chi_{0,eff}$ and -0.0958 for K_c). Positive sign indicated positive correlation and negative sign indicated negative correlation.

The sensitivity value also showed a change at difference Fold #. For μ_{max} , there was no big change within the range of 0.5x and 1.2x, and similarly, it was almost linear relationship for $\chi_{0,eff}$. For K_a and K_c , the slope was very steep in the range of 0.1x ~ 2x, then showed almost no change when it increased for up to 10x. It inferred that increasing the affinity of toluene could be desirable to increase the bioremediation efficiency, either by increasing the affinity with toluene uptake receptors or that with chemotactic receptors on the surface of the bacterial cell.



(E)

Slope of tangential line / Sensitivity				
Fold #	μ_{max}	K_a	$\chi_{0,eff}$	K_c
0.1x	4.38E+00	N/A	1.05E-01	-2.78E-01
0.5x	7.14E+00	-7.94E+00	1.05E-01	-1.73E-01
1x	1.06E+01	-4.82E+00	1.04E-01	-9.58E-02
2x	1.20E+01	-1.77E+00	1.02E-01	-2.93E-02
5x	N/A	-8.80E-02	9.76E-02	-8.45E-04
10x	N/A	-5.92E-04	8.96E-02	-2.28E-06

*data for 1.2x of reference value of μ_{max}

Figure 3.5.1.3 Fitted curves for sensitivity calculation (reference point: $x=1$). The table below listed the calculated sensitivity for growth and chemotaxis parameters.

3.5.2 Moment analysis of simulation results with current experimental setup

To investigate how each above-mentioned parameter influenced the behavior of bacterial cells when they were transported within the 2-D microcosm, the bacterial cell concentration was plotted along y-axis at 2-D microcosm outlet at each value of the respective parameter, as drawn in **Figure 3.5.2.1**. The first, second, and third moment of the peaks were calculated (**Appendix A4**), which respectively represents the center of mass, the spread, and the skewness of the bacterial cell peaks. These three moments were affected by each of the parameters in different fashion and the eventual appearance of the peaks would result from comprehensive function of them. Note that toluene was injected from the inlet located at $y = 0$. So toluene concentration was highest at $y = 0$ and gradually decreased in both $\pm y$ directions. Bacterial cells were injected from the inlet located at $y = 0.03$ m.

After a certain time after injection, the bacterial cells got exposure to toluene, and subsequently sensed the toluene gradient and swam toward higher concentration of toluene via chemotaxis mechanism. This would lead to the downward movement (movement toward $y = 0$) of the center of mass of bacterial cells (first moment), and the greater the chemotaxis (increasing $\chi_{0,eff}$ and decreasing K_c), the higher degree of downward setting. As the bacterial cells closer to the center of toluene plume would experience higher toluene gradient (**Figure 3.3.1**), they would move faster than the bacterial cells distant to the center of the toluene plume, as a result, this would lead to a positively skewed bacterial cell distribution peak (third moment), and subsequently, broader peaks (second moment).

The influence of μ_{max} and K_a are more complicated. After the bacterial cells got exposure to toluene, they would start to grow. The original bacterial cell distribution was

a symmetric peak centered at $y = 0.03$ m. However, the bacterial cells below this line would get exposed to more toluene and grew faster than those cells located above this line. This faster growth of the bacterial cells at the bottom would always lead to the downward movement of the center of mass of bacterial cells, while the final peak would appear as a sum of residual bacterial cells (less closer to $y = 0$) and newly generated bacterial cells (more closer to $y = 0$). The growth would also contribute to broaden and to positively skew the peak as it would pull up the tail of the originally symmetric bacterial cell peak. However, the growth of bacterial cells upon exposure to toluene would increase the peak height and this would result in a narrowed, as well as less skewed peak. In a word, the final shape of the bacterial peaks would result from the comprehensive interaction of the four parameters, in particular, would depend on which one would exert a dominant effect.

In regard to the effect of $\chi_{0,eff}$ (**Figure 3.5.2.1 (C) and (E)**), with its increase, the center of mass of bacterial peak moved downward (toward $y = 0$ direction where toluene concentration was highest) a little bit but was negligible. However, as this lead to exposure to more toluene, a slight increase in bacterial cell number (peak area) could be observed. Additionally, a slightly increasing broadness of the peak as well as slightly increasing positive skewness was observed. These were inconsistency with above analysis. In regard to the effect of K_c (**Figure 3.5.2.1 (D) and (E)**), as chemotaxis got weakened with its increase, the trend was the opposite of that of $\chi_{0,eff}$.

In regard to the effect of μ_{max} (**Figure 3.5.2.1 (A) and (E)**), with its value increased up to 1x, the center of mass moved downward a bit. The width of the peak decreased more and more up to 1x of μ_{max} but suddenly increased at 1.2x. This was due to the faster growth of the bacterial cells upon exposure to higher concentration of toluene closer to $y = 0$.

The same trend was observed for the skewness of the peak for the same reason, except that the turning point occurred at 0.5x of its reference value. The effect of K_a (**Figure 3.5.2.1 (C) and (E)**) was opposite of that of μ_{max} . A constantly downward movement of center of mass was observed, and similar to what was observed for μ_{max} effect, complicated responses in broadness as well as skewness of the peak were observed, due to the interplay of the different processes. Besides, a more drastic change in bacterial cell number (peak area) due to bacterial cell growth/death related parameters in comparison to chemotaxis related parameters could be observed.

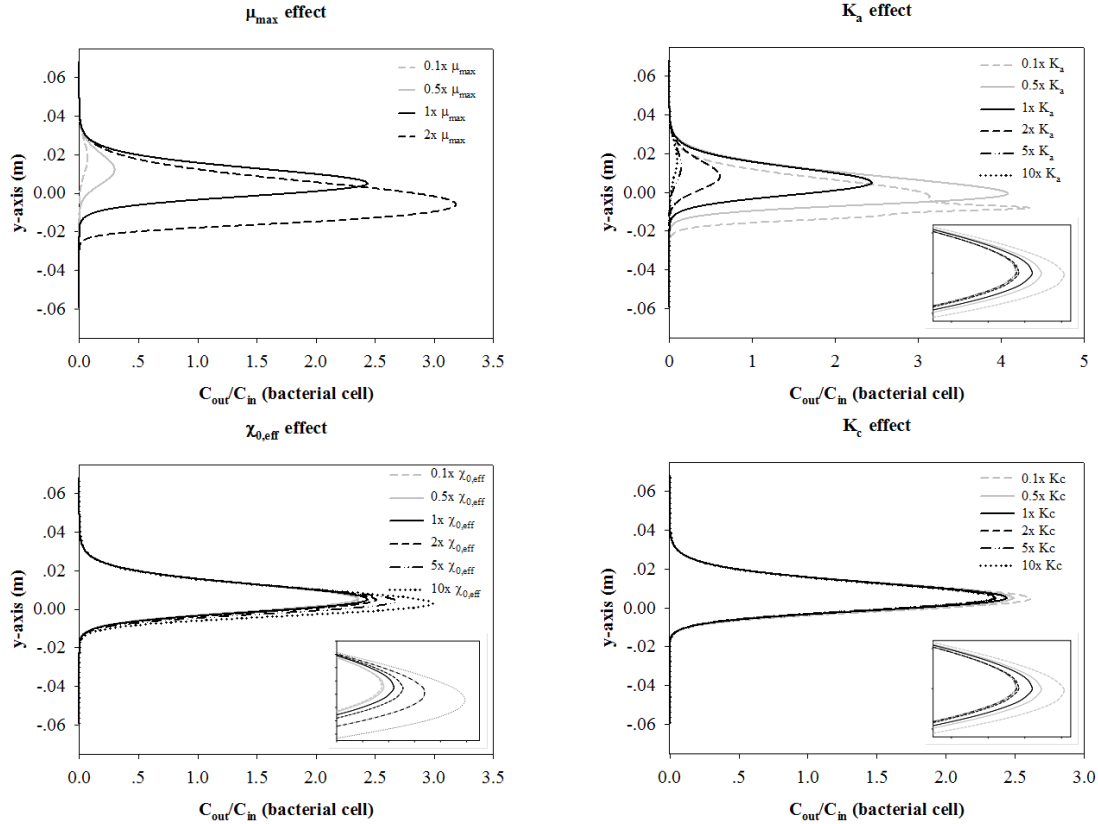


Figure 3.5.2.1 Concentration profiles of bacterial cells at the outlet at various parameter values.

Table 3.5.2.1 Moment analysis. \bar{y} was listed in reference to the injection position.

Moment analysis (Bacterial cell)										
		m1	m2	m3			m1	m2	m3	
Fold #		\hat{y} (cm)	σ^2 (cm ²)	γ	Fold #		\hat{y} (cm)	σ^2 (cm ²)	γ	
Growth/death	μ_{max}	0.1x	-2.98	0.697	2.42E-08	K_a	0.1x	-3.00 ^{&}	0.779 ^{&}	4.50E-07 ^{&}
		0.5x	-2.99	0.680	1.34E-07		0.5x	-3.00	0.657	3.30E-07
		1x	-2.99	0.578	1.88E-07		1x	-2.99	0.578	1.88E-07
		2x	-3.00*	0.979*	5.38E-07*		2x	-2.99	0.670	2.13E-07
		5x	N/A	N/A	N/A		5x	-2.98	0.773	1.24E-07
		10x	N/A	N/A	N/A		10x	-2.98	0.773	1.24E-07
Chemotaxis	$\chi_{0,eff}$	0.1x	-2.99	0.578	1.88E-07	K_c	0.1x	-2.99	0.574	1.93E-07
		0.5x	-2.99	0.578	1.87E-07		0.5x	-2.99	0.577	1.91E-07
		1x	-2.99	0.578	1.88E-07		1x	-2.99	0.578	1.88E-07
		2x	-2.99	0.578	1.93E-07		2x	-2.99	0.578	1.87E-07
		5x	-2.99	0.579	2.09E-07		5x	-2.99	0.578	1.85E-07
		10x	-2.99	0.579	2.09E-07		10x	-2.99	0.578	1.85E-07

*recovery for 1.2x of reference value of μ_{max}

[&]recovery for 0.2x of reference value of K_a

3.6 Effect of oxygen supply

For bioremediation with aerobic bacteria, it has been well studied that limited oxygen supply significantly impedes the bioremediation process (53, 54). To elucidate the role of oxygen in current 2-D microcosm experiments, mathematical models incorporating and not incorporating oxygen consumption terms were set up, as shown in **Equation 3.2.17 – 3.2.18**. Simulation was done in “steady state” mode, and the visual 2-D results as well as the plots of toluene, bacterial cells, and oxygen at the outlet of 2-D microcosm were also shown (**Figure 3.6.1** and **3.6.2**). By observation, there was no apparent difference in toluene and bacterial cell distribution when oxygen consumption were or were not applied (**Figure 3.6.1** (A) and (B) vs. **Figure 3.6.2** (A) and (B), **Figure 3.6.1** (F) vs. **Figure 3.6.2** (F)), while decreased oxygen concentration in the region close to the outlet were observed in **Figure 3.6.1** (C) which was not the case when oxygen was not being consumed in **Figure 3.6.2** (C). Plotting the toluene and bacterial cell concentration profile together in **Figure 3.6.3**, it can be seen that incorporation of oxygen into the model didn't have any effect on the pattern, demonstrating that oxygen was not limiting the growth of the bacterial cells or the consumption of the toluene by the bacterial cells.

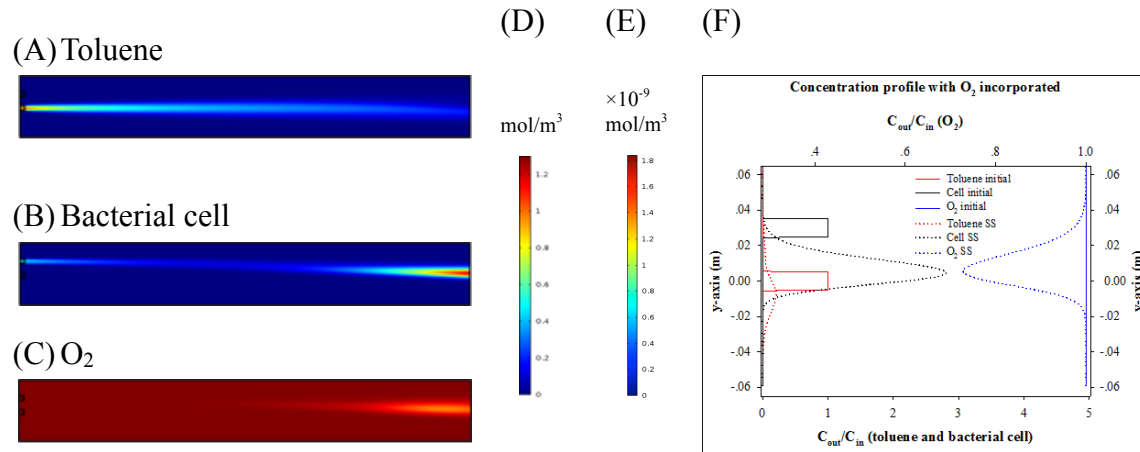


Figure 3.6.1 With O_2 incorporated in the model. Distribution of toluene (A), bacterial cell (B), and oxygen (C) within the 2-D microcosm at steady state. (D) is the scale bar for (A) and (C), and (E) is the scale bar for (B). Concentration profile of toluene, bacterial cell, and oxygen at the outlet were plotted over y-axis in (F).

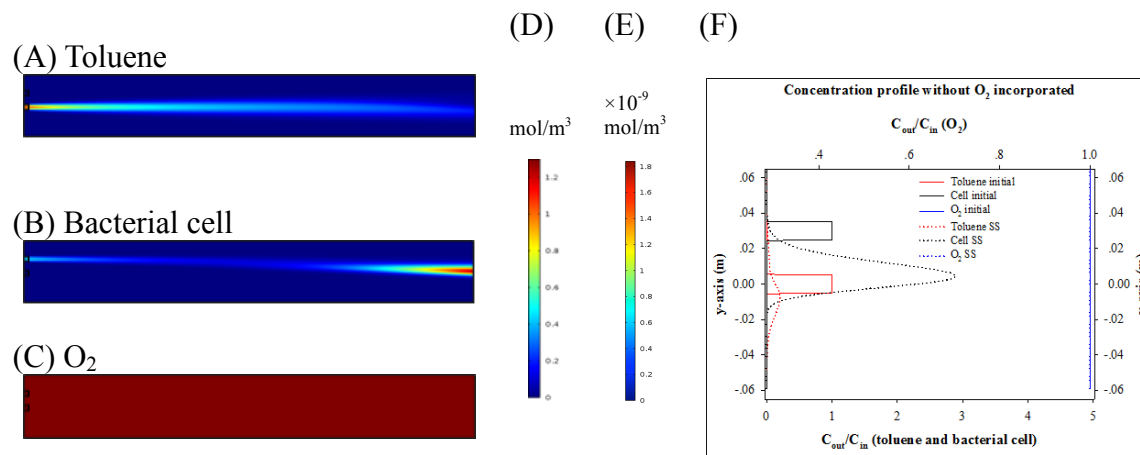


Figure 3.6.2 Without O_2 incorporated in the model. Distribution of toluene (A), bacterial cell (B), and oxygen (C) within the 2-D microcosm at steady state. (D) is the scale bar for (A) and (C), and (E) is the scale bar for (B). Concentration profile of toluene, bacterial cell, and oxygen at the outlet were plotted over y-axis in (F).

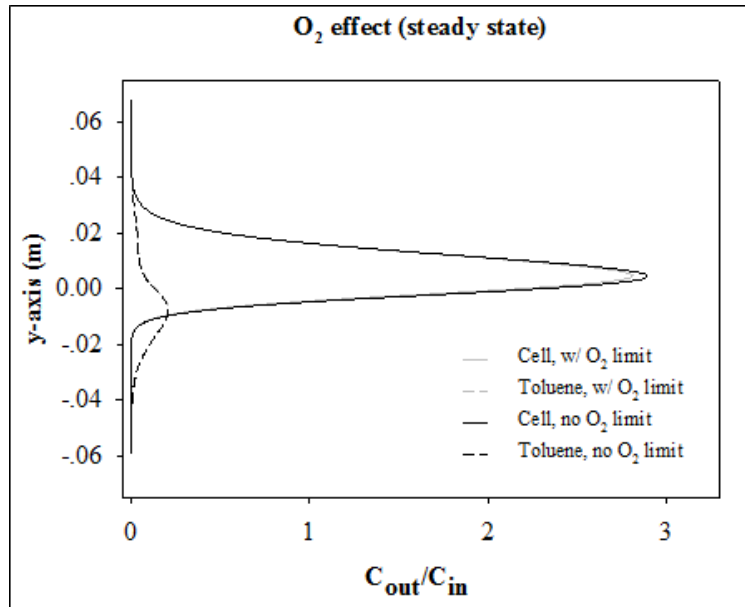


Figure 3.6.3 Comparison of toluene and bacterial cell recovery when oxygen was and wasn't incorporated in the mathematical model.

Next, simulations were done with varied oxygen concentrations, from 0.1x for up to 2.8x (56, 57) of the oxygen concentration used in current experimental setup. Bacterial cell as well as toluene recovery was plotted over the varied oxygen concentrations. It was clearly shown that at 0.1x of reference oxygen concentration, bacterial cell growth and toluene cleanup were significantly limited; at 0.5x of reference oxygen concentration, bacterial cell growth and toluene cleanup were moderately affected; from 1x to up to 2.8x of reference oxygen concentration, bacterial cell growth and toluene cleanup didn't change much. This again confirmed that, the oxygen supply was not limiting the bioremediation efficiency under current experimental setup, and toluene was the sole bacterial cell growth limiting as well as toluene cleanup limiting factor.

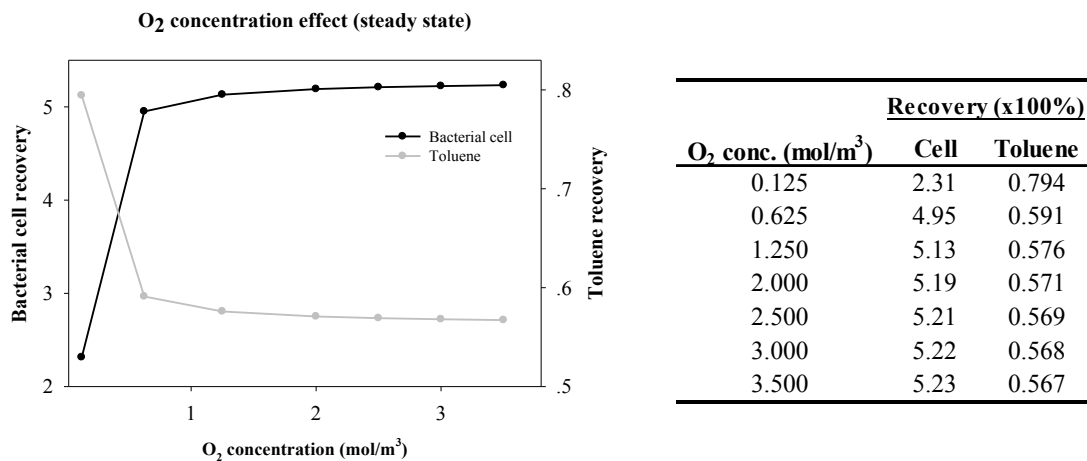


Figure 3.6.4 Effect of oxygen concentration on toluene and bacterial cell recovery.

3.7. Effect of spacing between bacterial cell and toluene

To study the behavior of bacterial cells more distant to the contaminated site than current experimental setting, the injection inlet for the bacterial cells were moved up 1 cm resulting in the distance of 4 cm between the bacterial cell and toluene injection inlet. COMOSL simulations were performed the same way as in Chapter 3.3, and the results were shown in **Figure 3.7.1** (3 cm spacing) and **3.7.2** (4 cm spacing). With increased spacing, no significant decrease (**Figure 3.7.1** (A) and (F)) in toluene concentration in the region close to 2-D microcosm outlet was observed as in the closer spacing in **Figure 3.7.2** (A) and (F). Consequently, no significant cell growth or decrease in oxygen concentration (**Figure 3.7.2** (B), (C) and (F)) in the region close to the outlet was observed as compared with in closer spacing (**Figure 3.7.1** (B), (C) and (F)).

Similar to the sensitivity analysis with 3 cm spacing, a tornado chart was drawn to study the sensitivity of bacterial cell as well as toluene recovery to the four parameters related with bacterial cell growth/death and chemotaxis (**Figure 3.7.3** and **Table 3.7.1**). The overall bacterial recovery was lower and toluene recovery was higher, at this distant region, due to less exposure of the bacterial cells to toluene throughout the 2-D microcosm runs. The sensitivity was still higher for bacterial cell growth/death process than the chemotaxis process. The quantitative analysis of the sensitivity also showed the same trend as in closer spacing (**Figure 3.7.4** and **Table 3.7.2**)

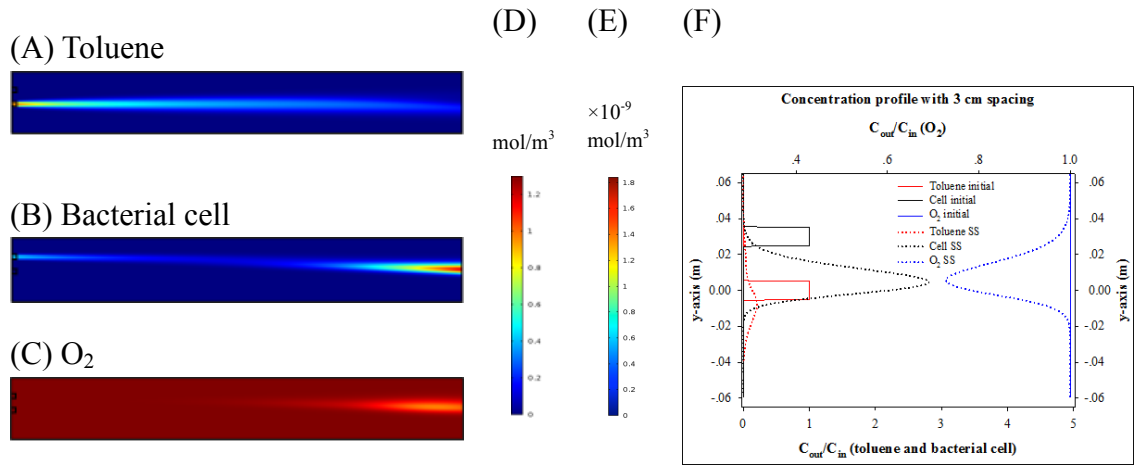


Figure 3.7.1 With 3 cm spacing between bacterial cell and toluene (experimental setup). Distribution of toluene (A), bacterial cell (B), and oxygen (C) within the 2-D microcosm at steady state. (D) is the scale bar for (A) and (C), and (E) is the scale bar for (B). Concentration profile of toluene, bacterial cell, and oxygen at the outlet were plotted over y-axis in (F).

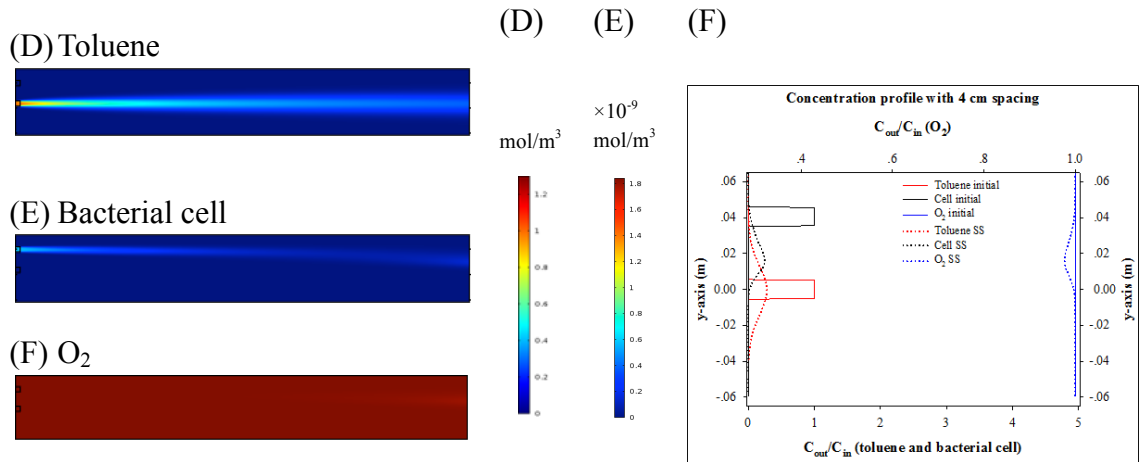
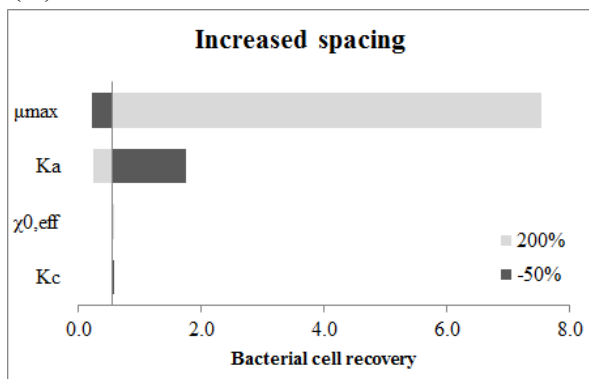


Figure 3.7.2 With 4 cm spacing between bacterial cell and toluene. Distribution of toluene (A), bacterial cell (B), and oxygen (C) within the 2-D microcosm at steady state. (D) is the scale bar for (A) and (C), and (E) is the scale bar for (B). Concentration profile of toluene, bacterial cell, and oxygen at the outlet were plotted over y-axis in (F).

(A) Bacterial cell



(B) Toluene

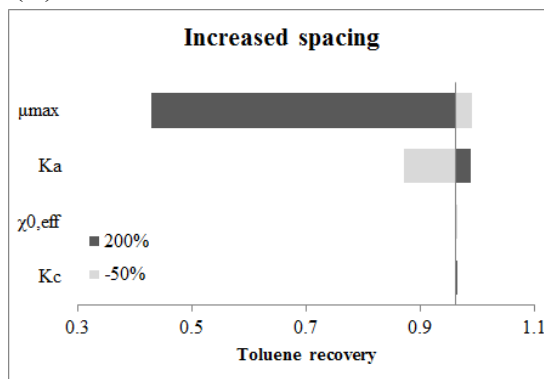


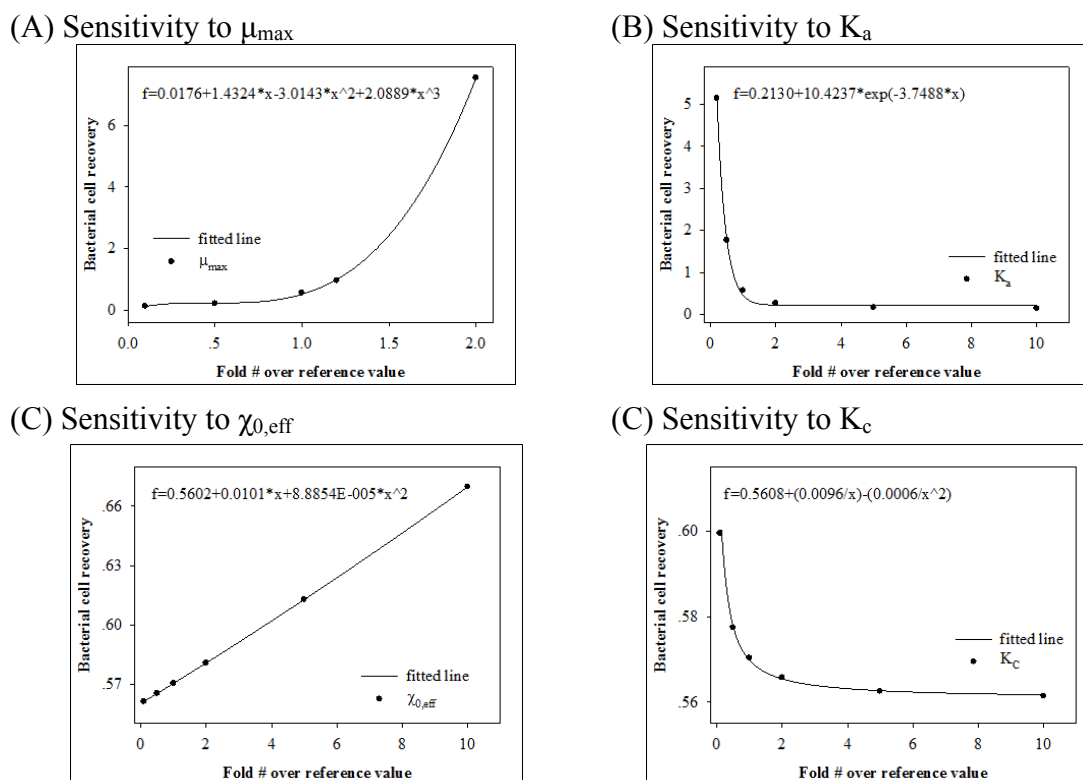
Figure 3.7.3 Tornado chart for sensitivity analysis of bacterial cell recovery (A) and toluene recovery (B) to growth and chemotaxis parameters at steady state, with increased spacing between bacterial cells and toluene.

Table 3.7.1 Parametric study with bacterial cell recovery and toluene recovery, with increased spacing between bacterial cells and toluene.

Bacterial cell recovery (x100%), steady state					Toluene recovery (x100%), steady state				
Fold#	μ_{\max}	K_a	$\chi_{0,\text{eff}}$	K_c	Fold#	μ_{\max}	K_a	$\chi_{0,\text{eff}}$	K_c
0.1x	0.138	5.148*	0.561	0.599	0.1x	0.999	0.600*	0.964	0.961
0.5x	0.222	1.766	0.565	0.577	0.5x	0.991	0.872	0.964	0.963
1x	0.570	0.570	0.570	0.570	1x	0.963	0.963	0.963	0.963
2x	7.538	0.262	0.581	0.566	2x	0.429	0.988	0.963	0.964
5x	N/A	0.165	0.613	0.563	5x	N/A	0.996	0.960	0.964
10x	N/A	0.143	0.670	0.561	10x	N/A	0.998	0.956	0.964

*recovery for 0.2x of reference value of K_a

*recovery for 0.2x of reference value of K_a



(E)

	<u>Slope/ Sensitivity (Fold # = 1)</u>	
	<u>3 cm spacing</u>	<u>4 cm spacing</u>
μ_{\max}	1.06E+01	1.67E+00
K_a	-4.82E+00	-9.20E-01
$\chi_{0,\text{eff}}$	1.04E-01	1.03E-02
K_c	-9.58E-02	-8.40E-03

Figure 3.7.4 Fitted curves for sensitivity calculation at the reference point ($x=1$) with simulation with increased spacing between bacterial cells and toluene. The table below listed the calculated sensitivity for growth and chemotaxis parameters with increased spacing between bacterial cells and toluene, as well as those from current experimental setup for comparison.

3.8. Effect of flow rate

In this chapter, the effect of groundwater flow rate on the bacterial behavior and toluene cleanup process was studied. As compared the flow rate used in the experimental setup 1.55×10^{-5} m/s, an elevated flow rate of 1.76×10^{-4} m/s was tested (45, 46). A comparison was shown in **Figure 3.8.1 and 3.8.2**. The decrease in toluene concentration, bacterial cell growth, and decrease in oxygen concentration in the region close to 2-D microcosm outlet were no longer observable at high flow rate. Though higher flow rate was beneficial in terms of promoting the transfer of species perpendicular to the flow rate by increasing the dispersion (where i is one of the species toluene, bacterial cell or oxygen, $D_{iy} = \alpha_{iy} \times V_f + \frac{D_{i,eff}}{\varepsilon}$), the increased flow rate dramatically decreased the residence time of the species by carrying them away even faster through the convective flow. As a result, the bacterial cells had decreased time period for them either to sense the toluene gradient to give chemotactic response or to uptake toluene to reproduce themselves. The calculated dispersion coefficient for toluene, bacterial cells, and oxygen were listed in **Table 3.8.1**.

Sensitivity analysis was performed the same way in chapter 3.5, and at higher flow rate, the bacterial cell growth/death related parameters still played a greater role than chemotaxis in terms of toluene cleanup rate and bioremediation efficiency. (**Figure 3.8.3, Figure 3.8.4, and Table 3.8.2**)

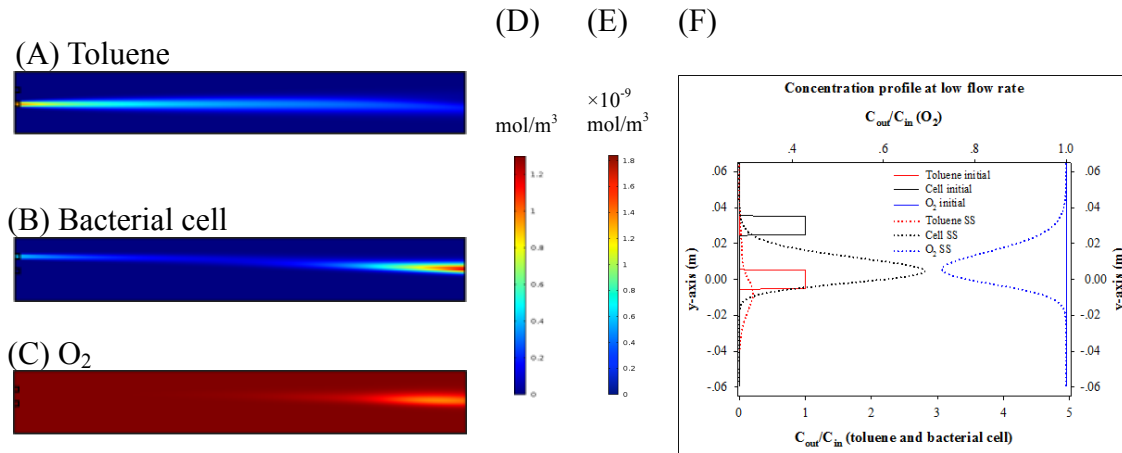


Figure 3.8.1 Simulation result at $V_f = 1.55 \text{ e-}5 \text{ m/s}$ (experimental setup). Distribution of toluene (A), bacterial cell (B), and oxygen (C) within the 2-D microcosm at steady state. (D) is the scale bar for (A) and (C), and (E) is the scale bar for (B). Concentration profile of toluene, bacterial cell, and oxygen at the outlet were plotted over y-axis in (F).

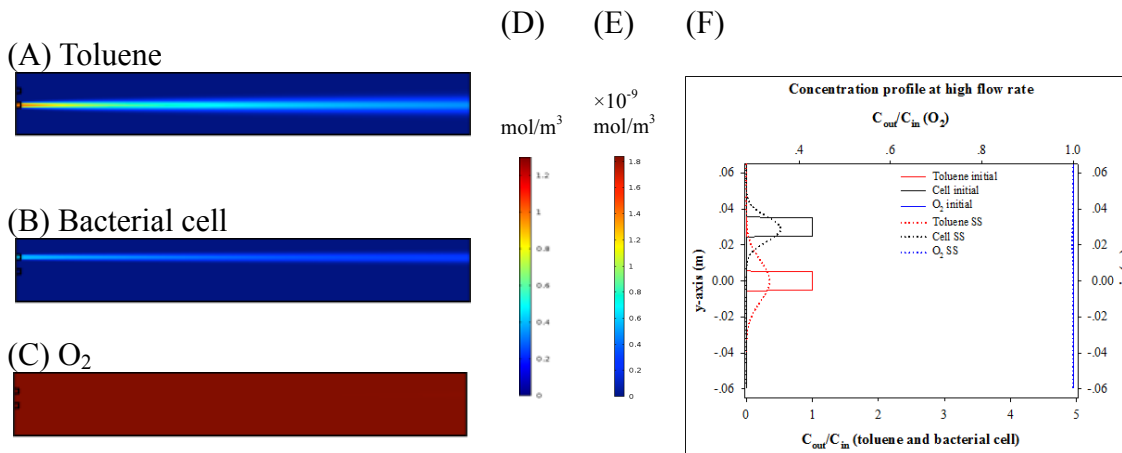


Figure 3.8.2 Simulation result at $V_f = 1.76 \text{ e-}4 \text{ m/s}$. Distribution of toluene (A), bacterial cell (B), and oxygen (C) within the 2-D microcosm at steady state. (D) is the scale bar for (A) and (C), and (E) is the scale bar for (B). Concentration profile of toluene, bacterial cell, and oxygen at the outlet were plotted over y-axis in (F).

Table 3.8.1 Dispersion coefficient of toluene, bacterial cell, and oxygen at low and high flow rate.

	$V_f = 1.55e-5 \text{ m/s}$	$V_{f,hi} = 1.76e-4 \text{ m/s}$
D_{ay}	3.36E-09	1.30E-08
D_{by}	1.15E-09	4.07E-09
D_{oy}	6.25E-09	1.59E-08

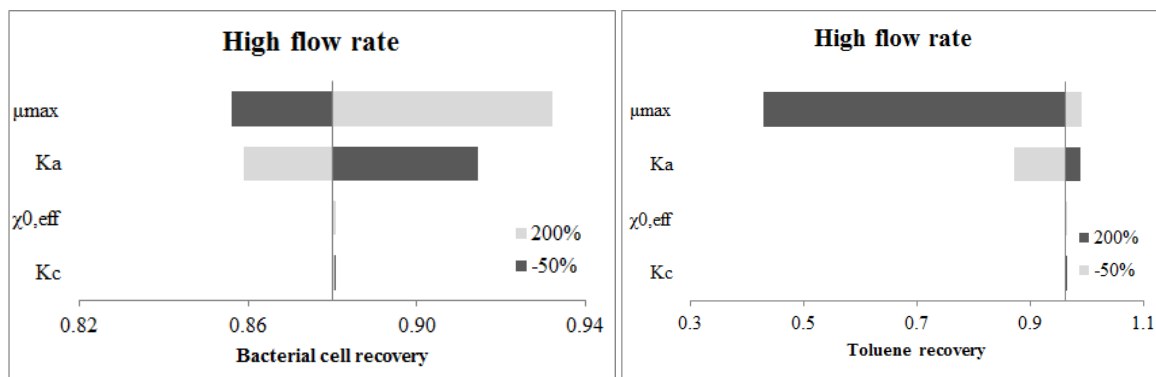
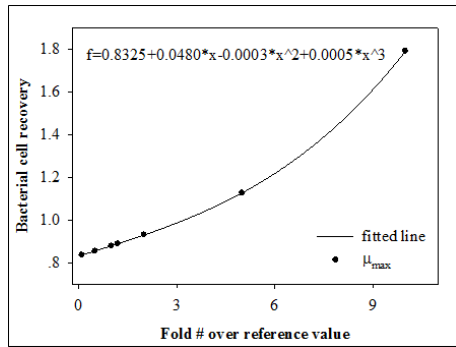
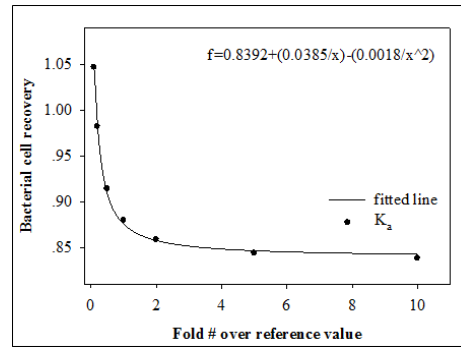
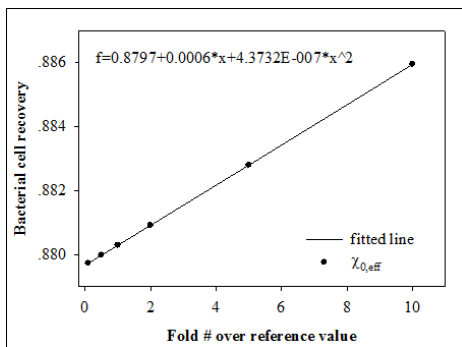
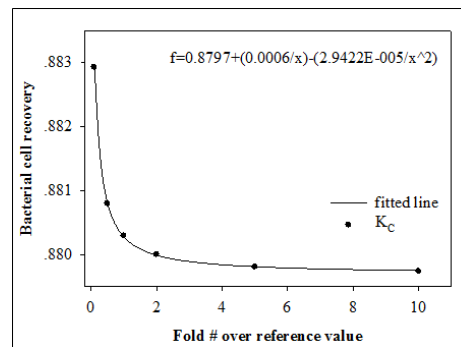


Figure 3.8.3 Tornado chart for sensitivity analysis of bacterial cell recovery and toluene to growth and chemotaxis parameters at steady state, with higher flow rate.

Table 3.8.2 Parametric study with bacterial cell recovery and toluene recovery, with higher flow rate.

Bacterial cell recovery (x100%), steady state					Toluene recovery (x100%), steady state				
Fold#	μ_{max}	K_a	$\chi_{0,eff}$	K_c	Fold#	μ_{max}	K_a	$\chi_{0,eff}$	K_c
0.1x	0.838	0.982*	0.880	0.883	0.1x	1.000	0.990*	0.997	0.997
0.5x	0.856	0.914	0.880	0.881	0.5x	0.999	0.995	0.997	0.997
1x	0.880	0.880	0.880	0.880	1x	0.997	0.997	0.997	0.997
2x	0.932	0.859	0.881	0.880	2x	0.981	0.999	0.997	0.997
5x	1.13	0.844	0.883	0.880	5x	0.939	1.000	0.997	0.997
10x	1.79	0.839	0.886	0.880	10x	0.939	1.000	0.997	0.997

*recovery for 1.2x of reference value of K_a *recovery for 0.2x of reference value of K_a

(A) Sensitivity to μ_{\max} (B) Sensitivity to K_a (C) Sensitivity to $\chi_{0,\text{eff}}$ (D) Sensitivity to K_c 

(E)

	Slope/ Sensitivity (Fold # = 1)	
	Low flow rate	High flow rate
μ_{\max}	1.06E+01	4.89E-02
K_a	-4.82E+00	-3.49E-02
$\chi_{0,\text{eff}}$	1.04E-01	6.01E-04
K_c	-9.58E-02	-5.41E-04

Figure 3.8.4 Fitted curves for sensitivity calculation at the reference point ($x=1$) with simulation with higher flow rate. The table below listed the calculated sensitivity for growth and chemotaxis parameters with higher flow rate, as well as those from current experimental setup for comparison.

Chapter 4. Conclusions and Recommendations

The transport of microorganisms through the saturated porous matrix of soil is critical to the successful implementation of bioremediation in polluted groundwater systems. Motile bacteria that are self-propelled are able to swim independently of the groundwater flow and thereby enhance their accessibility to the hydrocarbon pollutants which they chemically transform and use as carbon and energy sources. Access to the hydrocarbons, thus provides a competitive advantage and increases the growth rate of the motile bacterial population, which ultimately led to improved bioremediation efficiency. In this study, a 2-D rectangular-shaped microcosm packed with quartz sand was used to study the transport and population growth of bacteria within a saturated model aquifer system as well as the resulting toluene cleanup efficiency. A model system comprising *Pseudomonas putida* F1 (PpF1) strains and toluene, to which PpF1 is chemotactic to and with which PpF1 could utilize as their carbon and energy source for survival and growth, was employed. Species of *Pseudomonas putida* F1, either PpF1 wild type or PpF1 mutants (PpF1 (Δ to*dX*) or PpF1 (Δ to*dX* Δ cym*D* Δ F1*fadL*)) that lacked a mechanism to transport toluene across the outer cell membrane, were injected above or below the toluene. The ability to take up toluene into the cell resulted in significantly greater population growth of the PpF1 wild type as compared to the mutants. The established mathematical model also confirmed the sensitiveness of the toluene degradation efficiency to bacterial growth related parameters which was directly correlated with toluene uptake capability, regardless of the presence of mass transfer barrier. And this sensitiveness was reserved under different conditions such as in a region more distant to toluene source and with an increased flow rate. This suggests that, in addition to mechanisms that enhance the delivery of the degrading agents to the contaminated site, transport membrane proteins of bacteria can also play a key role in bioremediation enhancement. Moreover, it suggests the potential of engineering bacteria toward higher

contaminant permeability for enhanced bioremediation efficiencies. Overall, the results indicated that the coupling between transport of motile bacteria and population growth facilitated by uptake of toluene leads to a greater abundance of bacteria in the vicinity of the plume that will aid biodegradation in groundwater systems that are not naturally well-mixed. Furthermore, it suggested the potential to engineer toluene-degrading bacteria toward greater toluene permeability for enhanced bioremediation efficiency.

5. References

1. WG Rixey. "The long-term dissolution characteristics of a residually trapped BTX mixture in soil". *Hazardous Waste and Hazardous Materials*, Vol 13 (2), 2009.
2. VI Pye and J Kelley. "The extent of groundwater contamination in United States". National Academies Press, Jan 1, 1984.
3. United States Environmental Protection Agency, <https://www.epa.gov/ust>, 2017.
4. United States Environmental Protection Agency, Office of Underground Storage Tanks, Corrective Action Measures Archive, 2001.
5. P Panagos, MV Liedekerke, Y Yigini and L Montanarella. "Contaminated sites in Europe: Review of the current situation based on data collected through a European network". *Journal of Environmental and Public Health*, Vol 2013, 2013.
6. DH Chen. "Sustainable water technologies: Groundwater protection and remediation". CRC Press, Oct 14, 2016.
7. MG Snousy, MM Khalil, T Abdel-Moghny and El-Sayed E. "An overview on the organic contaminants". *SDRP Journal of Earth Sciences and Environmental Studies*, Vol 1, 2016.
8. National Research Council. "Alternatives for managing the nation's complex contaminated groundwater sites". National Academies Press, Mar 27, 2013.
9. United States Environmental Protection Agency. "Toxic and priority pollutants under the clean water act".
10. F Saga. "Evaluation of demonstrated and emerging technologies for the treatment of contaminated land and groundwater". *Applied Catalysis B: Environmental*, Vol 15 (3-4), 1998.
11. DM Mackay and JA Cherry. "Groundwater contamination: Pump-and-treat remediation". *Environmental Science & Technology*, Vol 23, 1989.
12. JE Vidonish, K Zygourakis, CA Masiello, G Sabadell and PJJ Alvarez. "Thermal

-
- treatment of hydrocarbon-impacted soils: A review of technology innovation for sustainable remediation”. *Engineering*, Vol 2 (4), 2016.
13. RZ Hoff. “Bioremediation: an overview of its development and use for oil spill cleanup”. *Marine Pollution Bulletin*, Vol 26 (9) 1993.
 14. JH Langwaldt and JA Puhakka. “On-site biological remediation of contaminated groundwater: a review”. *Environmental Pollution*, Vol 107 (2), 2000.
 15. M Farhadiana, C Vachelarda, D Ducheza and C Larrochea. “In situ bioremediation of monoaromatic pollutants in groundwater: A review”. *Bioresource Technology*, Vol 99 (13), 2008.
 16. J Chen, X Gao and LD Yan. “Recent progress in monoaromatic pollutants removal from groundwater through bioremediation”. *International Letters of Natural Sciences*, Vol 7, 2015.
 17. RK Jain, M Kapur, S Labana, PM Sarma, B LaI, D Bhattacharya and IS Thakur. “Microbial Diversity: Application on micro-organisms for the biodegradation of xenobiotics”. *Current Science*, Vol 89, 2005.
 18. R. Chandra. “Advances in biodegradation and bioremediation of industrial waste”. CRC Press, Mar 24, 2015.
 19. TH Christensen, P Kjeldsen, PL Bjerg, DL Jensen, JB Christensen, A Baun, HJ Albrechtse and G Heron. “Biogeochemistry of landfill leachate plumes”. *Applied Geochemistry*, Vol 16 (7-8), 2001.
 20. P Martian, KS Sorenson and LN Peterson. “A critique of the internal tracer method for estimating contaminant degradation rates”. *Ground Water*, Vol 41 (5), 2003.
 21. KU Mayer, SG Benner, EO Frind, SF Thornton and DN Lerner. “Reactive transport modeling of processes controlling the distribution and natural attenuation of phenolic compounds in a deep sandstone aquifer”. *Journal of Contaminant Hydrology*, Vol 53 (3-4), 2001.

-
22. ID Klenk and P Grathwohl. "Transverse vertical dispersion in groundwater and the capillary fringe". *Journal of Contaminant Hydrology*, Vol 58 (1-2), 2002.
 23. A Kumar, BS Bisht, VD Joshi and T Dhewa. "Review on Bioremediation of Polluted Environment: A Management Tool". *International Journal of Environmental Sciences*, Vol 1 (6), 2011.
 24. LW Perelo. "Review: In situ and bioremediation of organic pollutants in aquatic sediments". *Journal of Hazardous Materials*, Vol 177, 2010.
 25. SM Bamforth and I Singleton. "Bioremediation of polycyclic aromatic hydrocarbons: current knowledge and future directions". *Journal of Chemical Technology and Biotechnology*, Vol 80 (7), 2005.
 26. PJ Sturman, PS Stewart, AB Cunninghama, EJ Bouwera and JH Wolfram. "Engineering scale-up of in situ bioremediation processes: a review". *Journal of Contaminant Hydrology*, Vol 19 (3), 1995.
 27. RW Harvey and H Harms. "Tracers in Groundwater: Use of Microorganisms and Microspheres". *Encyclopedia of Environmental Microbiology*, 2003.
 28. RM Ford and RW Harvey. "Role of chemotaxis in the transport of bacteria through saturated porous media". *Advances in Water Resources*, Vol 30 (6–7), 2007.
 29. LM Lanning, RM Ford and T Long. "Bacterial Chemotaxis Transverse to Axial Flow in a Microfluidic Channel". *Biotechnology and Bioengineering*, Vol 100 (4), 2008.
 30. M Wang, RM Ford and RW Harvey. "Coupled Effect of Chemotaxis and Growth on Microbial Distributions in Organic-Amended Aquifer Sediments: Observations from Laboratory and Field Studies". *Environmental Science & Technology*, Vol 42 (10), 2008.
 31. T Long and R Ford. "Enhanced Transverse Migration of Bacteria by Chemotaxis in a Porous T-Sensor". *Environmental Science & Technology*, Vol 43 (5), 2009.
 32. KL Strobel, S McGowan, RD Bauer, C Griebler, J Liu and RM Ford. "Chemotaxis

-
- Increases Vertical Migration and Apparent Transverse Dispersion of Bacteria in a Bench-Scale Microcosm”. *Biotechnology and Bioengineering*, Vol 108 (9), 2011.
33. LI Robert and KS Subhas. “Bioremediation Technologies: Principles and Practice”. 1998
34. GE Quinton, RJ Buchanan Jr., DE Ellis and SH Shoemaker. “A method to compare groundwater cleanup technologies”. *Remediation Journal*, Vol 7 (4), 1997.
35. FA Caliman, BM Robu, C Smaranda, VL Pavel and M Gavrilesu. “Soil and groundwater cleanup: benefits and limits of emerging technologies”. *Clean Technologies and Environmental Policy*, Vol 13 (2), 2011.
36. JA MacDonald. “Evaluating Natural Attenuation for Groundwater Cleanup”. *Environmental Science and Technology*, Vol 34 (15), 2000.
37. PE Hardisty and E Özdemiroğlu. “The economics of groundwater remediation and protection”. 2004.
38. RD Bauer, P Maloszewski, YC Zhang, RU Meckenstock and C Griebl. “Mixing-controlled biodegradation in a toluene plume - Results from two-dimensional laboratory experiments”. *Journal of Contaminant Hydrology*, Vol 96, 2008.
39. RD Bauer, M Rolle, S Bauer, C Eberhardt, P Grathwohl, O Kolditz, RU Meckenstock and C Griebl. “Enhanced biodegradation by hydraulic heterogeneities in petroleum hydrocarbon plumes”. *Journal of Contaminant Hydrology*, Vol 105, 2009.
40. RD Bauer, M Rolle, P Kürzinger, P Grathwohl, RU Meckenstock and C Griebl. “Two-dimensional flow-through microcosms - Versatile test systems to study biodegradation processes in porous aquifers”. *Journal of Hydrology*, Vol 369, 2009.
41. RE Parales, JL Ditty and CS Harwood. “Toluene-Degrading Bacteria Are Chemotactic towards the Environmental Pollutants Benzene, Toluene, and Trichloroethylene”. *Applied Environmental Microbiology*, Vol 66 (9), 2000.
42. JGI Genome Portal. Genus species strain: *Pseudomonas putida* F1. JGI project id:

-
4000373. Culture collection: ATCC 700007.
43. G Alagappan and RM Cowan. "Effect of temperature and dissolved oxygen on the growth kinetics of *Pseudomonas putida* F1 growing on benzene and toluene". *Chemosphere*, Vol 54 (8), 2004.
 44. EM Hearn, DR Patel and B van den Berg. "Outer-membrane transport of aromatic hydrocarbons as a first step in biodegradation". *Proceedings of the National Academy of Sciences of the United States of America*, Vol 105 (25), 2008.
 45. DL Naftz, SJ Morrison, JA Davis, and CC Fuller. "Handbook of Groundwater Remediation Using Permeable Reactive Barriers". Academic Press, 2002.
 46. NR Thomson. "Bringing Groundwater Quality Research to the watershed Scale". International Association of Hydrological Sciences, 2005.
 47. Cold Spring Harbor Protocols; 2010; doi: 10.1101/pdb.rec12295.
 48. RW Harvey, DW Metge, N Kinner and N Mayberry. "Physiological considerations in applying laboratory-determined buoyant densities to predictions of bacterial and protozoan transport in groundwater: results of in-situ and laboratory tests". *Environmental Science and Technology*, Vol 31, 1997.
 49. J Liu, RM Ford and JA Smith. "Idling time of motile bacteria contributes to retardation and dispersion in sand porous medium". *Environmental Science and Technology*, Vol 45, 2011.
 50. M Auset and AA Keller. "Pore-scale processes that control dispersion of colloids in saturated porous media". *Water Resources Research*, Vol 49, 2004.
 51. Z Yan, EJ Bouwer and M Hilpert. "Coupled effects of chemotaxis and growth on traveling bacterial waves". *Journal of Contaminant Hydrology*, Vol 164, 2014.
 52. B Berkowitz, I Dror and B Yaron. "Contaminant Geochemistry: Interactions and Transport in the Subsurface Environment, Edition 2". Springer Sciences & Business, 2014.

-
53. R Boopathy. "Factors limiting bioremediation technologies". *Bioresource Technology*, Vol 74 (1), 2000.
 54. J Troquet, C Larroche and CG Dussap. "Evidence for the occurrence of an oxygen limitation during soil bioremediation by solid-state fermentation". *Biochemical Engineering Journal*, Vol 13 (2-3), 2003.
 55. RB Doctor, R Dahl, L Fouassier, G Kilic and JG Fitz. "Cholangiocytes exhibit dynamic, actin-dependent apical membrane turnover". *American Journal of Physiology - Cell Physiology*, Vol 282 (5), 2002.
 56. TA Vida and SD Emr. "A new vital stain for visualizing vacuolar membrane dynamics and endocytosis in yeast". *Journal of Cell Biology*, Vol 128 (5), 1995.
 57. D Horstmann. "From 1970 until present: the Keller–Segel model in chemotaxis and its consequences I". 2003.
 58. KC Chen, PT Cummings, and RM Ford. "Perturbation Expansion of Alt's Cell Balance Equations Reduces to Segel's One-Dimensional Equations for Shallow Chemoattractant Gradients". *SIAM Journal of Applied Mathematics*, Vol 59 (1), 1995.
 59. O Paliy and TS Gunasekera. "Growth of *E. coli* BL21 in minimal media with different gluconeogenic carbon sources and salt contents". *Applied Microbial and Cell Physiology*, Vol 73, 2007.
 60. B Berkowitz, I Dror, and B Yaron. "Contaminant Geochemistry: Interactions and Transport in the Subsurface Environment, Edition 2". Springer Sciences & Business, 2014.
 61. G Bratbak, and I Dundas. "Bacterial dry matter content and biomass estimations". *Applied and Environmental Microbiology*, Vol 8 (4), 1984.
 62. GS Campbell. "A simple method for determining unsaturated conductivity from moisture retention data". *Soil Science*, 1974.

63. JW Barton, and RM Ford. "Determination of effective transport-coefficients for bacterial migration in sand columns". *Applied Environmental Microbiology*, Vol 61(9), 1995.

Appendices

A1. Uranine quantification

Uranine as a conservative tracer was injected from the inlet together with cells to trace the flow pattern in the microcosm. Uranine was quantified by measuring its absorbance with a plate reader. As samples from the outlet ports were subjected to filtration prior to measurement, the PpF1 cells wouldn't interfere uranine quantification at this wavelength. Uranine showed an absorbance peak at wavelength of 490 nm, so this wavelength was used for quantifying uranine. Uranine solution was serially diluted and the calibration curve was drawn as below by plotting the absorbance value at 490 nm versus the uranine concentration.

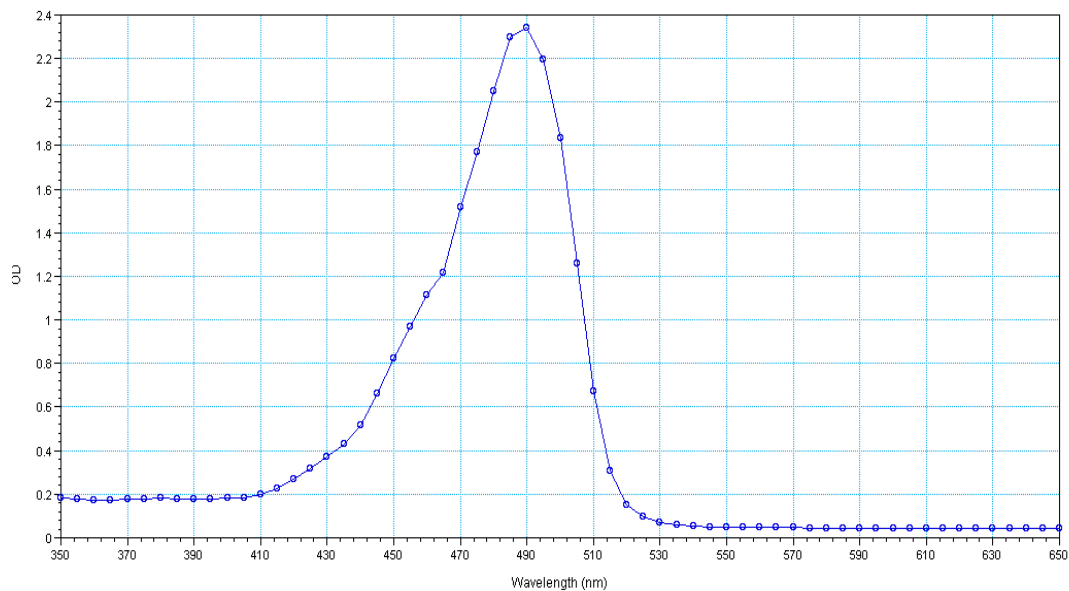


Figure A1.1 Adsorption spectrum of uranine. Uranine has an absorption peak at ~490 nm.

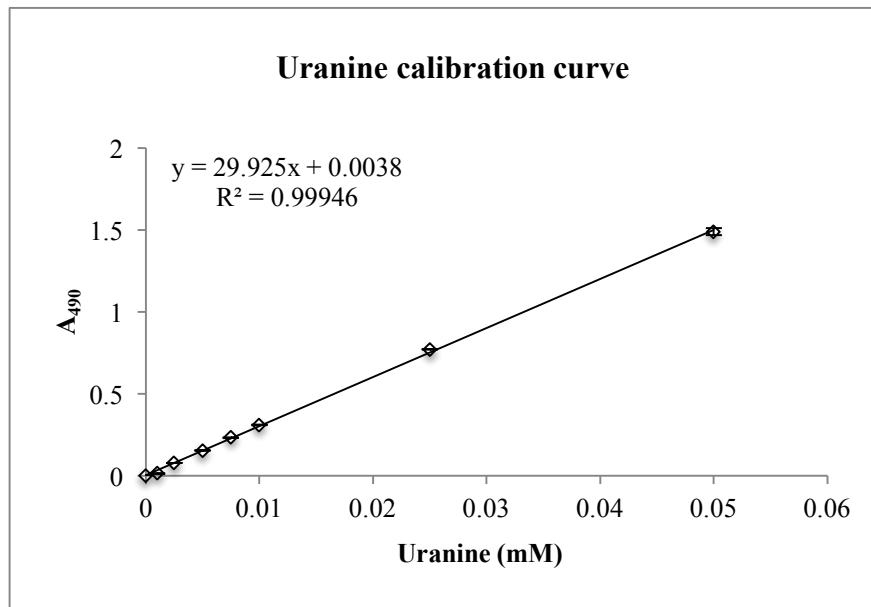


Figure A1.2 Calibration curve of uranine, measured with absorption at 490 nm.

Table A1.1 Calibration curve of uranine measured with adsorption at 490 nm.

Uranine (mM)	Avr., A ₄₉₀	SD, A ₄₉₀	CV, A ₄₉₀
0	0	0	
0.001	0.015	0.001	5%
0.0025	0.079	0.000	0%
0.005	0.154	0.001	1%
0.0075	0.234	0.003	1%
0.01	0.311	0.001	0%
0.025	0.771	0.002	0%
0.05	1.488	0.021	1%

A2. Cell enumeration

For enumeration, cells suspended in the sample were collected by centrifugation, stained with a fluorescent dye, confirmed of the fluorescent property by fluorimeter, and then cell numbers were counted with a flow cytometer.

A2.1. Cell staining

Cells were stained with a fluorescent dye in order to remove the possible signal interference from sand and debris *etc.* when counting with flow cytometer. The dye to stain the cells is FM® 4-64 Dye (N-(3-Triethylammoniumpropyl)-4-(6-(4-(Diethylamino) Phenyl) Hexatrienyl) Pyridinium Dibromide) (Life Technologies, CAT# T3166). FM® 4-64 Dye is a lipophilic styryl compound which is nontoxic to cells and virtually nonfluorescent in aqueous media. It is believed to insert into the outer leaflet of the surface membrane where it becomes intensely fluorescent. This method of membrane labeling has been used to selectively visualize plasma membrane in cultured bacteria (55, 56).

Cells were stained according to the following the procedure. 500 uL of sample containing cells was pelleted by centrifugation at 10,000 xg for 5 min, then supernatant was discarded and cells were suspended in 1 mL of filtered M9 media via vortexing and collected by centrifugation again. This washing step was performed twice. Then cells were suspended in 1 mL of filtered M9 media again and 1 uL 5 mg/mL of FM® 4-64 Dye stock solution was added and mixed well together. The solution was covered by foil and put at room temperature for 10 min for staining. Then washing was performed as the same procedure as above and stained cells were finally suspended in at a final volume of 0.5 mL M9 media for further analysis with fluorimeter and flow cytometer.

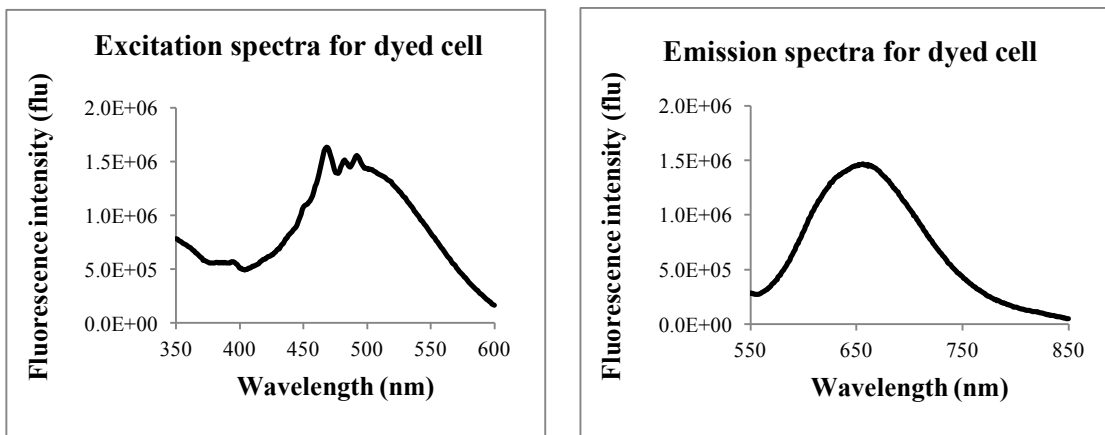


Figure A2.2.1 Excitation and emission spectrum of cells stained with FM4-64. Ex/Em for stained cells is ~ 500 nm/650 nm.

A2.2. Fluorimeter analysis

A fluorimeter is a device used to measure parameters of fluorescence. The intensity and wavelength distribution of the emission spectrum of the sample can be measured after excitation by a certain spectrum of light. These parameters are used to identify the presence and the amount of specific molecules in a medium.

PpF1 cells stained with FM[®] 4-64 (57, 58) were reported to be excited at 506 nm and emitted at 750 nm. In reference to this, to optimize the excitation and emission wavelength in current setting of the experiment, the stained cell suspension was first subjected to emission scan with excitation wavelength of 500 nm, then with the emission wavelength that exhibited maximum fluorescence thereof, excitation scan was done thereafter. Slit number was set as 5 for both excitation and emission scans. 2 mL of cell suspension was used for measurement and cell concentration was about 0.5 OD₅₉₀ as measured before dying with FM[®] 4-64.

The result shows that the stained cells exhibit maximum excitation wavelength at around 500 nm and maximum emission wavelength at around 650 nm (**Figure A2.2.1**). These values fall approximately within the analysis range of the current laser configuration of the flow cytometer, which is integrated with excitation wavelength of 488 nm and emission filter of 610/20 nm at the detector position FL3.

A2.3. Flow cytometer analysis

Flow cytometry is a process of performing measurements on particles including cells that are in liquid suspension. It is a technology that simultaneously measures and analyzes multiple characteristics of particles as they pass through a beam of light, such as relative size, internal complexity and fluorescence intensity. Typically particles or cells from 0.2 – 50 micrometers in size are suitable for flow cytometry analysis. A flow cytometer is composed of three main subsystems: fluidics, optics, and electronics. The fluidics subsystem transports the particles of interest to the interrogation point where they interact with the excitation sources. The optics subsystem provides the excitation sources and the components to collect light signals and route them to the appropriate detectors.

The electronic subsystem converts light signals to equivalent electronic signals. When particles flow through the laser beam, light scattering occurs in two directions: the forward scatter light which gives the relative particle size information, and the side scatter light which gives the information on particle granularity or internal complexity. If the particles contain fluorochromes, either by staining or having been engineered to express fluorescent molecules in the case of cells, this particle population can also be identified according to the type of the fluorochrome that they have.

A threshold is the lowest signal intensity value an event can have for it to be recorded by

the cytometer. The signal pulse must exceed the level set on the threshold to be recorded as an event on any other channel. When choosing the appropriate threshold value, debris and undesired events should be eliminated without inadvertently eliminating relevant events. If this is the first time a particular experiment is performed, it might not be clear which events are the correct ones, so they must be identified. Once the particles have been identified, the threshold should be set low enough to ensure the entire population is captured. The ideal placement of the threshold is somewhere between the particles of interest and the noise floor.

The BD AccuriTM C6 flow cytometer has a default threshold setting of FSC-H as 80,000, which has been optimized for mammalian cell analysis. As PpF1 is typically 1 μm in length, much smaller than mammalian cells, the FSC-H threshold must be further lowered for the analysis in this study, or the majority of cells would be excluded from the recorded events. Additionally, the stained cells provide an additional threshold option of FL3-H, to separate them from nonfluorescent noises.

During the optimization process of flow cytometer parameters, both stained and unstained cells were prepared. Cells were cultured to logarithmic phase in LB media under optimal condition (30 °C, 150 rpm, 9 h culture). Unstained cells were prepared by direct centrifugation of cell culture at 10,000 $\times g$ for 5 min, then supernatant was discarded and cells were suspended in fresh filtered analysis media and collected by centrifugation again. This washing step was performed twice. Then cell concentration was adjusted to OD₅₉₀ value of 1, and this will be defined as 1x OD cell concentration in the following statements for convenience. Accordingly, 0.1x OD cell concentration means cell concentration is where the absorbance value is 0.1 at 590 nm. For stained cell samples, the same staining procedure was performed as mentioned above in the “staining

cell” section.

Table A2.3.1 Optimization of FSC-H threshold for cell counting. No cells (M9 media only), unstained cells and stained cells were counted with various FSC-H thresholds.

1x M9 media				
	Threshold	10k	20k	30k
Size	FSC-H mean	23,282	37,717	63,715
	FSC-H median	11,259	26,636	43,539
FM64-4 Signal	FL3-H mean	200	531	1,085
	FL3-H median	166	236	487
Unstained cells				
	Threshold	10k	20k	30k
Size	FSC-H mean	57,718	64,042	71,843
	FSC-H median	49,599	55,428	62,423
FM64-4 Signal	FL3-H mean	307	310	315
	FL3-H median	290	293	297
Stained cells				
	Threshold	10k	20k	30k
Size	FSC-H mean	60,136	58,991	66,795
	FSC-H median	52,008	51,008	58,665
FM64-4 Signal	FL3-H mean	26,642	26,994	28,056
	FL3-H median	23903	24554	25639

For each analysis, 300 uL of sample containing cells was injected and the washing step with filtered DW for 2 min was performed between every measurement. Back-flushing and unclogging were done from time to time.

Firstly, FSC-H threshold was optimized (**Table A2.3.1, Figure A2.3.1**). FSC-H threshold

was optimized with 1x cell concentration of unstained cells and stained cells. M9 media was also analyzed as background analysis. Optimization was done with single threshold of FSC-H, and values of 50k, 30k, 20k, and 10k were tested.

With the increasing threshold of FSC-H, mean as well as median size of the detected particles showed approximately increasing trend for both unstained and stained cell samples. This is not surprising, as higher FSC-H threshold would exclude more events including the particles of interest while excluding the false positives in the sample. Data for M9 media only with FSC-H threshold of 10k, however, shows higher FSC-H and FL3-H mean values as well as median values than the sample with stained cells. This is probably due to the residual dyes from the previously run experiments for stained cells with various FSC-H thresholds. Stained cells exhibited higher FL3-H values compared with unstained cell as well as M9 media, as FL3-H recorded events by the fluorescence signal generated by the particles of interest. Change of FSC-H threshold hardly affected the FL3-H value. It could be noticed that M9 media also gave a good number of events reading, necessitating the inclusion of another threshold for the removal of background noise. Based on the comparison result of different FSC-H threshold, 10k was chosen for cell enumeration.

Secondly, FL3-H threshold was optimized. With FSC-H threshold value set as above-optimized value of 10k, further optimization of FL3-H threshold was performed with 0.1x cell concentration of stained and unstained cells. Plotting event number versus FL3-H, the majority of events in stained cell sample fell in FL3-H higher than 1k, while less than 1k for unstained cell sample and M9 media. (**Figure A2.3.2**)

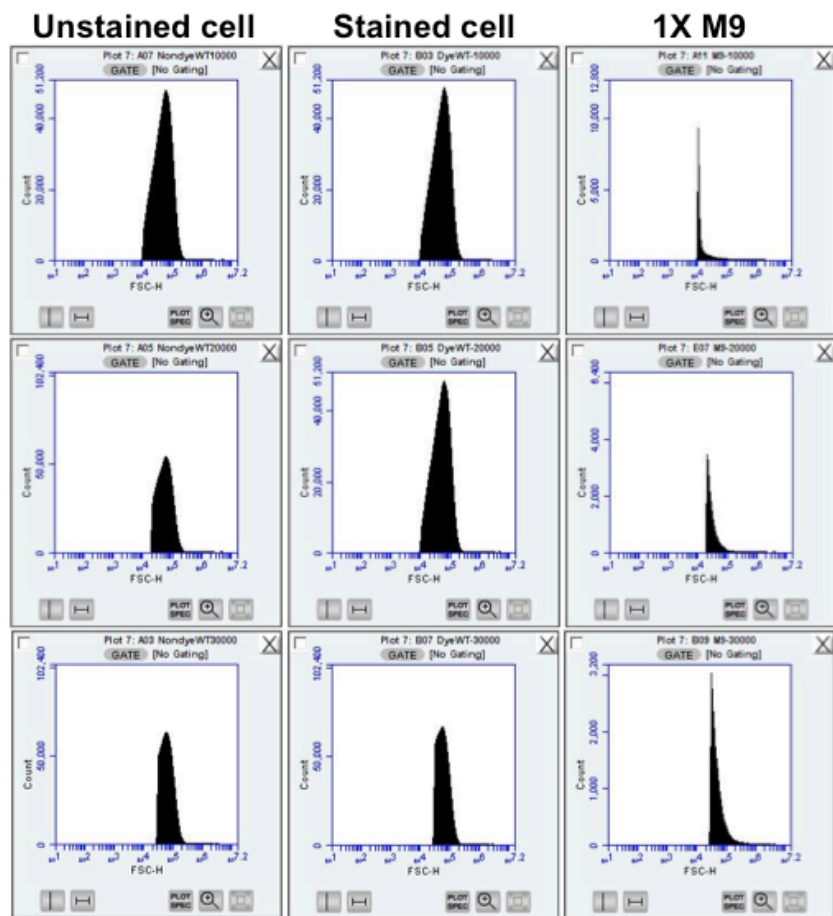


Figure A2.3.1 Optimization of FSC-H threshold for cell counting. M9, unstained cells and stained cells were counted with various FSC-H thresholds. In the vertical direction from top to bottom, FSC-H thresholds are 10 k, 20 k and 30 k in turn.

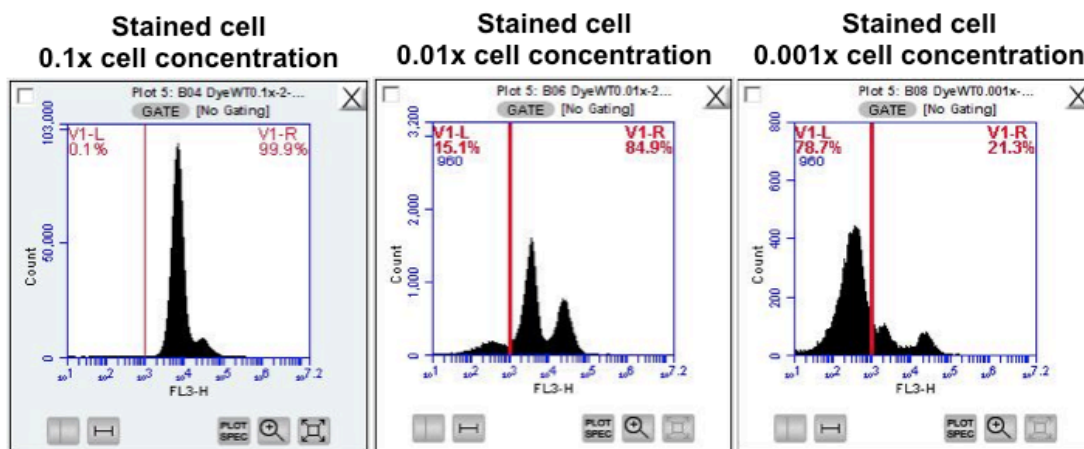


Figure 6.2.3.2 Optimization of FL3-H threshold. Stained cells, unstained cells and M9 samples were counted with FSC-H threshold of 10k, and cell counts were plotted over FL3-H value.

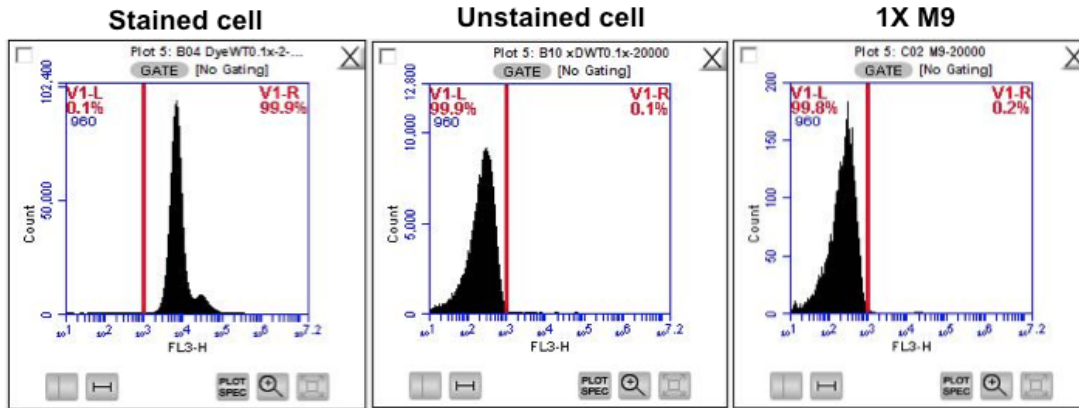


Figure A2.3.3 Cell counting of serially diluted stained cell samples. Cell counts of 1x, 0.1x and 0.01x stained cell samples were plotted over FL3-H value.

Table A2.3.2 Event counting of M9 with various parameters. Double thresholds - FSC-H of 10 k and FL3-H of 1 k - gave negligible recordings.

Sample	Threshold		# Events
	FSC-H	FL3-H	
M9	10k	None	21077
M9	10k	1k	6
M9	9k	1k	67
M9	8k	1k	149
M9	7k	1k	379
M9	5k	1k	1676
M9	10k	900	76
M9	10k	800	314

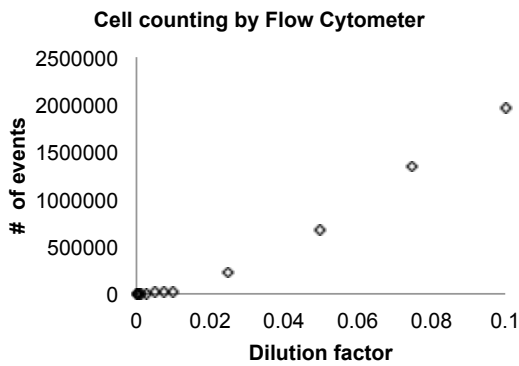
Event number versus FL3-H was also plotted for serially diluted stained cell samples. **(Figure 6.2.3.3)** A small number of the recordings below FL3-H value of 1000 is supposed to be background noises.

With further dilution, less events were recorded at the region where FL3-H was higher than 1k. Regarding previous result, FL3-H threshold of 1k was selected in addition to FSC-H threshold of 10k to remove the noises from unstained cells and debris *etc.*

Thirdly, background from M9 was checked. To check background from M9 media, flow cytometer analysis was done with buffer only with double thresholds, FSC-H threshold of 10k and FL3-H threshold of 1k.

M9 gave events number of 6 with double threshold set as above, which is almost negligible comparing with the event number recorded for stained cells. **(Table A2.3.2)**

Fourthly, the calibration curve was drawn with the above parameters. With optimized double thresholds, FSC-H threshold of 10k and FL3-H threshold of 1k, flow cytometer analysis was done with serially diluted stained cell samples and the recorded events were plotted versus the cell dilution factor. It showed a refined linear correlation within the range of 0.01x to 0.1x cell concentration. At lower cell concentration range, it showed linear correlation with a different slope. **(Figure A2.3.4)**



Dilution factor	# events
0.00010	266
0.00025	574
0.00050	735
0.00075	1135
0.00100	1547
0.00250	5531
0.00500	11580
0.00750	18658
0.01000	23511
0.02500	219700
0.05000	673706
0.07500	1339883
0.10000	1959503

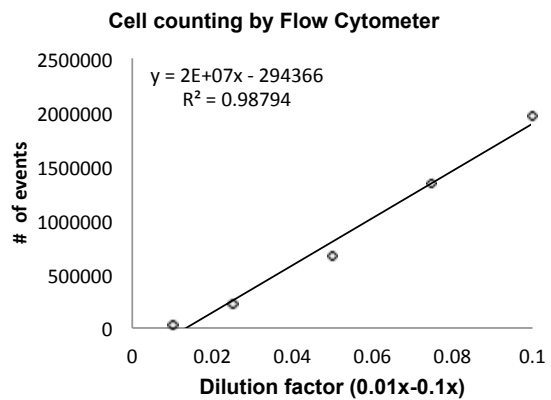
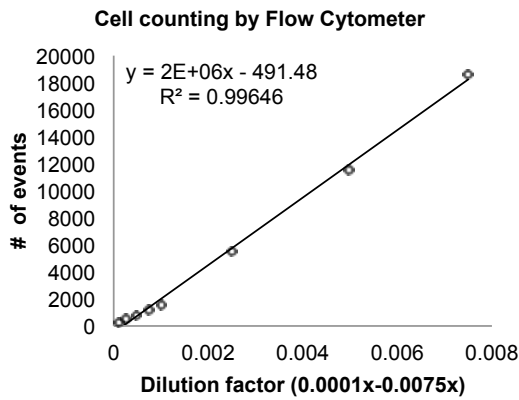


Figure. A2.3.4 Calibration curve of cell counting with flow cytometer. Double thresholds - FSC-H of 10 k and FL3-H of 1 k - were used.

A3. Toluene quantification by GC-MS

Toluene fraction was quantified from 2 mL sample aliquots by liquid-liquid extraction with 0.7 mL of cyclohexane containing 9.42 mg/L ethylbenzene as internal standard. Aqueous sample and the organic solvent were mixed together in a sealed glass vial, and then, after shaking for 1 h at room temperature at 100 rpm, the organic solvent phase was collected for further GC-MS analysis. GC-MS analysis was done with Shimadzu GCMS-QP2010 Plus (Kyodo, Japan) equipped with a DB-5MS column with dimension of 0.5 μm film thickness, 0.25 i.d., 30 m length from Agilent (Santa Clara, CA, United States). Sample injection was on splitless mode and the flow rate of the carrier gas helium was 1 mL min⁻¹. The oven temperature was 40 °C for 1 min, then ramped first at a rate of 20 °C min⁻¹ to 180 °C and then at a rate of 30 °C to 300 °C where it was held for 1 min. The MS was operated at 280 °C in the SIM scan mode for the masses 91.00 and 98.00. Washing step with pure extraction solvent was done with the same temperature program between each sample run to remove any residual contaminant peaks.

For toluene calibration curve, 2 mL of calibration samples, which are microcosm buffer containing various concentrations of toluene, were incubated with 0.7 mL cyclohexane containing ethylbenzene as described above, and then the solvent phase were subjected to GC-MS analysis after 1 h of shaking. A small background peak appeared as noise with the sample where organic solvent was incubated with buffer only. The standard deviation was determined and the limit of detection of this established quantification protocol was determined as approximately three times of this standard deviation value. The noise information and calibration curve are shown below. The dynamic range is toluene concentrations of 1e-8 (v/v) to 1e-5 (v/v), so samples were subjected to dilution when toluene concentration in them run above this range.

Table A3.1 GC-MS noise peak information (n=3).

	Avr.	SD	CV
Buffer	2.88e4	412	1%

Table A3.2 Toluene calibration curve from GC-MS (n=3), noise peak area has been deducted from original value.

Toluene (v/v)	Avr.	SD	CV
1.00E-08	4.65e3	1.32e3	28%
1.00E-07	2.38e4	2.04e3	9%
1.00E-06	2.94e5	8.52e3	3%
1.00E-05	5.49e6	3.55e5	6%

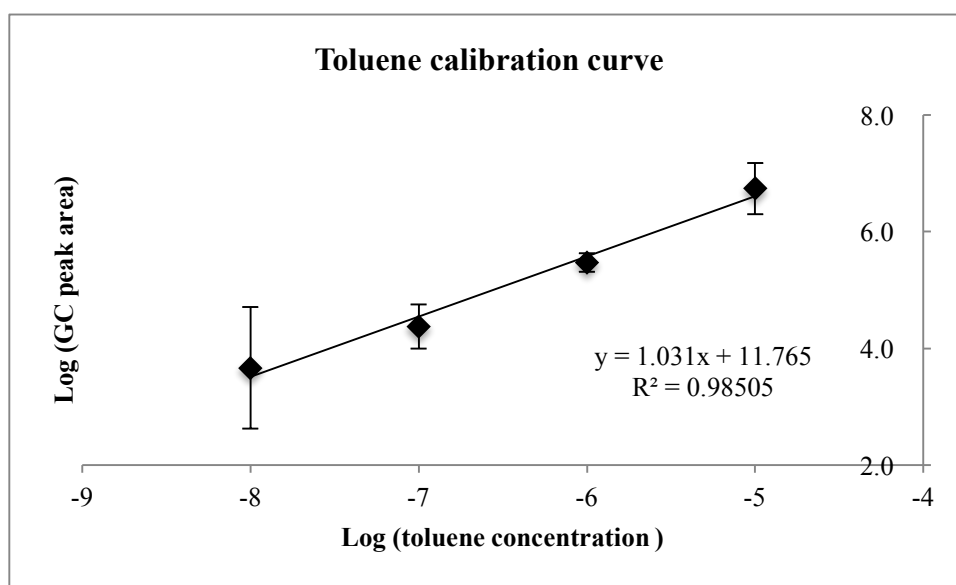


Figure A3.1 Toluene calibration curve by GC-MS analysis.

A4. Moment analysis

Moment analysis was done to analyze the vertical movement of the analyte.

The first moment, namely the mean value μ , represents the center of mass of the analyte and was determined from the following equation:

$$m_1 = \mu = \hat{y} = \frac{\sum(C_i * y_i)}{\sum C_i}$$

The second moment, namely the variance σ^2 , represents the spread of analyte and was determined from the following equation:

$$m_2 = \sigma^2 = \frac{\sum C_i * (y_i - \hat{y})^2}{\sum C_i}$$

The third moment, namely the skewness of the peak, represents the preferable movement of the analyte:

$$m_3 = \gamma = \frac{\sum C_i * (y_i - \hat{y})^3}{\sum C_i}$$

Where y_i is the outlet number, C_i is the analyte concentration percentage as compared with the inlet.

A5. Gaussian fitting

Gaussian fitting was done with “Dynamic 3-parameter Gaussian fitting” module in SigmaPlot software, the equation being:

$$f(x) = ae^{-\frac{(x-b)^2}{2c^2}}$$

where “b” denotes the center of the peak and “c” equals to “ σ ” which denotes the peak breadth.

A6. Medium and buffer recipes (47, 59)

- **M9 medium (1 L)**

Na₂HPO₄ 2.7 g, KH₂PO₄ 3 g, NaCl 0.5 g, NH₄Cl 1 g, MgSO₄ 0.1 mM, CaCl₂ 0.1 mM,
pH 7.0 (adjust with 10 M NaOH)

- **LR plate (1 L)**

KH₂PO₄ 24g, NaOH 1g, (NH₄)₂SO₄ 1.675g, MgSO₄ •H₂O 0.3 g, FeSO₄•7H₂O 3 mg,
concentrated H₂SO₄ 10 uL, noble agar 1.5%

- **LR liquid media (1 L)**

KH₂PO₄ 24g, NaOH 1g, (NH₄)₂SO₄ 1.675g, MgSO₄ •H₂O 0.3 g, FeSO₄•7H₂O 3 mg,
concentrated H₂PO₄ 10 uL

A7. 2-D microcosm experiments: scheme, image, analyte concentration profile, and data analysis

2-D microcosm experiments were conducted by simultaneous injection of two of three PpF1 strains into the microcosm in each run, which makes total of 6 runs. The scheme of each 2-D microcosm experiment, along with the actual image taken at the end and the concentration profiles of the analyte, are shown in **Figure A7.1**. Gaussian fitting was done for symmetric peaks and moment analysis was done for asymmetric peaks, as shown in **Table A7.2**.

Table A7.1 Three types of PpF1 strains and genotype

Strain label	Strain type	Strain genotype
PpF1 f0	PpF1 wild type	PpF1 wild type
PpF1 f1	PpF1 single knockout	PpF1 ($\Delta todX$)
PpF1 f3	PpF1 triple knockout	PpF1 ($\Delta todX\Delta cymD\Delta F1fadL$)

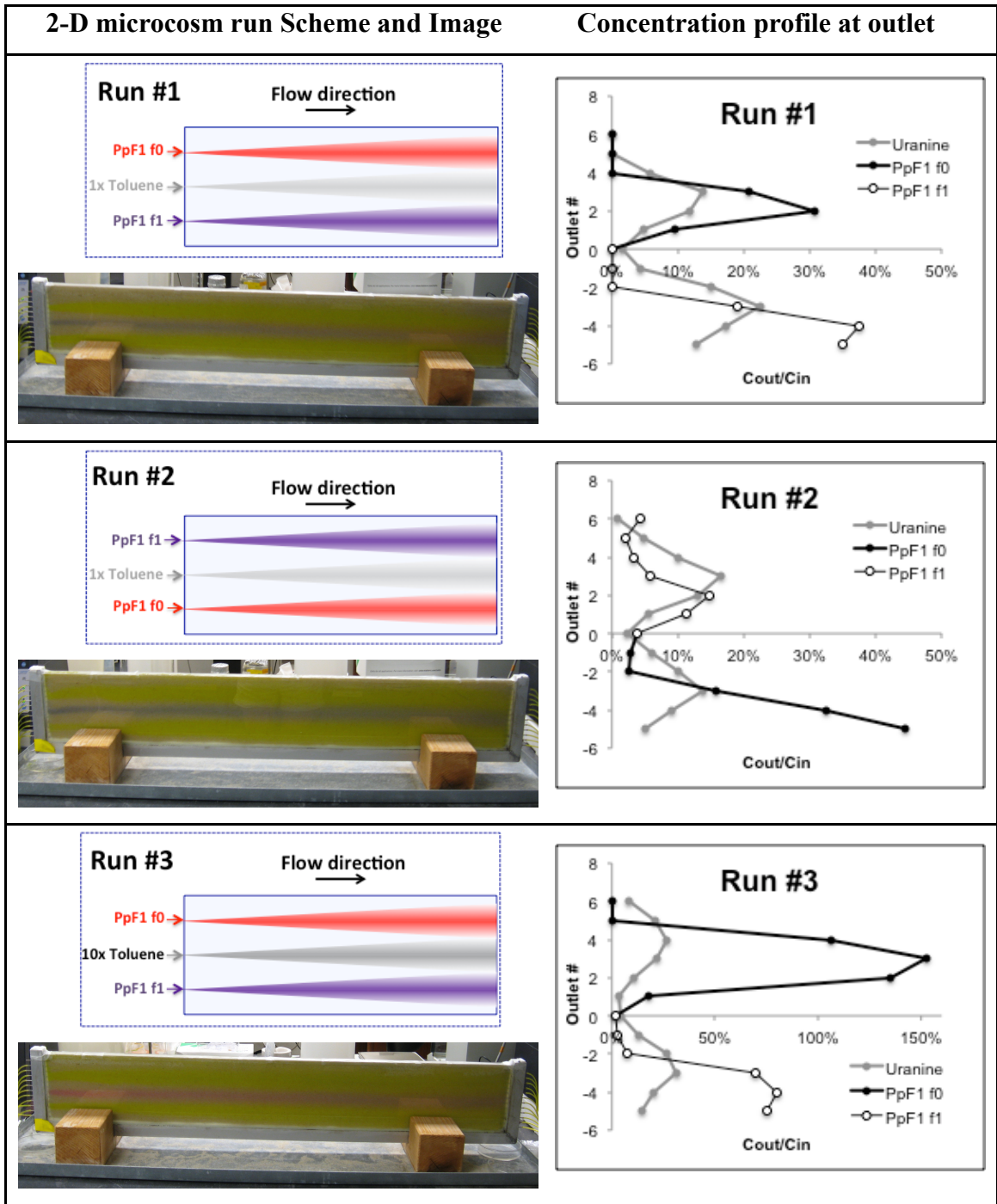


Figure A7.1 2-D Microcosm experiments with PpF1 f0, PpF1 f1 and PpF1 f3: scheme, images and concentration profiles of uranine and PpF1 cells at the outlet (continued on next page).

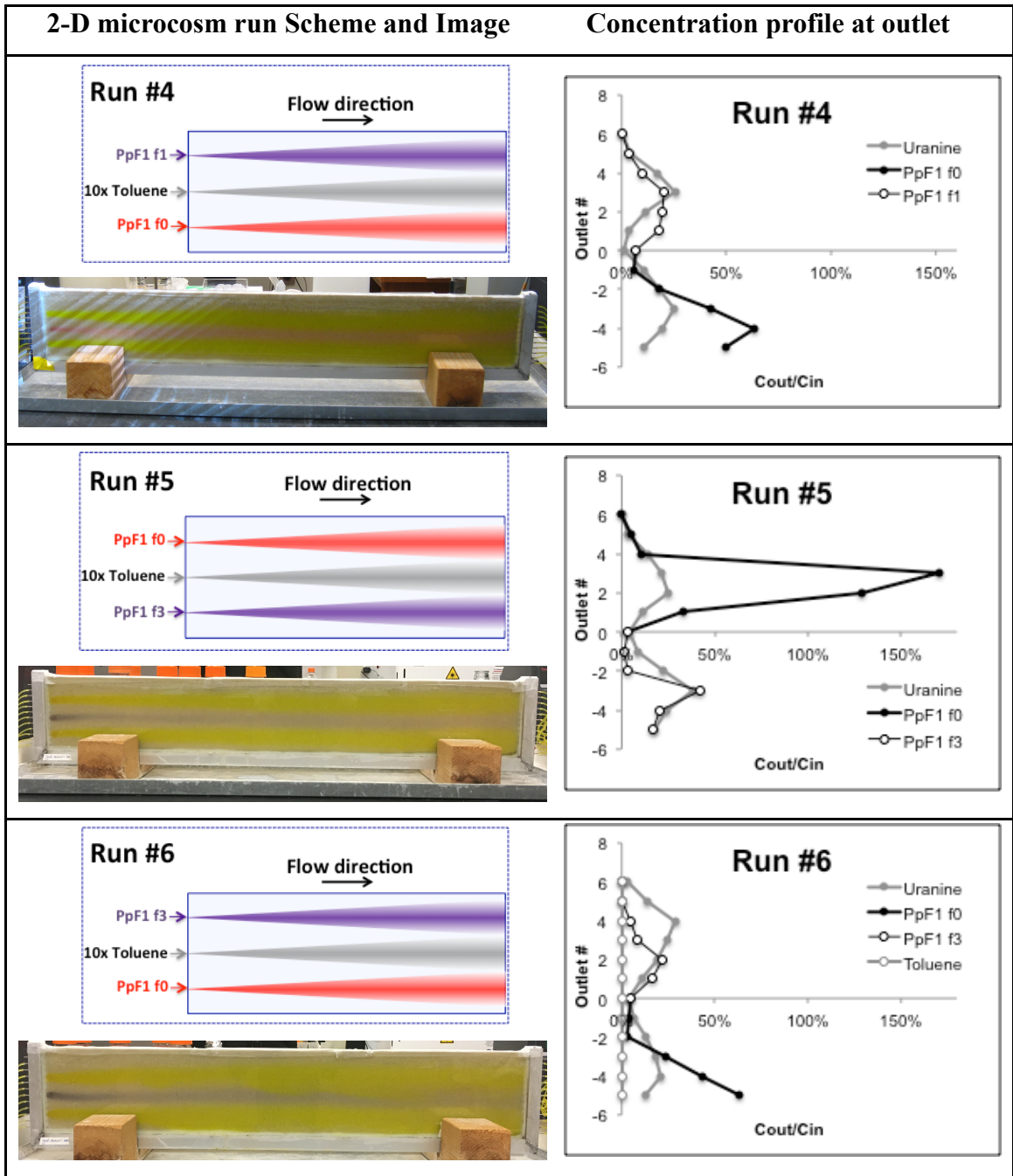


Figure A7.2 2-D Microcosm experiments with PpF1 f0, PpF1 f1 and PpF1 f3: scheme, images and concentration profiles of uranine and PpF1 cells at the outlet (continued from last page).

Table A7.2 List of peak parameters from Gaussian fitting and moment analysis for uranine and PpF1 strains in 2-D microcosm run #1 ~ #5 (#5' is repeat run of #5). *Italic numbers* are from Gaussian fitting and others from moment analysis.

	Inject position	Uranine			Cell		
		<i>Mean</i> \hat{y}	<i>Breadth</i> σ^2	Skewness Υ	Mean \hat{y}	Breadth σ^2	Skewness Υ
Run #1	Top	<i>-0.41</i>	<i>1.09</i>	-0.25	-0.28	0.46	-0.25
	Bottom	<i>-0.34</i>	<i>2.10</i>	0.30	-0.97	0.56	0.30
Run #2	Top	<i>-0.16</i>	<i>1.72</i>	0.83	-0.45	2.81	0.83
	Bottom	<i>0.11</i>	<i>2.29</i>	1.60	-1.21	1.54	1.60
Run #3	Top	<i>0.90</i>	<i>1.95</i>	-0.20	-0.81	0.77	-0.20
	Bottom	<i>0.12</i>	<i>2.43</i>	0.76	-1.06	0.93	0.76
Run #4	Top	<i>0.15</i>	<i>0.93</i>	0.14	-0.83	1.66	0.14
	Bottom	<i>-0.07</i>	<i>2.14</i>	0.98	-0.61	1.58	0.98
Run #5	Top	<i>-0.49</i>	<i>1.64</i>	-0.17	-0.06	0.63	-0.17
	Bottom	<i>-0.20</i>	<i>1.89</i>	0.80	-0.36	1.22	0.80
Run #6	Top	<i>0.27</i>	<i>2.34</i>	0.31	-1.26	1.08	0.31
	Bottom	<i>-0.53</i>	<i>3.02</i>	1.57	-0.92	1.44	1.57
Run #5'	Top	<i>0.81</i>	<i>1.59</i>	-0.20	0.11	0.74	-0.20
	Bottom	<i>0.17</i>	<i>2.55</i>	0.28	-0.66	0.89	0.28

A8. COMSOL parameter calculations

List of given parameters:

$$\varepsilon = 0.37 \quad (62)$$

$$V_f = \frac{l_{\text{microcosm}}}{\text{traveling time}} = \frac{0.95 \text{ m}}{17 \times 3600 \text{ s}} = 1.55e - 5 \frac{\text{m}}{\text{s}} \quad (\text{this study})$$

$$U_{\text{avg}} = \varepsilon \times V_f = 0.37 \times 1.55e - 5 \frac{\text{m}}{\text{s}} = 5.74e - 6 \frac{\text{m}}{\text{s}}$$

$$MW_{\text{toluene}} = 92.14 \text{ g/mol}$$

$$MW_{\text{oxygen}} = 32.00 \text{ g/mol}$$

$$D_{a,\text{bulk}} = 9.00e - 10 \frac{\text{m}^2}{\text{s}}$$

$$D_{b,\text{bulk}} = 3.20e - 10 \frac{\text{m}^2}{\text{s}} \quad (48)$$

$$D_{o,\text{bulk}} = 1.97e - 9 \frac{\text{m}^2}{\text{s}}$$

$$D_{ax,\text{ref}} = 1.95e - 8 \frac{\text{m}^2}{\text{s}} \quad (38)$$

$$D_{ay,\text{ref}} = 1.85e - 9 \frac{\text{m}^2}{\text{s}} \quad (38)$$

$$\alpha_{ay} = 6.00e - 5 \text{ m} \quad (5)$$

$$V_{f,\text{ref}} = 2.00e - 5 \frac{\text{m}}{\text{s}} \quad (38)$$

$$Y_{b/t} = 1.28 \frac{\text{g cell}}{\text{g toluene}}$$

$$q_e = \frac{\mu_{m,o}}{Y_{b/o}} = 2.60e - 4 \frac{\text{g cell}}{\text{g oxygen} \cdot \text{s}}$$

$$\sigma_b^2 = 7.00e - 5 \text{ m}$$

1. Bacterial setting velocity: v_{set}

$$v_{set} = \frac{l_{set}}{t} = \frac{1 \text{ cm}}{17 \text{ h} \times 3600 \text{ s}} \times \varepsilon = 6.04e - 8 \text{ cm/s}$$

2. Bacterial cell volume: V_b

Assuming average bacterial cell size: length $l_b = 0.5 \mu\text{m}$, diameter $d_b = 0.5 \mu\text{m}$

The volume of single cell:

$$V_b = \frac{\pi}{4} d_b^2 l_b = \frac{\pi}{4} (0.5 \mu\text{m})^2 \times (0.5 \mu\text{m}) = 9.82e-20 \text{ m}^3$$

Assuming wet cell density is 1 g/cm^3 , and bacterial cell is approximately composed of 80% of water (61), the dry cell density:

$$\rho_b = 20\% \times 1 \frac{\text{g}}{\text{cm}^3} = 2.00e5 \frac{\text{g}}{\text{m}^3}$$

So, mass of dry single cell:

$$m_b = \rho_b \times V_b = (2.00e5 \frac{\text{g}}{\text{m}^3}) \times (9.82e-20 \text{ m}^3) = 1.96e-14 \text{ g}$$

So, molecular weight of single dry cell:

$$MW_b = m_b \times N_A = 1.96e-14 \text{ g} \times 6.02e23 = 1.18e10 \frac{\text{g}}{\text{mole}}$$

3. Yield coefficient on toluene: $Y_{b/a}$ (51)

$$Y_{b/a} = 1.28 \frac{\text{g cell}}{\text{g toluene}} = \frac{1.28 \text{ g} / MW_b}{1 \text{ g} / MW_{\text{toluene}}} = \frac{2.55 \text{ g} / 1.18e10 \frac{\text{g}}{\text{mole}}}{1 \text{ g} / 92.14 \frac{\text{g}}{\text{mole}}} = 9.98e-9 \frac{\text{mole cell}}{\text{mole toluene}}$$

4. Maximum oxygen consumption rate: q_e

$$q_e = \frac{\mu_{m,o}}{Y_b} = 2.6e - 4 \frac{\text{g oxygen}}{\text{g cell} \cdot \text{s}} = \frac{2.60e-4 \text{ g} / MW_o}{1 \text{ g} / MW_b \cdot \text{s}} = \frac{2.6e-4 \text{ g} / 32.00 \frac{\text{g}}{\text{mole}}}{1 \text{ g} / 1.18e10 \frac{\text{g}}{\text{mole}} \cdot \text{s}} = 9.60e4$$

$\frac{\text{mole oxygen}}{\text{mole cell} \cdot \text{s}}$

5. Toluene longitudinal dispersivity: α_{ax}

Since

$$D_{ax,ref} = \alpha_{ax} \times V_{f,ref} + \frac{D_{a,eff,ref}}{\varepsilon_{ref}}$$

$$D_{ay,ref} = \alpha_{ay} \times V_{f,ref} + \frac{D_{a,eff,ref}}{\varepsilon_{ref}}$$

So,

$$\begin{aligned} \alpha_{ax} &= \frac{D_{ax,ref} - D_{ay,ref} + \alpha_{ay} \times V_{f,ref}}{V_{f,ref}} \\ &= \frac{1.95e - 8 \frac{m^2}{s} - 1.85e - 9 \frac{m^2}{s} + 6.00e - 5 m \times 2.00e - 5 \frac{m}{s}}{2.00e - 5 \frac{m}{s}} \\ &= 9.41e - 4 m \end{aligned}$$

6. Toluene longitudinal dispersion coefficient: D_{ax}

According to Millington-Quirk equation tells the relation between porosity ε and tortuosity τ (62):

$$\tau = \varepsilon^{-\frac{1}{3}}$$

Since

$$\frac{D_{toluene,eff}}{\varepsilon} = \frac{D_{toluene,bulk}}{\tau} \quad (63)$$

So,

$$\frac{D_{a,eff}}{\varepsilon} = \frac{D_{a,bulk}}{\tau} = \frac{D_{a,bulk}}{\varepsilon^{-\frac{1}{3}}} = \frac{9.00e - 10 \frac{m^2}{s}}{0.37^{-\frac{1}{3}}} = 6.46e - 10 \frac{m^2}{s}$$

So,

$$\begin{aligned} D_{ax} &= \alpha_{ax} \times V_f + \frac{D_{toluene,eff}}{\varepsilon} = 9.41e - 4 m \times 1.55e - 5 \frac{m}{s} + 6.46e - 10 \frac{m^2}{s} \\ &= 1.53e - 8 \frac{m^2}{s} \end{aligned}$$

7. Toluene transverse dispersion coefficient: D_{ay}

$$D_{ay} = \alpha_{ay} \times V_f + \frac{D_{a,eff}}{\varepsilon} = 6.00e - 5 \text{ m} \times 1.55e - 5 \frac{\text{m}}{\text{s}} + 6.46e - 10 \frac{\text{m}^2}{\text{s}}$$

$$= 1.58e - 9 \frac{\text{m}^2}{\text{s}}$$

8. Bacterial cell transverse dispersion coefficient: D_{by}

According to Einstein relation:

$$D_T = \frac{\sigma^2}{2t}$$

So,

$$D_{by} = \frac{\sigma_b^2}{2t} = \frac{7.00e - 5 \text{ m}^2}{2 \times 19 \times 3600 \text{ s}} = 5.12e - 10 \frac{\text{m}^2}{\text{s}}$$

9. Bacterial cell transverse dispersivity: α_{by}

$$\frac{D_{b,eff}}{\varepsilon} = \frac{D_{b,bulk}}{\tau} = \frac{D_{b,bulk}}{\varepsilon^{-\frac{1}{3}}} = \frac{3.20e - 10 \frac{\text{m}^2}{\text{s}}}{0.37^{-\frac{1}{3}}} = 2.30e - 10 \frac{\text{m}^2}{\text{s}}$$

Since

$$D_{by} = \alpha_{by} \times V_f + \frac{D_{b,eff}}{\varepsilon}$$

So,

$$\alpha_{by} = \frac{1}{V_f} \left(D_{by} - \frac{D_{b,eff}}{\varepsilon} \right) = \frac{1}{1.55e - 5 \frac{\text{m}}{\text{s}}} \left(5.12e - 10 \frac{\text{m}^2}{\text{s}} - 2.30e - 10 \frac{\text{m}^2}{\text{s}} \right)$$

$$= 1.82e - 5 \text{ m}$$

10. Bacterial cell longitudinal dispersivity: α_{bx}

Since

$$\frac{\alpha_{by}}{\alpha_{bx}} = \frac{\alpha_{ay}}{\alpha_{ax}} = \frac{6.00e - 5 \text{ m}}{9.41e - 4 \text{ m}} = 6.38e - 2$$

So,

$$\alpha_{bx} = \frac{\alpha_{by}}{6.38e - 2} = \frac{1.82e - 5 \text{ m}}{6.38e - 2} = 2.85e - 4 \text{ m}$$

11. Bacterial cell longitudinal dispersion coefficient: D_{bx}

$$\begin{aligned} D_{bx} &= \alpha_{bx} \times V_f + \frac{D_{b,eff}}{\varepsilon} = 2.85e - 4 \text{ m} \times 1.55e - 5 \frac{\text{m}}{\text{s}} + 2.30e - 10 \frac{\text{m}^2}{\text{s}} \\ &= 4.66e - 9 \frac{\text{m}^2}{\text{s}} \end{aligned}$$

12. Oxygen longitudinal dispersion coefficient: D_{ox}

$$\frac{D_{o,eff}}{\varepsilon} = \frac{D_{o,bulk}}{\tau} = \frac{D_{o,bulk}}{\varepsilon^{-\frac{1}{3}}} = \frac{1.97e - 9 \frac{\text{m}^2}{\text{s}}}{0.37^{-\frac{1}{3}}} = 1.41e - 9 \frac{\text{m}^2}{\text{s}}$$

$$\begin{aligned} D_{ox} &= \alpha_{ox} \times V_f + \frac{D_{o,eff}}{\varepsilon} = \alpha_{ax} \times V_f + \frac{D_{o,eff}}{\varepsilon} \\ &= 9.41e - 4 \text{ m} \times 1.55e - 5 \frac{\text{m}}{\text{s}} + 1.41e - 9 \frac{\text{m}^2}{\text{s}} = 1.60e - 8 \frac{\text{m}^2}{\text{s}} \end{aligned}$$

13. Oxygen transverse dispersion coefficient: D_{oy}

$$\frac{D_{o,eff}}{\varepsilon} = \frac{D_{o,bulk}}{\tau} = \frac{D_{o,bulk}}{\varepsilon^{-\frac{1}{3}}} = \frac{1.97e - 9 \frac{\text{m}^2}{\text{s}}}{0.37^{-\frac{1}{3}}} = 1.41e - 9 \frac{\text{m}^2}{\text{s}}$$

$$\begin{aligned} D_{oy} &= \alpha_{oy} \times V_f + \frac{D_{o,eff}}{\varepsilon} = \alpha_{ay} \times V_f + \frac{D_{o,eff}}{\varepsilon} \\ &= 6.00e - 5 \text{ m} \times 1.55e - 5 \frac{\text{m}}{\text{s}} + 1.41e - 9 \frac{\text{m}^2}{\text{s}} = 2.35e - 9 \frac{\text{m}^2}{\text{s}} \end{aligned}$$

A9 COMSOL setting window capture

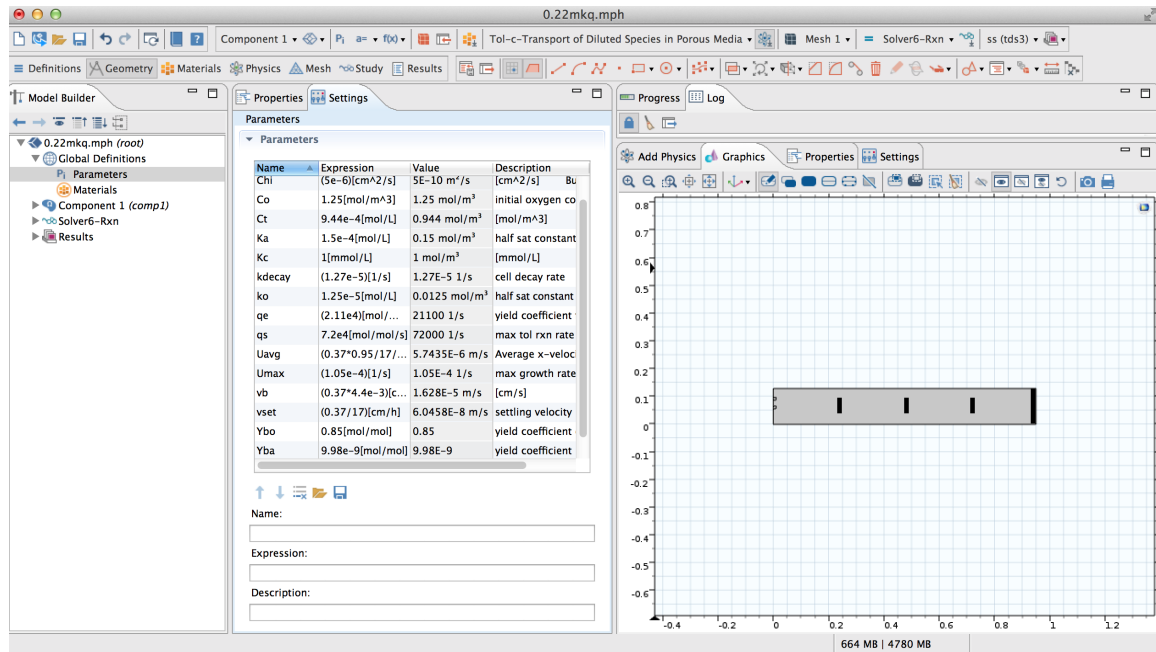


Figure A9.1 COMSOL parameter setting.

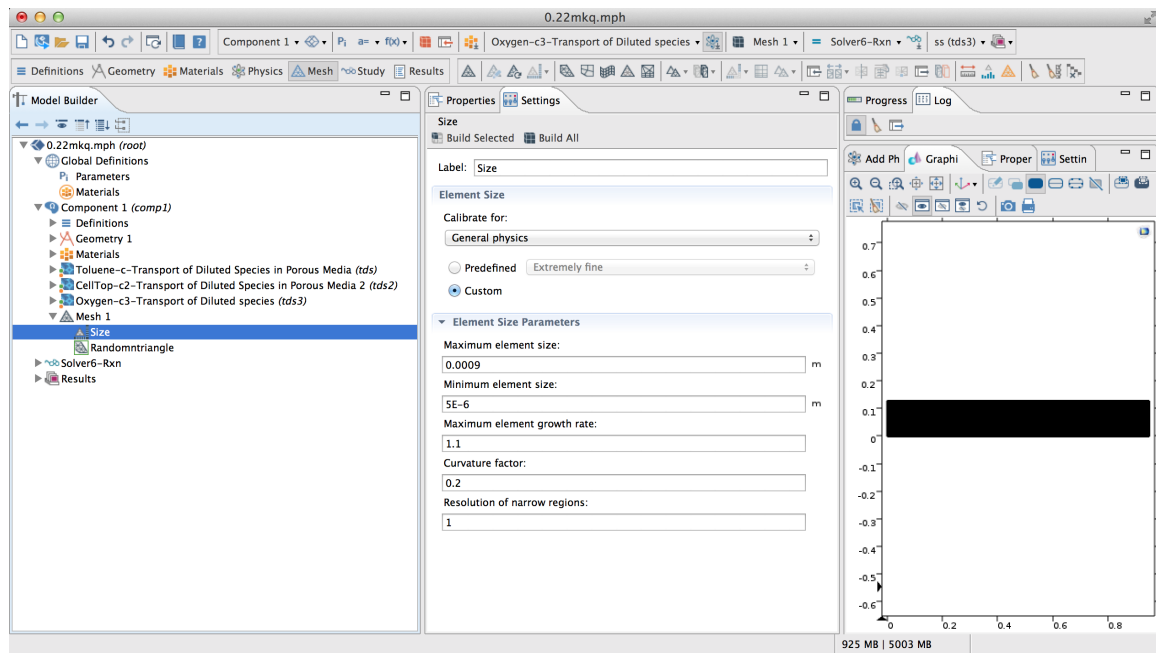


Figure A9.2 COMSOL Mesh setting.

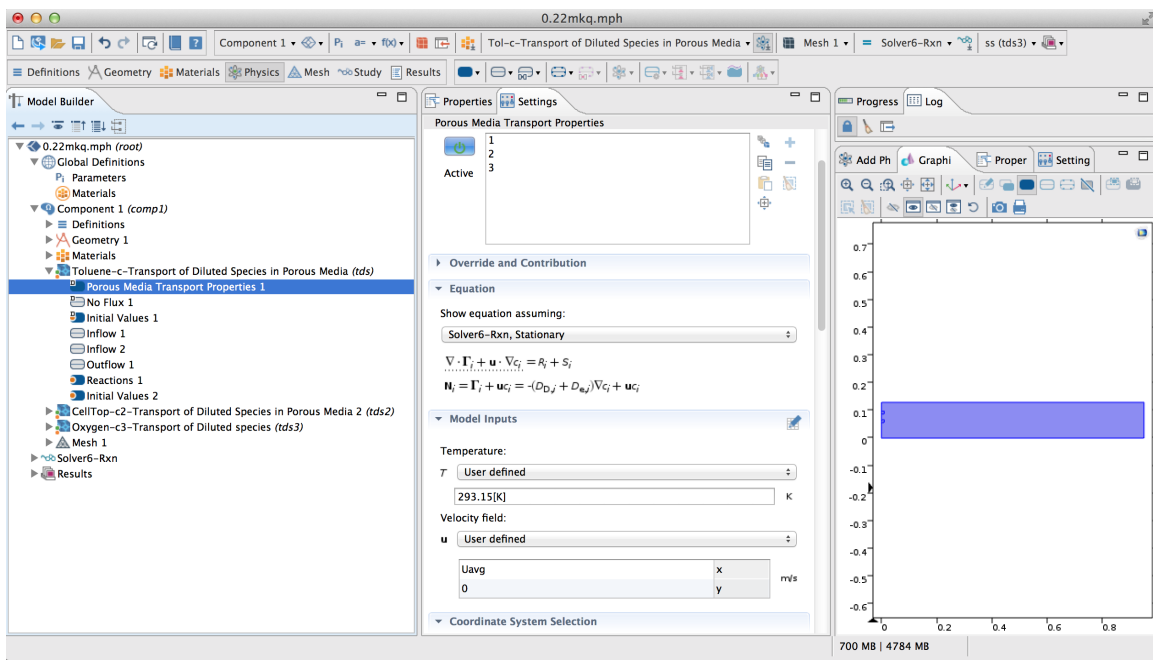


Figure A9.3 COMSOL setting for toluene (1).

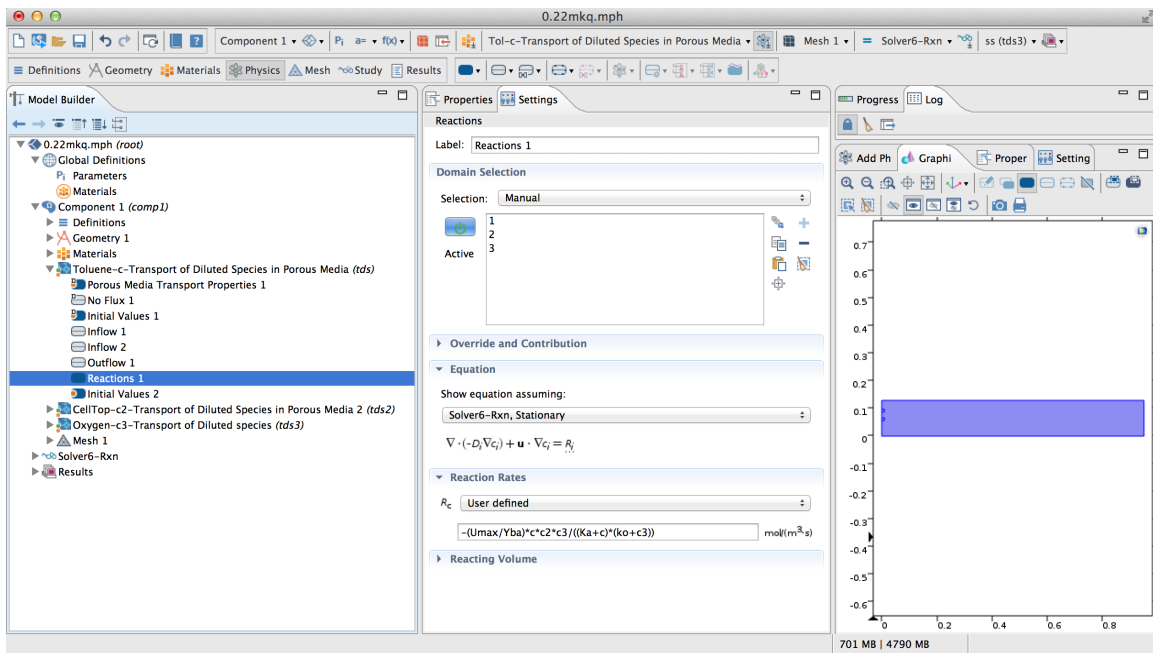


Figure A9.4 COMSOL setting for toluene (2).

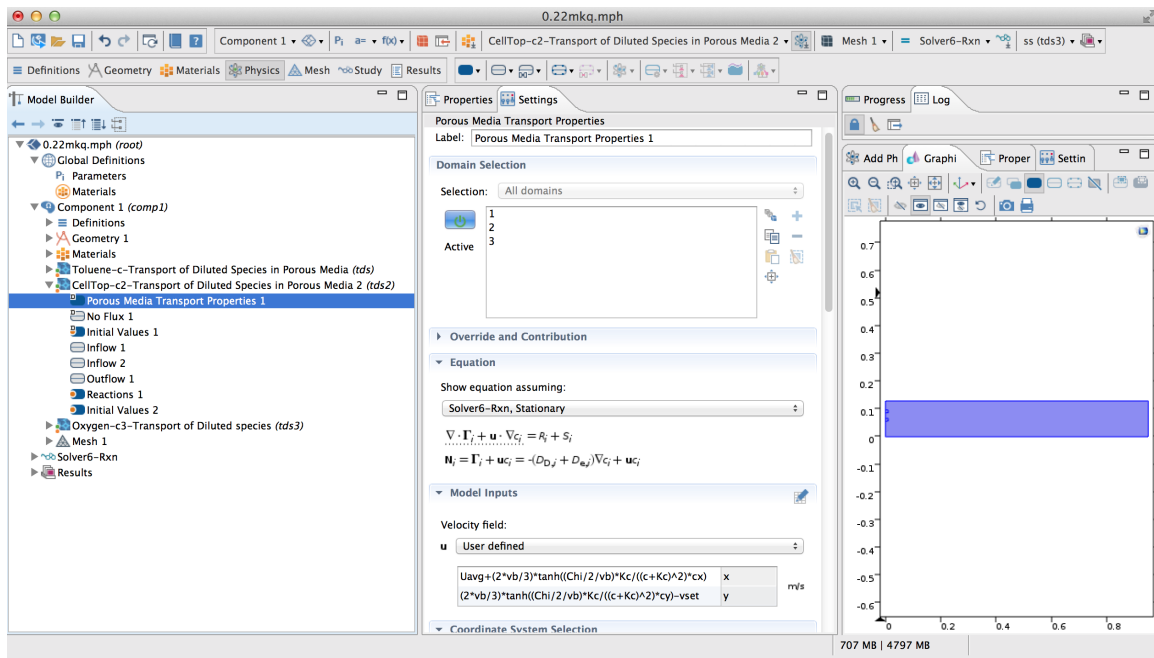


Figure A9.5 COMSOL setting for bacterial cell (1).

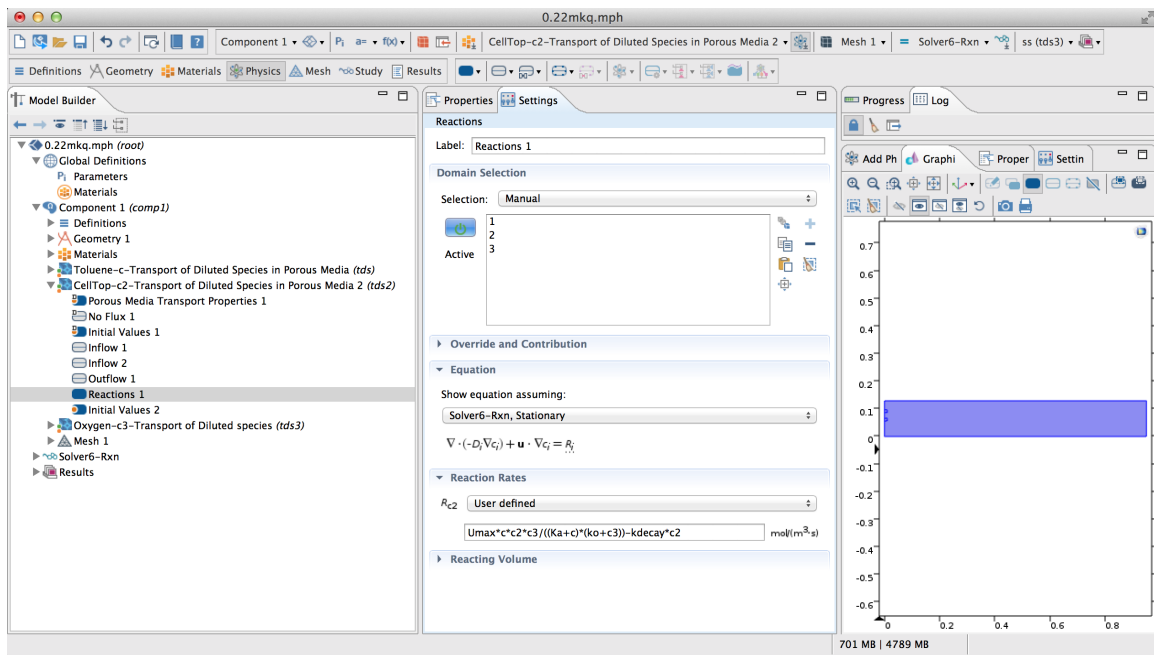


Figure A9.6 COMSOL setting for bacterial cell (2).

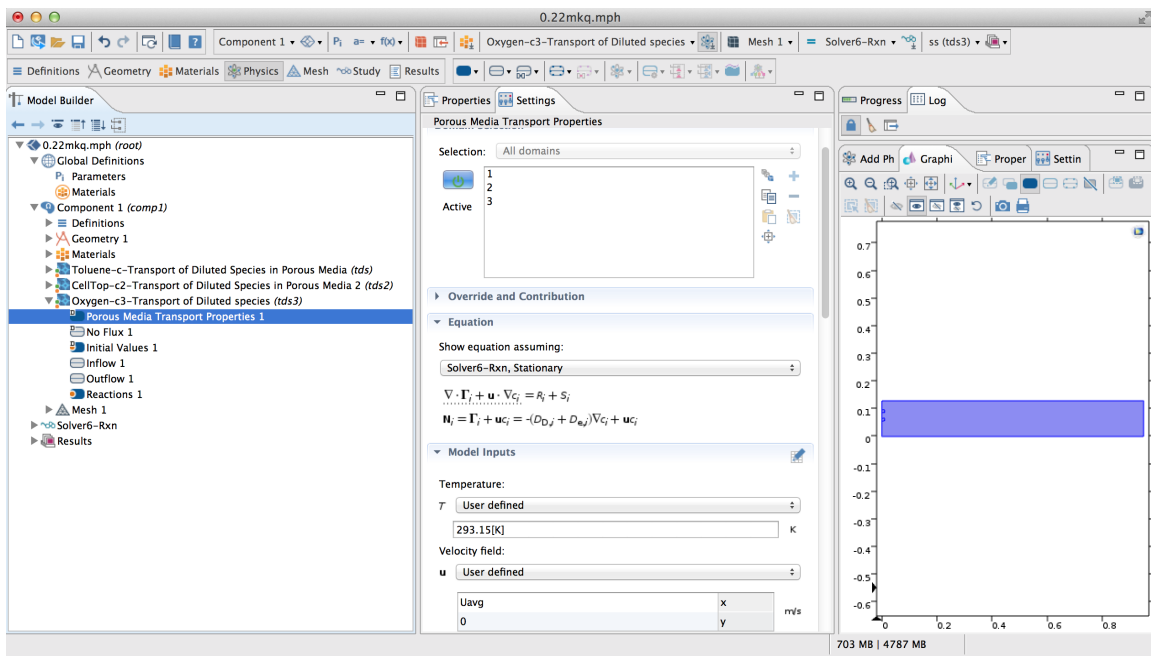


Figure A9.7 COMSOL setting for oxygen (1).

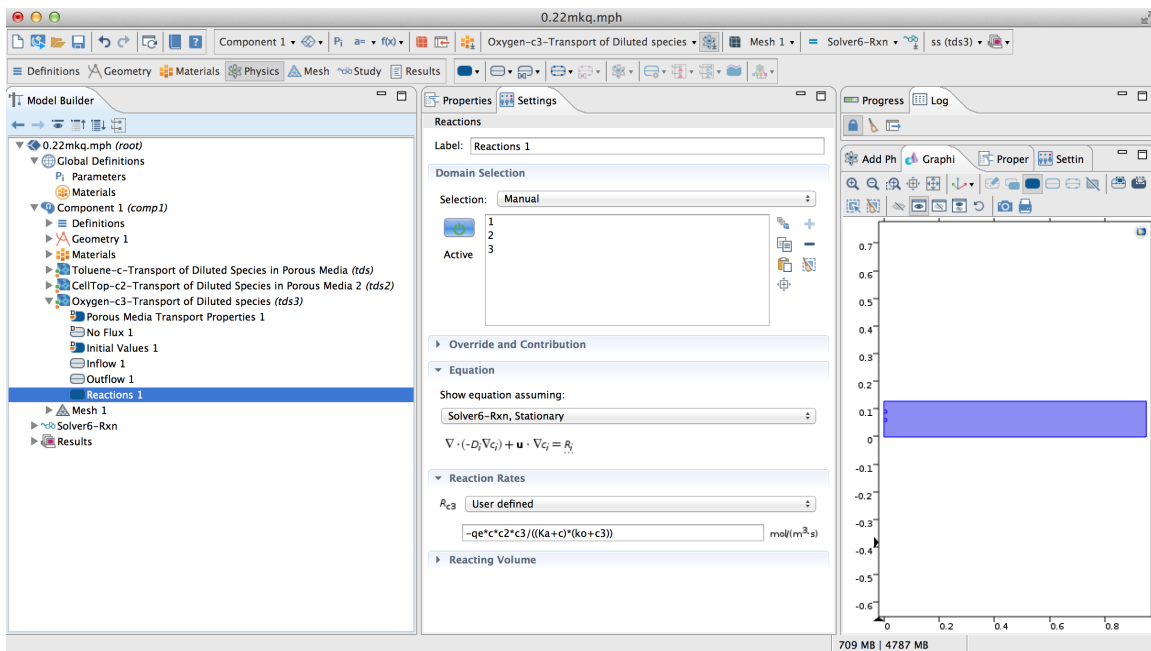


Figure A9.8 COMSOL setting for oxygen (2).

A10 Calculation of sensitivity of bacterial cell recovery to bacterial cell growth and chemotaxis parameters

Below: “*f*” denotes bacterial cell recovery, and “*x*” denotes Fold # of reference value of corresponding parameters

1) Experimental setup (3 cm spacing & Low flow rate)

μ_{max}

$$\text{Fitting line: } f = -2.0053 + 3.6865 * x + 3.4490 * x^2$$

$$\text{Slope} = \frac{df}{dx} = 3.6865 + 2 * 3.4490 * x$$

K_a

$$\text{Fitting line: } f = 13.0888 * \exp(-1.0005 * x)$$

$$\text{Slope} = \frac{df}{dx} = (-1.0005) * 13.0888 * \exp(-1.0005 * x)$$

$\chi_{0,eff}$

$$\text{Fitting line: } f = 5.0256 + 0.1056 * x - 0.0008 * x^2$$

$$\text{Slope} = \frac{df}{dx} = 0.1056 + 2 * (-0.0008) * x$$

K_c

$$\text{Fitting line: } f = 5.0497 + 0.2642 * \exp(-1.1827 * x)$$

$$\text{Slope} = \frac{df}{dx} = (-1.1827) * 0.2642 * \exp(-1.1827 * x)$$

2) With increased spacing (4 cm)

μ_{max}

$$\text{Fitting line: } f = 0.0176 + 1.4324 * x - 3.0143 * x^2 + 2.0889 * x^3$$

$$\text{Slope} = \frac{df}{dx} = 1.4324 + 2 * (-3.0143) * x + 3 * 2.0889 * x^2$$

K_a

$$\text{Fitting line: } f = 0.2130 + 10.4237 * \exp(-3.7488 * x)$$

$$\text{Slope} = \frac{df}{dx} = (-3.7488) * 10.4237 * \exp(-3.7488 * x)$$

$\chi_{0,eff}$

Fitting line: $f = 0.5602 + 0.0101 * x + 8.8854E-005 * x^2$

$$\text{Slope} = \frac{df}{dx} = 0.0101 + 2 * (8.8854E - 005) * x$$

K_c

Fitting line: $f = 0.5608 + (0.0096/x) - (0.0006/x^2)$

$$\text{Slope} = \frac{df}{dx} = -0.0096/x^2 - (-2) * 0.0006/x^3$$

3) High flow rate

μ_{max}

Fitting line: $f = 0.8325 + 0.0480 * x - 0.0003 * x^2 + 0.0005 * x^3$

$$\text{Slope} = \frac{df}{dx} = 0.0480 - 2 * 0.0003 * x + 3 * 0.0005 * x^2$$

K_a

Fitting line: $f = 0.8392 + (0.0385/x) - (0.0018/x^2)$

$$\text{Slope} = \frac{df}{dx} = -0.0385/x^2 - (-2) * 0.0018/x^3$$

$\chi_{0,eff}$

Fitting line: $f = 0.8797 + 0.0006 * x + 4.3732E-007 * x^2$

$$\text{Slope} = \frac{df}{dx} = 0.0006 + 2 * (4.3732E - 007) * x$$

K_c

Fitting line: $f = 0.8797 + (0.0006/x) - (2.9422E-005/x^2)$

$$\text{Slope} = \frac{df}{dx} = (-1) * 0.0006/x^2 - (-2) * (2.9422E - 005)/x^3$$